

STATISTICAL MODELING OF EARTH'S PLASMAPAUSE

by

Victoir Veibell
A Dissertation
Submitted to the
Graduate Faculty
of
George Mason University
In Partial Fulfillment of
the Requirements for the Degree
of
Doctor of Philosophy
Computational Space Sciences and Astrophysics

Committee:

_____ _____ _____	Robert Weigel, Dissertation Director Kirk Borne, Committee Member Fernando Camelli, Committee Member Jie Zhang, Committee Member Peggy Agouris, Interim Director, School of Physics, Astronomy, and Computational Sciences Peggy Agouris, Associate Dean, Office of Student Affairs & Special Programs, College of Science Peggy Agouris, Dean, College of Science Date: _____
	Spring Semester 2016 George Mason University Fairfax, VA

Statistical Modelling of Earth's plasmasphere

A dissertation submitted in partial fulfillment of the requirements for the degree of
Doctor of Philosophy at George Mason University

By

Victoir Veibell
Master of Science
George Mason University, 2014
Bachelor of Science
Embry Riddle Aeronautical University, 2010

Director: Robert Weigel, Professor
Department of Physics and Astronomy

Spring Semester 2016
George Mason University
Fairfax, VA

Copyright © 2016 by Victoir Veibell
All Rights Reserved

Dedication

I dedicate this dissertation to ... I dedicate this dissertation to ...

Acknowledgments

I would like to thank the following people who made this possible ... I would like to thank the following people who made this possible ...

Table of Contents

	Page
List of Tables	vii
List of Figures	viii
Abstract	0
1 Introduction	1
1.1 Background	1
1.1.1 Magnetosphere	1
1.1.2 Radiation Belts	7
1.1.3 Plasmasphere	9
1.1.4 Statistical Modeling of Magnetosphere and Plasmasphere	14
2 Models	20
2.1 Linear	20
2.1.1 Overview	20
2.1.2 ARX	20
2.1.3 ARMAX	23
2.1.4 Applicability	23
2.1.5 Caveats and Biases	23
2.1.6 Summary	26
2.2 Nonlinear	26
2.2.1 Overview	26
2.2.2 Neural Networks	27
2.2.3 Applicability	27
2.2.4 Caveats	27
2.2.5 Comparison to Linear Model	28
2.2.6 Summary	28
3 Measurements	31
3.1 Solar Wind	31
3.1.1 Source	34
3.1.2 Coverage	34
3.1.3 Data preparation	34

3.2	Geomagnetic	35
3.2.1	Source	35
3.2.2	Coverage	35
3.2.3	Data preparation	37
3.3	Plasmasphere and Plasmatrough	37
3.3.1	Source	37
3.3.2	Coverage	39
3.3.3	Data preparation	39
4	Analysis	41
4.1	Overview	41
4.2	Linear Correlations	41
4.3	Nonlinear Correlations	43
4.4	ARX	45
4.5	Epoch Analyses	46
4.6	$F_{10.7}$ Dependence	52
4.7	B_z Dependence	60
5	Onset Classification	66
5.1	Method	66
5.2	Results	67
5.2.1	Classification	67
5.2.2	Forecasting	72
A	An Appendix	75
	Bibliography	76

List of Tables

Table	Page
4.1 Table of linear model correlations showing the median of 100 random samples. Each sample trained on half of the data (via randomly selected rows of the least squares matrix) and tested on the other half.	42
4.2 Table of differences in linear training-testing models, where each correlation is the median correlation of 100 random samples. Each sample trained on half of the data (via randomly selected rows of the least squares matrix) and tested on the other half.	43
4.3 Table of nonlinear model test correlations showing the median of 100 random samples. Each sample trained on half of the data (via randomly selected rows of the least squares matrix) and tested on the other half.	44
4.4 Table of differences in nonlinear training-testing models, where each correlation is the median correlation of 100 random samples. Each sample trained on half of the data (via randomly selected rows of the least squares matrix) and tested on the other half.	44
4.5 Table of ARX model correlations created from the mean of 100 bootstrap models. CC-1 models have one hour of time lag, and CC-24 have 24 hours of time lags.	45

List of Figures

Figure	Page
1.1 Overview of the magnetosphere and plasmasphere [Russel, 2007]	2
1.2 Overview of inner magnetosphere. Adapted from [NASA]	3
1.3 Currents in/around the magnetosphere. Adapted from [Maus, 2010]	4
1.4 Top-down schematic of particle drift [Gold, 1959]	5
1.5 Data from GOES 6 around March 1989 geomagnetic storm	6
1.6 Motion of magnetically trapped particles [Walt, 1994]	8
1.7 Relative position of plasmasphere (blue) and radiation belts (red) with varying geomagnetic activity levels [Carreau, 2013].	9
1.8 Plasmasphere ion density emptying and refilling as measured by GEO in 2007, along with coinciding solar wind conditions. From [Denton and Borovsky, 2014].	11
1.9 Plasmapause position varying with K_p as represented by several particular plasmapause crossings made on outbound passes between local times of midnight and 0400. From [Lemaire, 1998]	12
1.10 Multiple ISEE 1 passes made between 09-15 MLT during saturated plasmapause conditions. From [Lemaire, 1998]	13
1.11 Plasmasphere dusk-side bulge with geomagnetic activity. The solid line is the average position of the plasmasphere knee during periods of $K_p = 2 - 4$, while the dots indicate a specific instance of increasing magnetic activity, and the dashes a specific instance of decreasing activity. From [Lemaire, 1998]. .	14
1.12 Map of ground stations used to measure the K_p , AE , and D_{st} indices. From [Allen, 1982].	16
2.1 (a) D_{st} (black), persistence (red), 12-hour impulse response model (blue). (b) vB_S input.	21
2.2 Correlation between prediction and measurement vs lead time of forecast .	24

2.3	Effect of using means over medians. Top: Events averaged using median values. Bottom: Events averaged using mean values.	29
2.4	Nonlinear models (left) vs linear models (right) of ρ_{eq}	30
3.1	Data from GOES 6 with dashed lines indicating default event thresholds discussed in Chapter 4.	32
3.2	Four examples of specific events from GOES 6.	33
3.3	Top: Model of magnetopause location showing location of GOES satellites in geosynchronous orbit. From [CCMC], taken during a period of $K_p=4$. Bottom: Model of plasmapause location as it varies with geomagnetic activity where the symbols indicate the local time of maximum plasmapause location. From [O'Brien and Moldwin, 2003]	36
3.4	Top: Detection rate of f_{T3-30m} for magnetic latitudes of 5, 9, and 11 degrees (curves A, B, and C respectively). From [Takahashi et al., 2010]. Bottom: MLT of all available data	38
3.5	Location of detected plasmapause on CRRES against the maximum K_p value for the previous 12 hours. From [Moldwin et al., 2002]	39
4.1	Median ρ_{eq} binned by magnetic local time	42
4.2	Epoch analysis for D_{st} events on an hourly timescale.	47
4.3	Epoch analysis for D_{st} events on an daily timescale.	48
4.4	Epoch analysis for D_{st} events on an daily timescale using only the years of 1989-1991 from [Takahashi et al., 2010].	50
4.5	Epoch analysis for D_{st} events on an daily timescale using only the years of 1989-1991.	51
4.6	Bootstrap differences between median daily value of events using only the years of 1989-1991.	52
4.7	Epoch analysis for D_{st} events lasting longer than 12 hours.	53
4.8	Epoch analysis for ρ_{eq} events on an daily timescale.	54
4.9	Epoch analysis for randomly selected events on an hourly timescale.	55
4.10	Epoch analysis for randomly selected events on a daily timescale.	56
4.11	Top: Comparing $F_{10.7-27d}$ and $\log(\rho_{eq-27d})$ using GOES 6 data. Bottom: Same as top, but all available satellites.	57
4.12	$F_{10.7}$ and $\log(\rho_{eq})$ correlation at varying time scales.	58
4.13	ρ_{eq} (top panel) and D_{st} (bottom panel) of D_{st} events binned by median $F_{10.7}$ values.	59

4.14	ρ_{eq} events binned by median $F_{10.7}$ before (top panel) and after (bottom panel) event onset.	61
4.15	D_{st} events binned by median $F_{10.7}$ before (top panel) and after (bottom panel) event onset.	62
4.16	ρ_{eq} events binned by median B_z before (top panel) and after (bottom panel) event onset.	63
4.17	Top: D_{st} predicted by nonlinear model of day of year. Bottom: Same, but including a dimension for B_z .	65
5.1	Diagram of classification (top) and prediction (bottom) methods.	67
5.2	Prediction confusion matrix for hourly (left) and daily (right) ρ_{eq} onset events using classification method	68
5.3	Histogram of onset conditions for daily-averaged ρ_{eq} events binned by correctness of prediction	69
5.4	Prediction confusion matrix for hourly (left) and daily (right) ρ_{eq} onset events, including ρ_{eq} as an input variable, and only looking at three hours before and including onset	70
5.5	Histogram of onset conditions for hourly ρ_{eq} events including ρ_{eq} as an input, binned by correctness of prediction	71
5.6	Prediction confusion matrix for hourly (left column) and daily (right column) ρ_{eq} onset events, including ρ_{eq} as an input in the bottom row, and using entire timeseries with a four hour sliding window	72
5.7	Histogram of onset conditions for daily ρ_{eq} events including ρ_{eq} as an input, binned by correctness of prediction	74

Abstract

STATISTICAL MODELLING OF EARTH'S PLASMASPHERE

Victoir Veibell, PhD

George Mason University, 2016

Dissertation Director: Robert Weigel

This dissertation intends to first: be a survey of current forecasting capabilities of statistical and magnetohydrodynamic (MHD) methods of Earth's magnetosphere, and second: attempt to improve upon forecasting methods by investigating the usefulness of various new models on both real and modeled data. The forecasting focuses on significant geomagnetic events and the predictability thereof using solar wind and magnetospheric drivers. This dissertation also attempts to discern significant nonlinear behaviors in the plasmatrough to aid in its modeling.

Chapter 1: Introduction

1.1 Background

This dissertation investigates the behavior of the plasmasphere and tests the ability to forecast space weather events based on said behavior. This chapter introduces the major connections the plasmasphere has with the magnetosphere and radiation belts, as well as how their individual processes are interdependent. It then explores previous attempts to statistically model the magnetosphere and plasmasphere.

1.1.1 Magnetosphere

Discovery

The dynamic processes of Earth's magnetosphere and their various impacts on the planet and its inhabitants have been studied for centuries: from Celsius and Hiorter who noted a correlation between compass orientation and aurora [Soon and Yaskell, 2003] to the Carrington event in 1859 that established the connection between solar output and electromagnetic effects on Earth [Carrington, 1859].

It was not until Van Allen performed his rocket sounding and satellite measurements of high altitude cosmic rays, finding the eponymous Van Allen Radiation Belt, that the structure of the magnetosphere was generally accepted to be more complex than that of a basic dipole magnet [Newell, 2011]. Gold [1959] showed that charged particles captured from the solar wind plasma are broken into constituent parts that drift in opposing directions around the Earth, leading to a deeper understanding of the behavior the magnetosphere and its interconnectivity with structures both inwards and outwards.

The overall magnetospheric system is portrayed in Figure 1.3, showing where the solar wind interacts with the bow shock, the magnetopause, and finally the plasmasphere, as well

as the overall structure this creates. Each of these components is described in a subsection of this chapter.

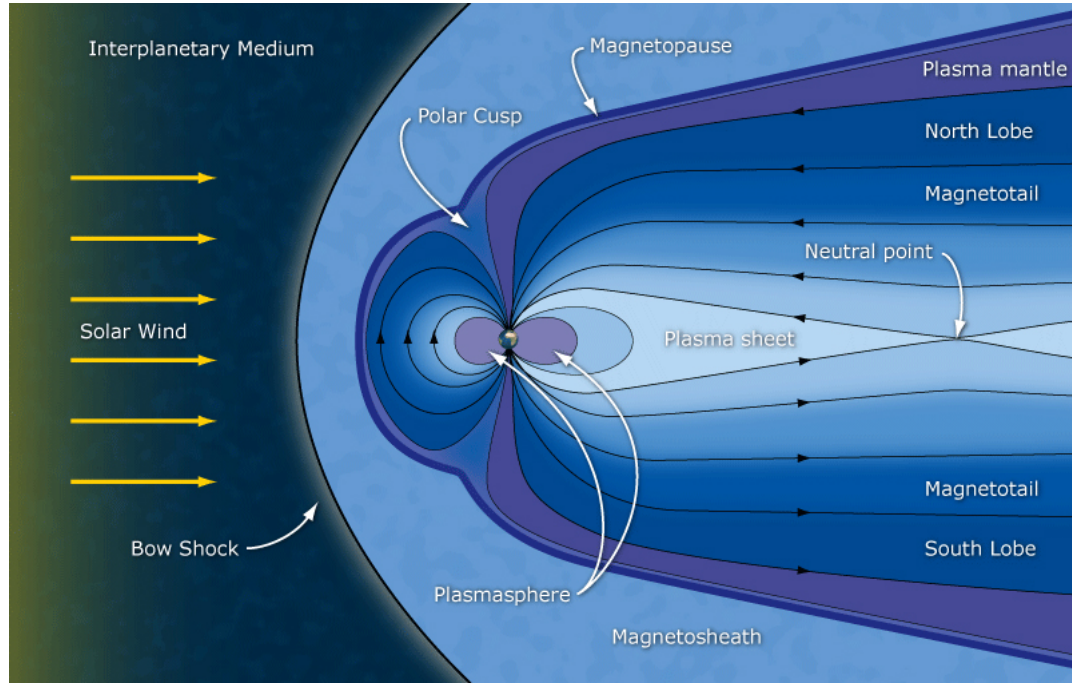


Figure 1.1: Overview of the magnetosphere and plasmasphere [Russel, 2007]

The inner magnetosphere, where this dissertation is primarily focused, is composed of three main constituent parts: the plasmasphere, the ring current, and the radiation belts, all of which are shown in Figure 1.2. This helps illustrate how the parts are not always spatially distinct and, depending on conditions, often overlap.

Processes

The complex structure of the magnetosphere and plasmasphere leads to a number of distinct behaviors and processes such as a ring current and geomagnetic storms and substorms, all of which are driven by the solar wind.

The Ring Current, one of the major magnetospheric currents shown in Figure 1.3, is composed of charged particles drifting opposite directions around the Earth based on their

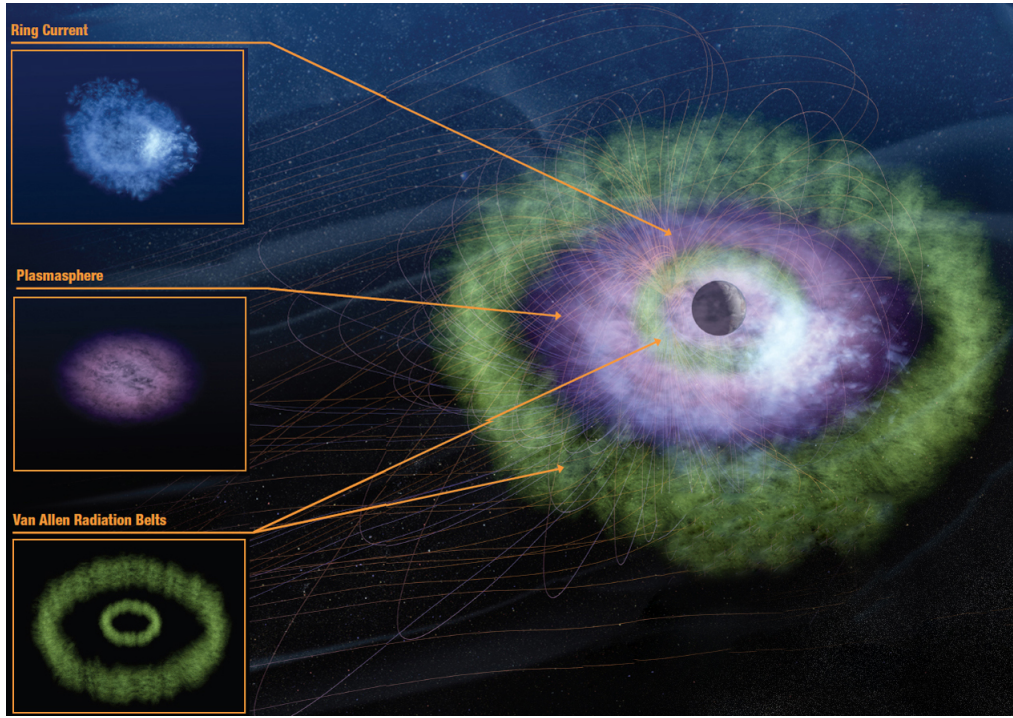


Figure 1.2: Overview of inner magnetosphere. Adapted from [NASA]

polarity. A schematic of this from a top-down perspective is shown in Figure 1.4. With enough energetic particles drifting together, a current is generated that can significantly affect the magnetic field measured on Earth’s surface. These particles in the current are energized into the magnetosphere via conditions that cause the solar wind’s magnetic field to reconnect with that of Earth.

Geomagnetic storms occur when the solar wind interacts with the Earth’s magnetosphere in such a way as to produce significant disruptions in its normal, quiet-time, behavior. A geomagnetic storm is generally defined by a significant change to the magnetic field measured by multiple ground-based magnetometer measurements from stations spread around the world, in the case of the K_p index, or around the geomagnetic equator in the case of the disturbance storm-time (D_{st}) index. These indices are used to classify storms into categories of severity [Oceanic and Administration, 2005]. The definition of storms in the literature varies slightly between authors [Yermolaev and Yermolaev, 2006], but most agree

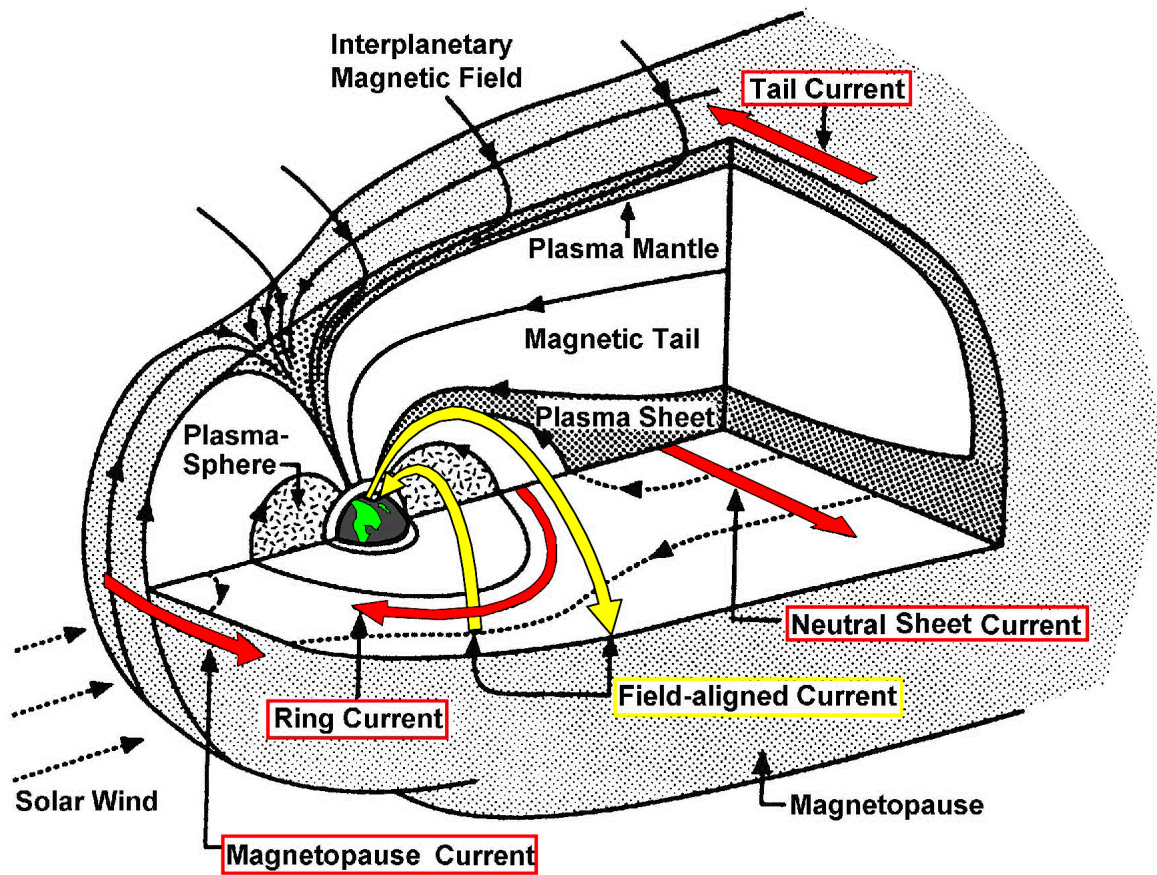


Figure 1.3: Currents in/around the magnetosphere. Adapted from [Maus, 2010]

that sustained and abnormally perturbed near-earth and mid-to-low geomagnetic latitude magnetic field strengths over several hours or more constitutes a geomagnetic storm [Gosling et al., 1991].

Geomagnetic substorms, in contrast with storms, are much shorter; typically only lasting for an hour or two, and potentially happening soon after one another. They tend to have a less appreciable effect on the amount of particles/energy in the ring current, and are associated with sudden changes in energy coming from the tail of the magnetosphere rather than the dayside reconnections associated with storms [Gonzalez et al., 1994]. Figure 1.5 serves as an example of this, where a long, high-intensity storm is punctuated with a few

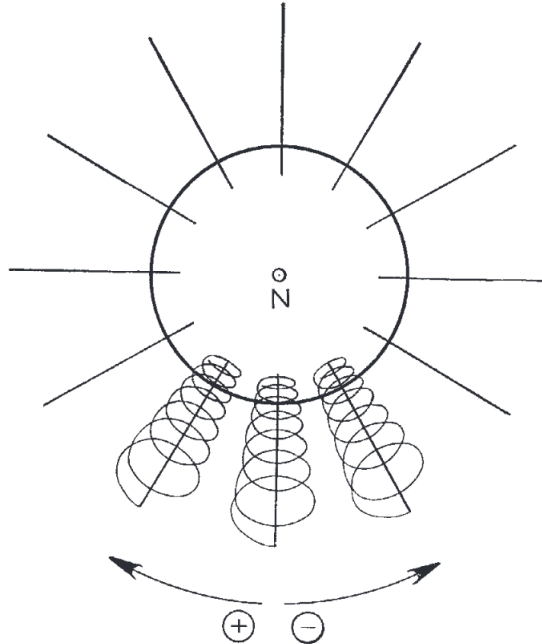


Fig. 2. Captive particle orbits, schematically, as seen from above the North Pole. Electrons will drift slowly eastwards, positive ions westwards

Figure 1.4: Top-down schematic of particle drift [Gold, 1959]

small, short disturbances in both B_z and D_{st} .

Geomagnetic storms and substorms can have significant impacts on Earth and space systems, from inducing currents in large power grids to harming satellite circuitry and on-board data [Allen et al., 1989]. Because of the potential damage of such events, any ability to forecast a storm could allow operators to prevent or mitigate problems in their systems. Because of the large correlation of CMEs with geomagnetic storms [Yermolaev and Yermolaev, 2006], it can be estimated that our forewarning time is the difference between observing a CME (via visual or X-ray methods) and its propagation time plus magnetospheric interaction time. This time can span from one to five days, depending on the speed of the CME and how it interacts with the interplanetary medium [Zhang et al., 2007].

All of these processes are coupled to some degree with the plasmasphere, by transferring plasma and energy from the interplanetary medium to near-Earth regions ($\lesssim 8R_E$).

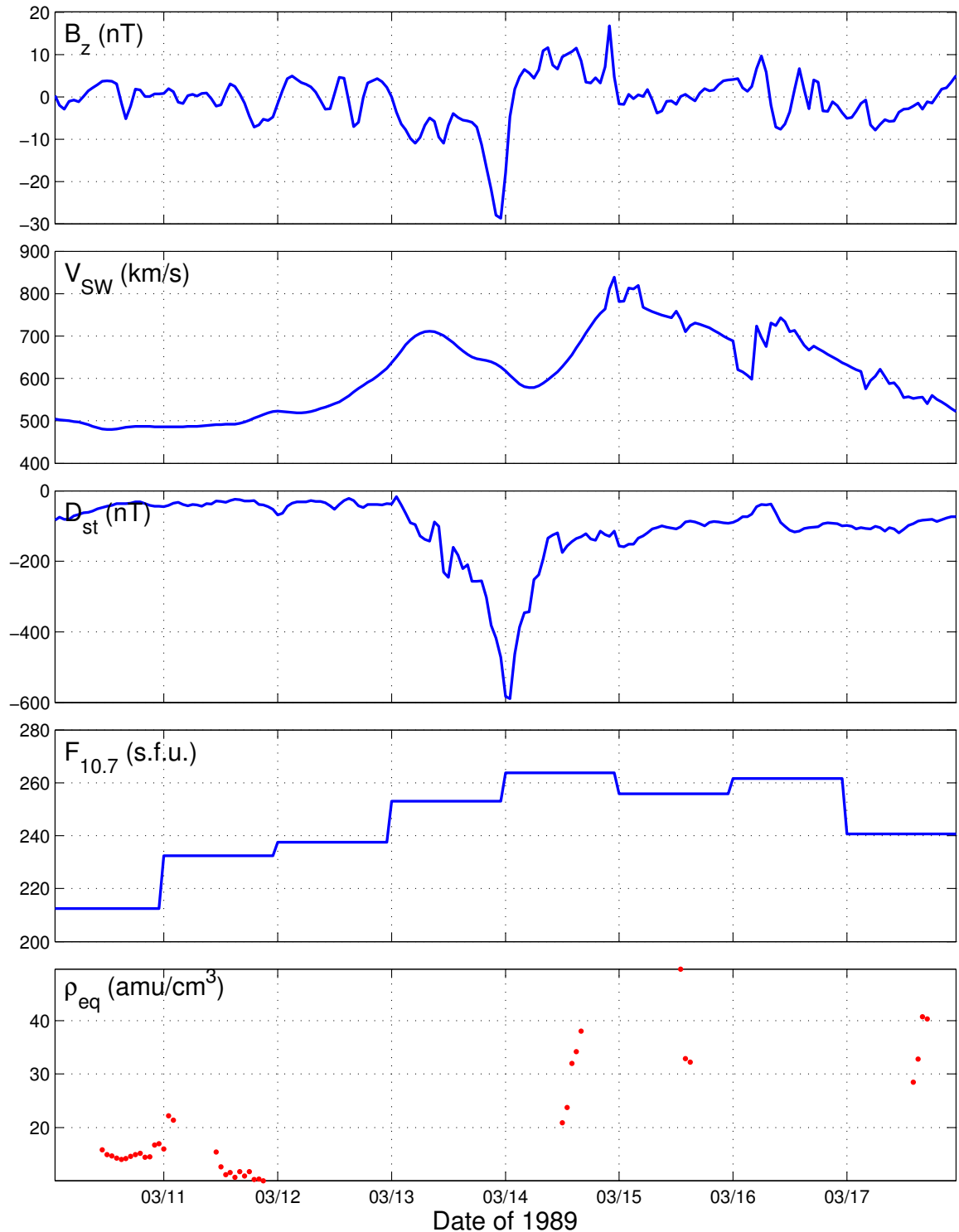


Figure 1.5: Data from GOES 6 around March 1989 geomagnetic storm

1.1.2 Radiation Belts

Discovery

The radiation belts that surround Earth, known as the Van Allen Radiation Belts, are two (occasionally three [Darrouzet et al., 2013]) bands of energetic particles encircling the planet. The existence of such bands was theorized based on knowledge of magnetically trapped motion of charged particles; results from rocket soundings showed that more radiation exists in the auroral regions than at the equator. The beginning of the space age allowed particle counters to be launched onboard the Explorer 1 and Explorer 3 satellites, which found radiation far beyond what was anticipated and concentrated into bands of high intensity [Newell, 2011].

Processes

The outer radiation belt is filled with electrons captured from the solar wind by the magnetosphere and then injected into the radiation belts from the magnetotail, and occasionally lost when the magnetopause moves back Earthward [Millan and Thorne, 2007]. The inner belt tends to be filled by heavier species from the ionosphere, and is overall less variable than the outer belt [Darrouzet et al., 2013]. It gains particles from inward radial diffusion and loses them to the atmosphere via plasmaspheric hiss [Lyons and Thorne, 1973]. The slot region between the two is formed by the interaction of energetic particles with very low frequency (VLF) waves, leading to particle loss to the atmosphere [Fung et al., 2006]. In contrast to the ring current particles, the radiation belt particles tend to have much higher energy

The various forms of particle movement are shown in Figure 1.6. The primary component being the drift motion leading to the ring current. As particles approach the “Mirror point”, a slight angle between the guiding center motion and the magnetic field line leads to a force opposing the motion along the line, eventually mirroring the particle back in the

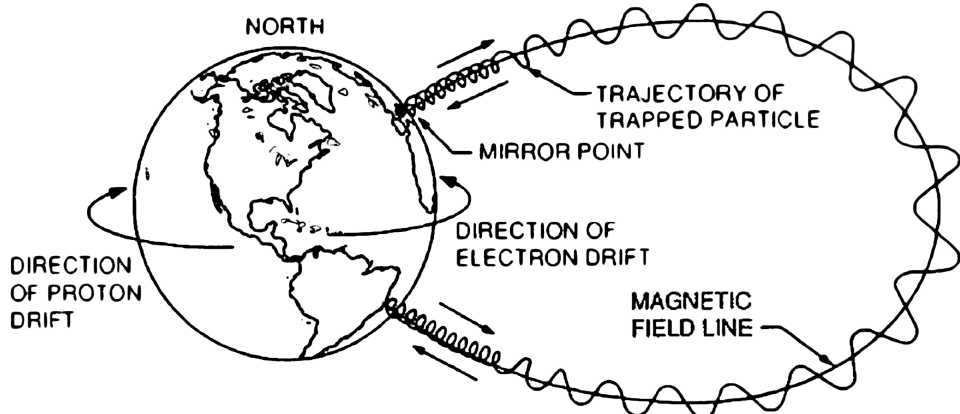


Figure 1.6: Motion of magnetically trapped particles [Walt, 1994]

opposite direction. Because mirroring applies to all particles within a certain range of energies and pitch angles, the collective sum of trapped particles forms the radiation belts. By modeling the particle mass, momentum, and the magnetic field strength of a given dipole magnetic field, approximations can be made regarding the amount of particles that will become trapped in the field, and the amount that will be lost to scattering [Young et al., 2008].

The radiation belts have an impact on the plasmasphere by acting as an occasional source of low energy particles and a sink for high energy particles. The plasmasphere also acts on the radiation belts via the VLF waves, energizing electrons out of the plasmasphere and into the radiation belts, or providing particles already in the belts the energy needed to become untrapped [Darrouzet et al., 2013]. While the outer limits of the plasmasphere and the outer radiation belt often coincide and react similarly to geomagnetic activity, they can become separated during geomagnetically active times [Darrouzet et al., 2013]. An example of this variation in relative position is shown in Figure 1.7.

Another source/sink of energy for particles in the radiation belts (or general magnetospheric plasma) is via Alfvén waves [Keiling, 2009]. These waves are composed of oscillating

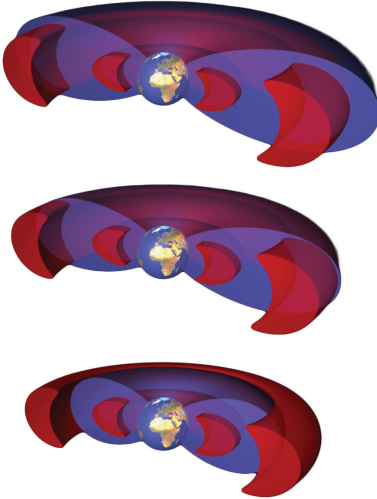


Figure 1.7: Relative position of plasmasphere (blue) and radiation belts (red) with varying geomagnetic activity levels [Carreau, 2013].

electromagnetic fields carrying both energy and field-aligned currents (via oscillating electrons) as they propagate. By moving energy along the field lines, Alfvén waves also couple the various distinct regions of plasma around Earth.

1.1.3 Plasmasphere

Discovery

The plasmasphere, shown in Figure 1.2, was largely unknown until the beginning of the space age, being found both through analyses of very low frequency radio waves and in-situ spacecraft measurements. Previously, it was believed that electron density decreased continuously from the ionosphere to the interplanetary medium [Lemaire, 1998]. These experiments showed that the Earth had a sphere of cold plasma around it that ended in an abrupt boundary, and varied in location and density gradient with geomagnetic activity [Carpenter, 1966, Lemaire, 1998].

Processes

The plasmasphere is interconnected with the radiation belts and the ionosphere. While many of the specifics of this interaction are still not fully understood, some parts have been observed and explained to a reliable degree of accuracy.

In the ionosphere, during the daytime sunlight photoionizes oxygen which produces excess electrons that are transferred up via polar wind into the plasmasphere along magnetic field lines bringing energy and heat along with it. This daily “refilling” flux continues until a saturation point is reached, bringing the lower bounds of the plasmasphere into equilibrium with the upper ionosphere. This flux also typically reverses on the night side, sending electrons back down into the ionosphere [Lemaire, 1998]. Figure 1.8 shows one particular example of active geomagnetic conditions emptying the plasmasphere following by a quiet time refilling flux restoring density over a couple of days.

During periods when the location of the plasmapause is quickly brought earthwards, or the plasmapause is re-established in a new location, plasma left outside the plasmapause is known to be magnetically convected outwards and sunwards [Carpenter and Lemaire, 1997, Lemaire, 1998], termed “eroding” the plasmasphere. This is because the location of the plasmapause can vary greatly with geomagnetic conditions. Figure 1.9 shows how the L -shell distance varies with magnetic activity via the K_p index.

Figure 1.9 also shows the plasmatrough; the low density region just outside the plasmapause where particle count often drops multiple orders of magnitude from the plasmasphere and continues out through the magnetosphere. The location of what is called the ”plasmapause knee” varies with time and geomagnetic activity, where the dayside boundary is often less steep than the nightside boundary. It’s also observed in Figure 1.10 that after multiple days of quiet geomagnetic conditions, the saturated plasmasphere smooths the knee out until the plasmapause is almost unidentifiable [Lemaire, 1998].

At times, the plasmasphere becomes distorted at the plasmapause due to dayside reconnection, causing bulges that can become elongated and detached during co-rotation, usually on the dusk side. These extended segments of plasma are known as “plumes” and appear

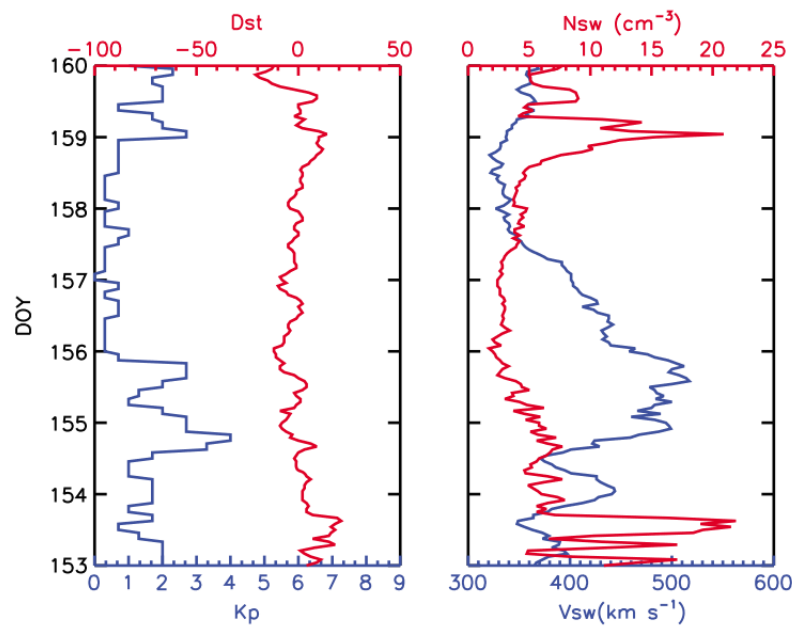
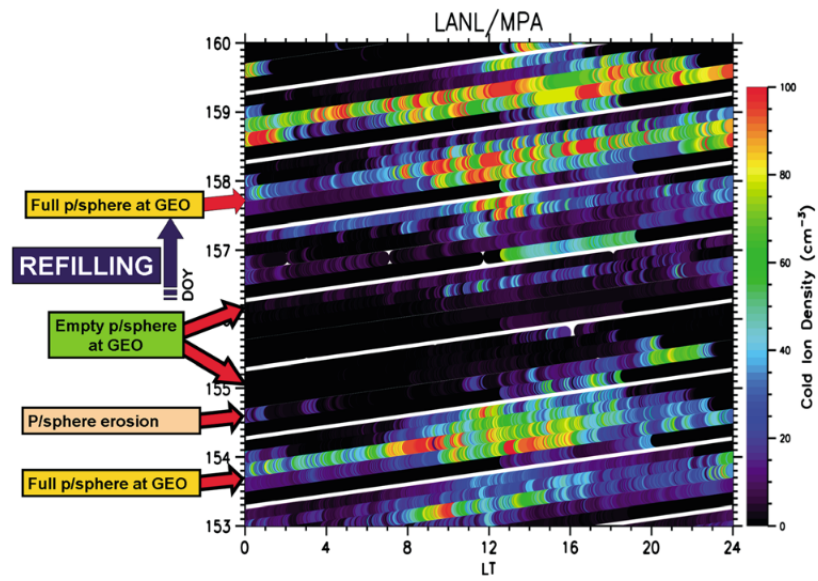


Figure 1.8: Plasmasphere ion density emptying and refilling as measured by GEO in 2007, along with coinciding solar wind conditions. From [Denton and Borovsky, 2014].

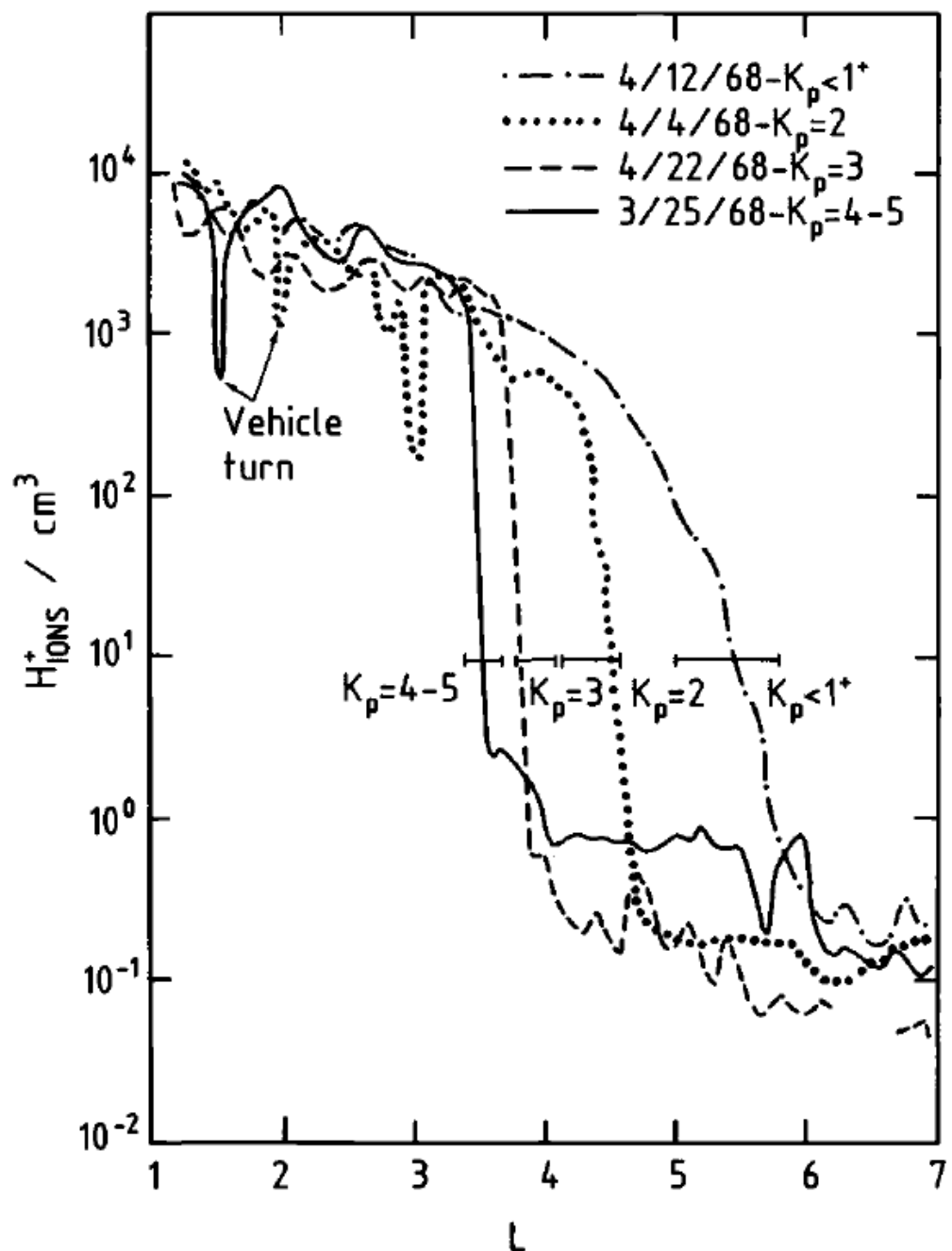


Figure 1.9: Plasmapause position varying with K_p as represented by several particular plasmapause crossings made on outbound passes between local times of midnight and 0400. From [Lemaire, 1998]

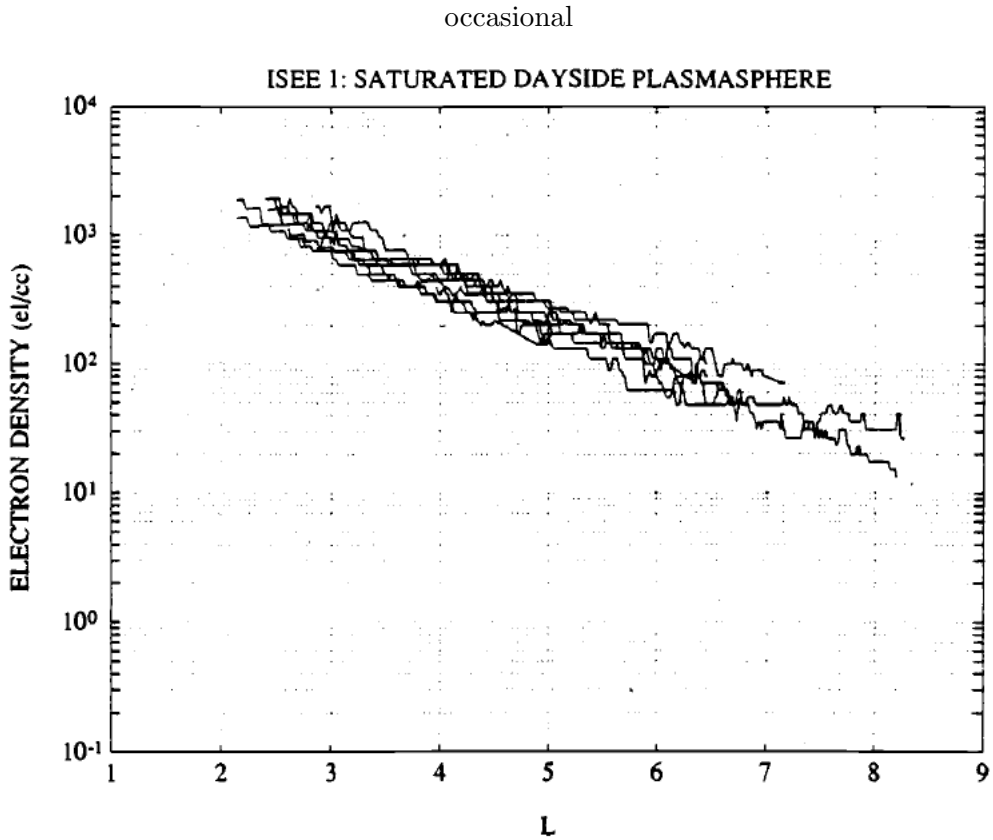


Figure 1.10: Multiple ISEE 1 passes made between 09-15 MLT during saturated plasma-pause conditions. From [Lemaire, 1998]

as a peak in density in a normally empty plasmatrough. These plumes also often occur with, and possibly because of, enhanced magnetospheric activity [Elphic et al., 1996]. This bulge, and the effects of geomagnetic activity on the bulge, is shown in Figure 1.11

What's not particularly well studied or understood is the behavior of plasma mass density in the plasmatrough. Most studies focus on behavior inside the plasmapause where density is higher and easier to measure, but since this mass diffuses inwards from the solar wind and through the plasmatrough, and satellites are often located in the plasmatrough (geostationary equatorial orbit (GEO) is at about $6-7 R_E$), it is worthwhile understanding the behavior of the region. This work takes a dataset specifically focused on mass density in the plasmatrough and attempts to understand, classify, and forecast behavior as it relates to solar wind and geophysical conditions.

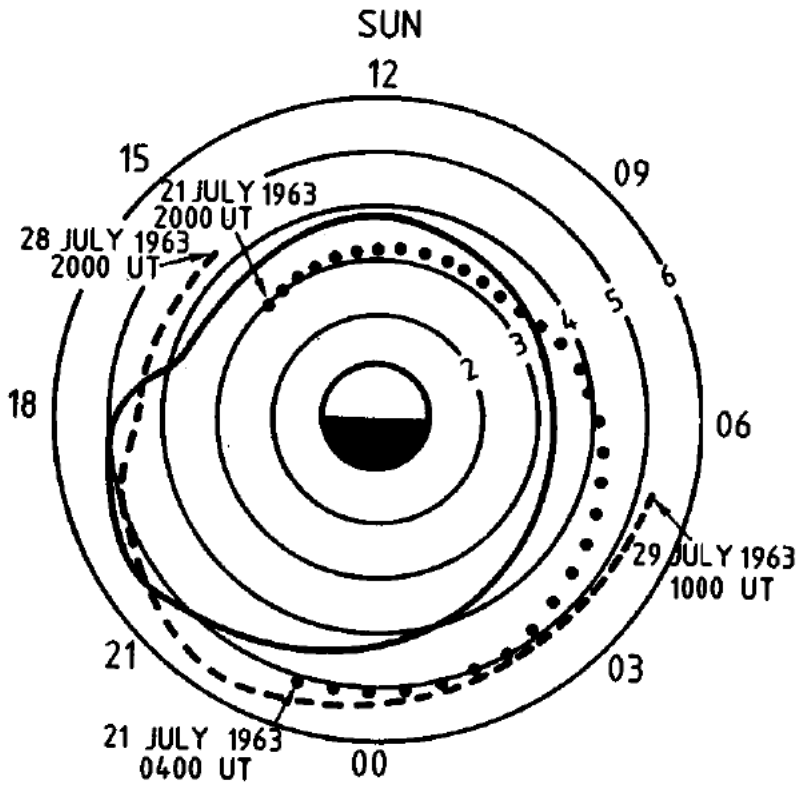


Figure 1.11: Plasmasphere dusk-side bulge with geomagnetic activity. The solid line is the average position of the plasmasphere knee during periods of $K_p = 2 - 4$, while the dots indicate a specific instance of increasing magnetic activity, and the dashes a specific instance of decreasing activity. From [Lemaire, 1998].

1.1.4 Statistical Modeling of Magnetosphere and Plasmasphere

Initial forecasts of geomagnetic disturbances were based on an observed time delay from sunspot sitings [Richardson, 1936]. The state of geomagnetic storm forecasting then advanced to a basic theory involving electromagnetic interactions in the magnetosphere [Chapman and Ferraro, 1931]. There now exist entire services dedicated to executing statistical and magnetohydrodynamic (MHD) based models of the magnetosphere [CCMC], as well as

multi-year, multi-institution efforts to survey the general statistics of modeling and forecasting of extreme events [Ghil et al., 2011].

The convergence of the advancement in both statistical and MHD-based simulation has led to a situation where the scientific community has the capacity for monitoring and forecasting the near-Earth effects in real time. There have been efforts to test the forecast performance of select models over a small number of geomagnetic events [Bala and Reiff, 2012, Tsyganenko and Sitnov, 2005, Zhang et al., 2006, Yermolaev and Yermolaev, 2006, Birn et al., 2001]. However no research has been done that involves the analysis of long-term forecasting performance of these models and comparison of the results with existing methods.

Three main metrics of magnetospheric activity are seen throughout the literature; the K_p index: a measure of magnetosphere convection caused by currents induced by a changing plasma sheet (and indirectly from the global convection field strength) [Thomsen, 2004]; the AE index: a measure of electrojet activity based on the maximum and minimum field strength measurements from magnetometer stations at auroral latitudes [Davis and Sugiura, 1966]; and the previously mentioned D_{st} index based on magnetic field perturbations caused primarily by a changing ring current. All three indices are derived from a set of ground stations shown in Figure 1.12 based on the nature of the metric.

Models specific to the plasmasphere and plasmatrough include Carpenter and Anderson's ISEE/Whistler Model of Equatorial Electron Density in the Magnetosphere, which use empirical data to determine the location and density of the saturated plasmasphere and plasmatrough [Carpenter and Anderson, 1992]. Carpenter and Anderson [1992] analyze ISEE 1 data for drops in number density of at least a factor of 5 across half an L-shell and state that the inner edge of the plasmapause is located at $L_{ppi} = 5.6 - 0.46K_{p_{max}}$. Here $K_{p_{max}}$ is the maximum value of K_p (an index averaging 11 mid-latitude stations in the previous 24 hours), and L is the set of magnetic field lines at a distance of L Earth radii at the magnetic equator. This specifies the outer boundary of the plasmasphere, and from there the density is modeled inwards as $n_e = n_{e_{L_{ppi}}} \cdot 10^{-(L-L_{ppi})/\Delta pp}$, where $n_{e_{L_{ppi}}}$ relates

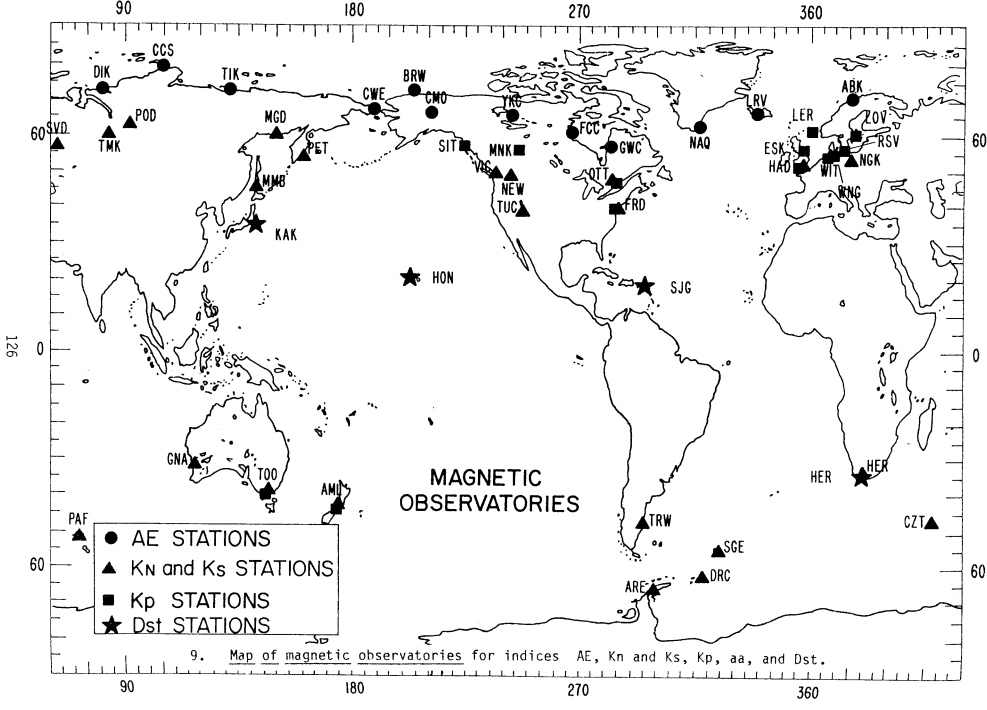


Figure 1.12: Map of ground stations used to measure the K_p , AE , and D_{st} indices. From [Allen, 1982].

day number, sunspot number, whistler profiles, and multiple year-long perturbations in an exponential fashion shown as $n_e(L, d, \bar{R}) = 10^{\Sigma x_i}$. L_{ppi} and Δpp are empirically derived plasmapause location and width, respectively. x_1 is a whistler reference profile, and indices $i = 2 - 4$ represent perturbation values for annual, semiannual, and solar cycle variations respectively. The exact numbers in the density profiles vary slightly between a midnight-06 MLT model, and a 06-15 MLT model, based on the specific passes used to fit the parameters for each section.

Gallagher et al. [2000] created a Global Core Plasma Model which combines empirically derived models of the ionosphere, plasmasphere, and magnetosphere. For the plasmasphere it links plasma density and magnetosphere conditions by fitting Carpenter's equation, but replacing their piecewise dependence on MLT with a sinusoidal term along with extra factors to account for the post-dusk bulge while still keeping the plasmasphere model continuous.

At the most basic level, the plasmasphere component reduces to an exponential equation of the form $n_{ps} = 10^{gh} - 1$, where g and h are terms relating to the inner plasmasphere and plasmapause, combining sunspot number, day of year, and a plasmapause gradient term that accounts for the MLT dependence in the form of $\Delta_{pp} = 0.036 \cdot \sin(\frac{2\pi(MLT-6)}{24}) + 0.14$. They also link plasmasphere filling time to K_p , stating it starts at 3.5 MLT and fills until a time of $\Phi_{TP} = 0.145K_p^2 - 2.63K_p + 21.86$ hours [Gallagher et al., 1995].

Moldwin et al. [2002] build on Carpenter's model by taking CRRES data and the same plasmapause detection parameters as Carpenter, finding 969 plasmapause detections compared to the 40 used to derive the model in Carpenter and Anderson [1992]. Using the abundance of data they do statistical analyses such as showing a least squares linear fit between increasing K_p and decreasing L-shell of the plasmapause of the form $L_{pp} = (5.39 \pm 0.072) - (0.382 \pm 0.019) \cdot K_p(max)$ with a correlation of 0.548. They also find that if they limit this to plasmapause crossings between 09 and 15 MLT, the linear correlation increases to 0.727.

O'Brien and Moldwin [2003] find that using auroral electrojet (AE) or disturbance storm time (D_{st}) indices work better than K_p for determining plasmapause location. They use the same plasmapause crossings as Moldwin et al. [2002] and model them against hourly changes in the ring current (via D_{st}) or 1-minute changes in the auroral electrojet currents (AE). They take the maximum (or minimum, as required) of each index over a varying range of hours, from a start of up to 72 hours before crossing up to end of at least 6 hours before crossing, and fit a basic linear model. Their three best models were a basic linear fit of L_{pp} to $\max_{-36,-2}K_p$, $\max_{-36,0}AE$, and $\log_{10}(\min_{-24,0}D_{st})$. Using a bootstrap analysis for significance, all three models were indistinguishably similar in the root mean square error (RMSE) of their respective models, except for AE having significantly less error in the night sector than D_{st} . Making the model slightly more advanced by including a MLT dependence and periodic terms allows a bulge to be approximated, and finds that the allowing local time to be accounted for significantly (at the 95% confidence level) reduces the error of the

model, but still shows no significant difference between models of the same complexity.

Denton et al. [2006] models the distribution of electrons along magnetic field lines based on measurements from the Radio Plasma Imager onboard the IMAGE spacecraft. They attempt to show that mass density has a local peak near the magnetic equator, and do show that in some cases it can be inferred, especially for values of $L \geq 6$, but can't conclusively establish its existence.

As for models specifically of the plasmatrough, Loto'aniu et al. [1999] take ground based Ultra Low Frequency (ULF) wave measurements, then map them to plasma mass densities between $L = 4.5$ and $L = 10$ via the Tsyganenko T89 magnetic field model and an R^{-4} plasma mass density profile. These estimated values were then compared to in-situ measurements from the CRRES satellite and found that this technique can, under specific conditions where all of the field lines at the ground stations map to plasmatrough, accurately measure plasmatrough mass density.

Takahashi et al. [2006] take a similar approach, but approximate ULF waves from the CRRES satellite directly, instead of using ground stations, and then map that to mass density values. By using the electric field spectra on the satellite and finding a fundamental frequency of the toroidal waves, they estimate mass density with a combination of theoretical model and empirical observations. The magnetic field model used is either T89 or T96, dependent on K_p or D_{st} respectively. Instead of an R^{-4} dependence for the mass density model, they use $\rho = \rho_{eq}(LR_E/R)^{0.5}$, and then combine with frequency observations via $\rho_{eq_est} = \rho_{eq_theory}(f_{1_theory}/f_{1_obs})^2$.

Takahashi et al. [2010] similarly looks at deriving mass density using toroidal Alfvén waves, but switch from using the fundamental harmonic mode to using the third harmonic because it was most detectable at the location of the GOES satellites, which they used in place of CRRES to get a geostationary orbit and larger number of observation points. The methods are largely the same as the previous paper, but include statistics accounting for detection rates of f_{T3} and slight modifications to technique required for the geostationary satellites.

Min et al. [2013] derives equatorial mass density using the GOES and AMPTE satellites by applying magnetoseismology to the toroidal Alfvén waves, confirms the benefits of using the third toroidal frequency as described by Takahashi and Denton, and confirm the statistical properties of the dataset such as f_{T3} being largely undetectable in the midnight region and the high correlation between ρ_{eq} and $F_{10.7}$.

Denton et al. [2015] also uses the GOES satellites to determine mass density at geostationary orbit. They assume the same form of power law as Takahashi et al. [2006] but with a fit power parameter α , making the equation: $\rho = \rho_{eq}(LR_E/R)^\alpha$, then normalize to the third harmonic frequency for data availability. Binning by harmonic frequency, they fit Gaussian curves to MLT, $F_{10.7}$, and AE to get best fit α for the model, and end up getting a model that produces a good average value for field line density.

Most of these studies focus on plasma density in the plasmapause and plasmasphere, since that is where the densities are the highest, easiest to measure, and have the most data availability. This study focuses on the plasmatrough partly due to it's unexplored nature, and largely due to the significance of the region to objects in geostationary orbits. It also couples with both the magnetosphere and plasmasphere, suggesting that a greater understanding of the behavior of the plasmatrough may aid in understanding the coupling of both major bordering regions.

Chapter 2: Methods

This work utilized both linear and nonlinear methods for analysis, modeling, and prediction, including Auto-Regressive Moving Average models with eXogenous inputs (ARMAX) and neural net models. No single method is ideal, and using many methods is better for insight, especially for nonlinear/complex systems. The details of their application will be expanded upon in their respective sections.

2.1 Linear

2.1.1 Overview

Due to its simplicity and ease of application, linear models are used in practically all fields as a first attempt to interpret data and any potential relationships. In Space Physics, where the underlying behavior of a complex system is not theoretically known, and in-situ measurements are sparse, linear models are often the first step towards understanding what components are related and to what degree. Sometimes this leads to understanding unexpected complexities in a system.

2.1.2 ARX

Impulse response systems are systems in which the output (a response) is driven by an input convolved with a linear sum of coefficients (a series of impulses). A simple example would be making a loud noise in a concert hall. The response is the unique echoes and reverberations created by the initial driving sound, and with enough signal, a statistical model can be generated that will map the input sound to a response echo. In the magnetosphere, the most used example is an impulse of vB_S driving the Auroral Electrojet (AE/AL) index

[Bargatze et al., 1985], or the Disturbance Storm Time (D_{st}) index [Clauer et al., 1981]. vB_S is the solar wind velocity multiplied by the southward component of the solar wind magnetic field (i.e. southward components keep their value, northward components are zeroed). A sample result from this model is shown in Figure 2.1

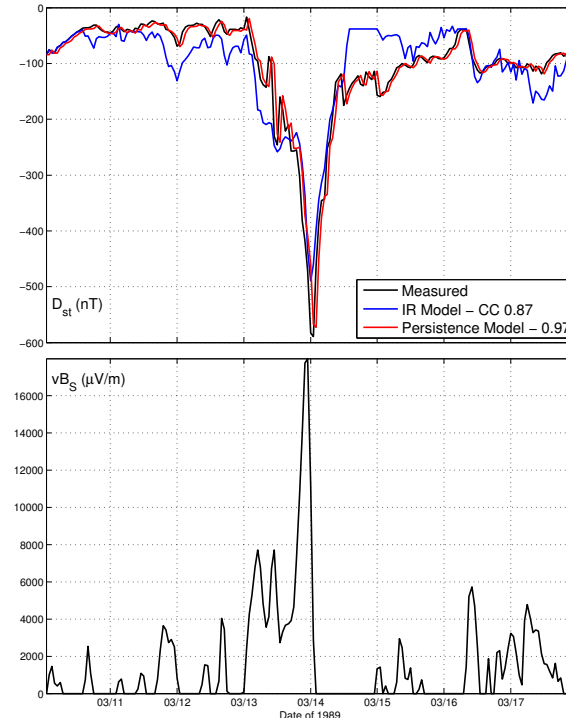


Figure 2.1: (a) D_{st} (black), persistence (red), 12-hour impulse response model (blue). (b) vB_S input.

This plot shows how different models are used to predict magnetospheric variables with varying amounts of success. In this proposal, what starts as a Box-Jenkins model of the form [Weigel, 2007]:

$$x(t) = \sum_{j=1}^m b_j \cdot f(t - j\Delta t) + c_t$$

can be modified to include an auto-regressive component to be an autoregressive model

with exogenous inputs (ARX) such as that used in Klimas et al. [1998], taking the form:

$$\hat{x}(t) = \sum_{i=1}^l a_i \cdot x(t - i\Delta t) + \sum_{j=1}^m b_j \cdot f(t - j\Delta t) + c_t \quad (2.1)$$

Where m and l are the number of coefficients desired for including previous data points in the prediction, and c is a factor to remove the mean offset from the data. Note that in some cases the starting value of the iterators can be individually increased if there is a known delay in response time or there is a desire to predict further into the future. In Klimas et al. [1998], second order equations ($m = 2$) were used with anywhere from one to four driving coefficients, but in practice any number of coefficients and any number of driving variables can be used up to some fraction of the number of data points that allows the coefficient matrices to be solved for.

There generally is a limit to the usefulness of large-lead-time forecasts Ghil et al. [2011]. By looking at a plot of the cross correlation relative to the number of coefficients, a limit will generally be seen where adding more coefficients no longer reduces error in the model. By creating a threshold of change in fit per coefficient added (perhaps via a bootstrap method), the minimum number of coefficients needed to optimally model the system can be determined.

By constructing a linear system of equations from Equation 2.1, the coefficients can be solved for in a general matrix form (where, in this case, $l = m$):

$$\begin{pmatrix} x_0 & \dots & x_{l-1} & f_0 & \dots & f_{l-1} & 1 \\ x_1 & & x_l & f_l & & f_l & 1 \\ \dots & & & & & & \\ x_{N-l} & \dots & x_{N-1} & f_{N-l} & \dots & f_{N-1} & 1 \end{pmatrix} \begin{pmatrix} a_0 \\ \dots \\ a_{l-1} \\ b_0 \\ \dots \\ b_{l-1} \\ c \end{pmatrix} = \begin{pmatrix} x_l \\ x_{l+1} \\ \dots \\ x_N \end{pmatrix}$$

This is a linear model for the behavior of a system. However, it has been shown that the set of coefficients describing the response of a system can change with storm intensity Klimas et al. [1998], the time scale modeled Vassiliadis et al. [2004], and even the time of day Bargatze et al. [1985]. This creates a very large number of possible directions for research, from predicting storm onsets, to predicting storm intensities, to modeling the overall shape and behavior of a storm, as well as all of the other possible interactions outside of storm-time.

2.1.3 ARMAX

A class of model known as an Auto-Regressive Moving Average with eXogenous inputs model (ARMAX) is often used in time series analysis to combine the effects of persistence, linear dependence, and an average that changes with time. It makes a slight change on the ARX model in Equation 2.1, adding the moving average term:

$$\hat{x}(t) = \sum_{i=1}^l a_i \cdot x(t - i\Delta t) + \sum_{j=1}^m b_j \cdot f(t - j\Delta t) + \sum_{k=1}^n e_k \cdot c(t - k\Delta t) + c_t \quad (2.2)$$

2.1.4 Applicability

As implied by the name, an ARMAX model is suitable for analysis of a time-dependent linear system where the value of a measurement is determined by its own persistence, an external variable, and some factor that contributes to a moving average with time. Most linear systems can be encapsulated by this framework, some even being overspecified with this level of accounting for variability.

2.1.5 Caveats and Biases

There will be a number of things that, ideally, must come together to make this kind of data prediction work. For one: ARX methods can often be heavily dependent on a concept known as “persistence”, whereby the best prediction for a variable at any time is that

same variable at the last measured time step. For example, if the high temperature today is 70° , it is fairly likely that the high temperature tomorrow will be near 70° . Too much reliance on persistence forecasting, though, and predictions can lose their usefulness. Figure 2.1, for example, shows how a model can achieve high correlation with persistence, but be almost entirely useless for predicting events before they happen since the spikes are never anticipated, just modeled after they have been observed. Also, if the time of interest is multiple time-steps ahead, a simple persistence forecast becomes less and less accurate with each step.

The other major problem in forecasting is that of lead time. Being able to forecast a storm one minute in advance is generally not enough time for operators to take mitigating action.

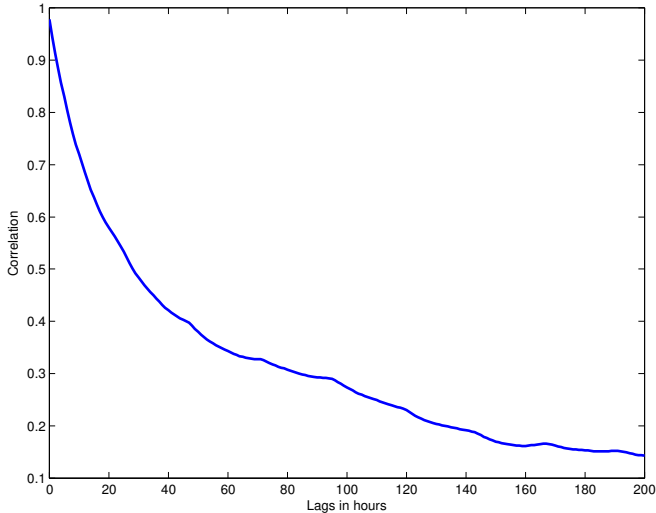


Figure 2.2: Correlation between prediction and measurement vs lead time of forecast

Figure 2.2 shows the correlation of a set of predictions made for autocorrelation in the disturbance storm time index (D_{st}) against the amount of lead time in the forecasts. This metric is a measure of how much disturbances in the magnetosphere induce currents in ground-based electrical systems. The predictions were made further and further in time from the current magnetic field and D_{st} measurements, with decreasing accuracy as the

predicted time got further from the current time. While an accurate prediction can be made one hour in advance, a prediction 3 days in advance has almost no correlation with what was measured. This is one of the main problems that this dissertation hopes to address.

Mean vs Median

The question of whether to use means or medians for analysis is based on what facets of the data are most important to the research. Since means are biased towards outliers and medians biased against them, the decision rests on how much weight should be given to outliers (or extreme values) in a study. For example, when looking at long-term solar wind variables, intermittent spikes may not be relevant to the overall pattern of behavior being analyzed, but knowing that on a short time scale a certain day had a noticeable spike may be important. In the former case, using the median would likely be best, and using the mean for the latter. However, space physics often deals with skewed distributions and sparse data, leading to an uncertainty of which method is best, so both are analyzed with their respective traits in mind.

As an example, Figure 2.3 shows a plot where data for multiple events is split into bins based on the average value of a binning variable, and then significance tests performed for each hour of the event to determine if the variable behaves differently based on bin. In this case, where the same events is used for both methods, when using means as the method of averaging the hours have far more variability and are thus seen to have less significance, whereas using medians finds over twice as many significant hours, as well as a clearly more divisive behavior.

Effects of time averaging

Similarly to the mean vs median question, the decision on if/how much to average the data over time will affect the resulting time series to be biased against intermittent spikes in value. The more time added to any particular average, the less impact any short-term

changes will have on the final value.

2.1.6 Summary

Because linear models are simple, optimizable, and adequately model many physical systems, they are a useful first choice for trying to determine the behavior of mass density in the plasmatrough. The relationships between solar wind, plasmatrough, and plasmasphere may also be detectable on the first order approximation by a linear model if not entirely linear in nature.

2.2 Nonlinear

2.2.1 Overview

While many nonlinear systems are approximated by a number of localized linear models for the sake of simplicity and ease of interpretation, the design and implementation of nonlinear models has become greatly simplified in recent years. Their use allows for determining nonlinear structure without pre-assuming any localization of the data, and as such were used to attempt forecasting in this dissertation. The first choice was a model based on neural networks [Hernandez et al., 1993, Bala and Reiff, 2012] which approximates a non-linear system given a set of training data. The usefulness of this is apparent in a few key points: the weights of contribution of any particular variable to a system will likely be nonlinear in some fashion (e.g. a ground station's measurements will depend on sunlight heating the ionosphere which depends on latitude, time of year, and time of day), and allowing for the non-linear effects of saturation where perhaps the magnetosphere will behave differently after reaching certain levels of particle density or electric potential, rather than directly scaling regardless of limits.

Another algorithm known as Principal Component Analysis (PCA) can be used to take the large number of possible variables and define an orthogonal set of vectors that most efficiently encapsulate the variance in the data. By doing this, the number of variables

needed for computing any linear or non-linear algorithm can be reduced and optimized, making predictions quicker while maintaining most of the predictive benefits of using all possible data, as well as indicating which variables contain the most information relevant to the predictions.

2.2.2 Neural Networks

2.2.3 Applicability

Nonlinear models are applicable when a system has more complexity than can be encapsulated by a linear model. Since they're usually a class of model that trains adaptive weights that can be tuned by known inputs and outputs, they're especially useful for systems where a large amount of training data are available.

2.2.4 Caveats

Nonlinear models can be susceptible to overfitting, since they inherently attempt to fit more complexity than a linear model, but can also be controlled via the number of inputs and weights used. They also may suggest more structure than might truly exist. Both of these problems are lessened by training with more data, if available. Figure 2.4 shows a comparison of predicting equatorial mass density (ρ_{eq}) with the $F_{10.7}$ index and the disturbance storm time index (D_{st}). The neural net models (left) shows much more structure than the linear models (right) despite being given the same data. Whether that structure reflects any real physical phenomenon, however, is a difficult problem to answer, and so both models are often compared to attempt to ascertain what structure may be valid.

Sometimes, as in the top two plots of Figure 2.4, the structure seems to support the same conclusion where the nonlinear model just adds slight detail. Othertimes, as in the case of the lower two plots, the results seem discrepant. The linear model indicates increasing ρ_{eq} with increasing B_z and increasing $F_{10.7}$, while the nonlinear model shows a more nuanced structure with increased ρ_{eq} showing up with lower B_z values, and at a range of $F_{10.7}$ values. Situations like these require further analysis to determine the true underlying structure.

2.2.5 Comparison to Linear Model

Nonlinear models differ from linear models by incorporating some method for accounting for effects within a domain that are not seen across the entire domain. Though both models can be given the same inputs, and trained on the same outputs, the models themselves can fundamentally differ. Linear models are also generally simple to interpret (e.g. $y = 2 * x$ means for every change in x , y changes by double that amount.) Nonlinear models, on the other hand, often have no simple interpretation and must be approached by testing for a range of parameters in the model to map out resulting outputs and make some interpretation of the underlying structure.

Nonlinear models can be compared to a linear model of the same data in order to assess the usefulness of accounting for nonlinear features. If both models result in similar correlation values, it can be said that the nonlinear model offers no extra insight into the structure of the system and the relationships therein.

2.2.6 Summary

Nonlinear models are a useful addition to linear models by allowing for better approximations to more complex physical systems, where the entire system may not fit a linear model or may have localized dependencies.

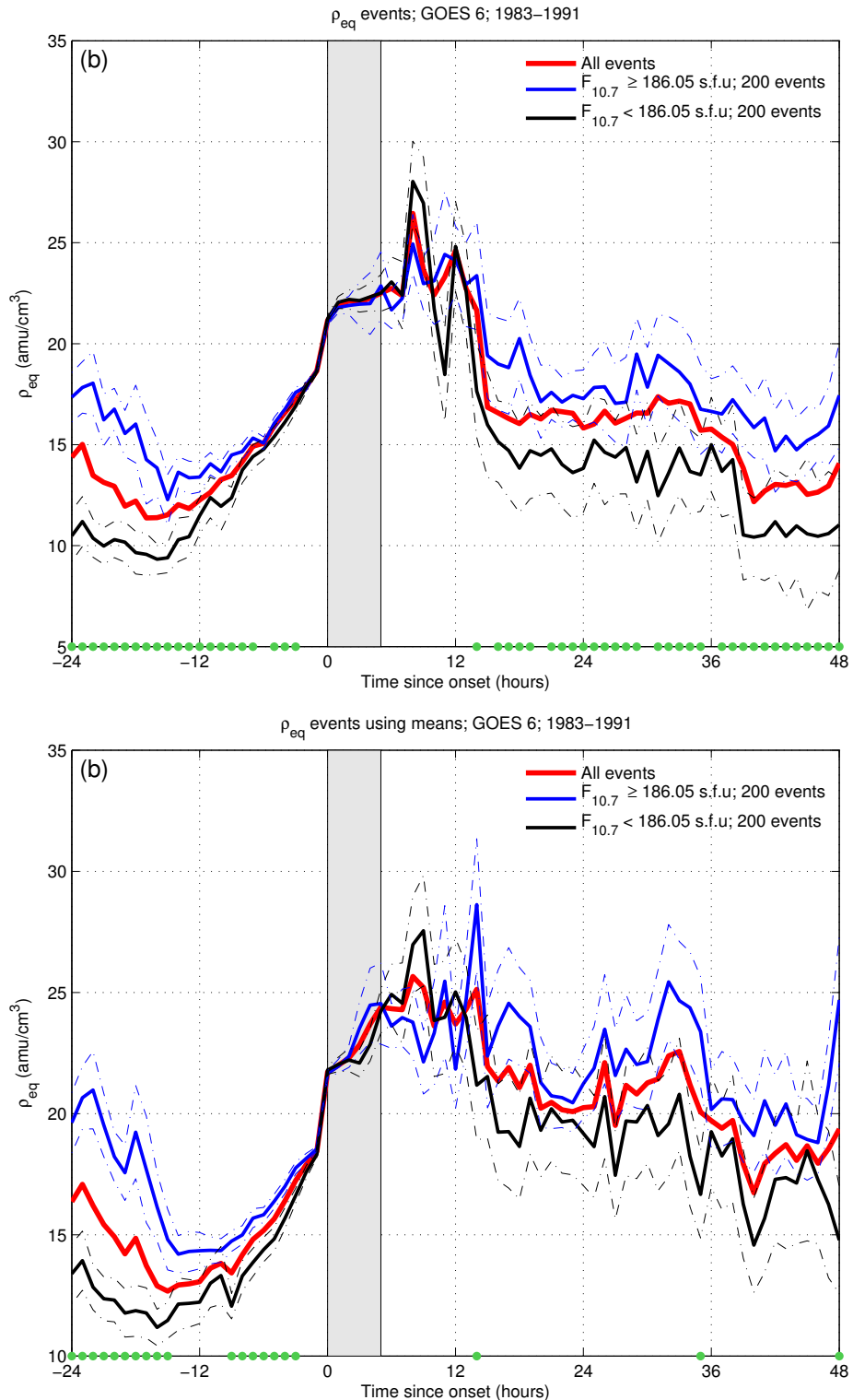


Figure 2.3: Effect of using means over medians. Top: Events averaged using median values. Bottom: Events averaged using mean values.

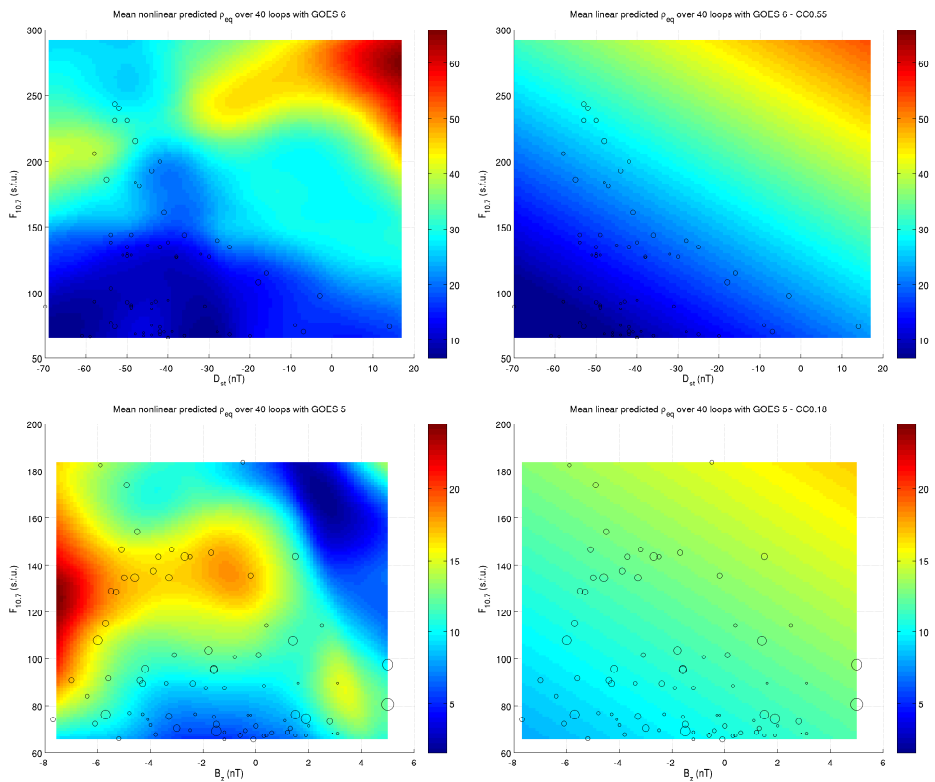


Figure 2.4: Nonlinear models (left) vs linear models (right) of ρ_{eq}

Chapter 3: Measurements

The measurements can, to a certain extent, be broken into three main components: those pertaining to the solar wind and solar corona, those from the magnetosphere in general, and those specific to the plasmasphere. The combined data sources used in this dissertation are shown in Figure 3.1, providing solar wind variables B_z and V_{SW} , solar variable $F_{10.7}$, plasmatrough variable ρ_{eq} , and magnetosphere variable D_{st} .

Similarly, Figure 1.5 earlier showed the same variables before, during, and after the March 1989 geomagnetic storm as seen by GOES 6. This makes it clearer how the variables are interrelated, notably how short-timescale effects such as drops in B_z and D_{st} are connected, or longer time scale changes in $F_{10.7}$ and V_{SW} are related. It also shows how the sparse availability of ρ_{eq} created challenges for this study, which is discussed in more detail later in Section 3.2.2.

Figure 3.2 shows four more selected examples of short time periods with interesting characteristics. They all show, to a varying degree, an elevated solar wind velocity coinciding with a drop in D_{st} , and almost always also an enhancement in southward B_z . The bottom right panel also appears to show how an extended period of no activity allows the plasmasphere to refill.

3.1 Solar Wind

The solar wind is the primary source of particles for the magnetosphere, and as such is an important input for a plasmatrough model. Conditions such as magnetic field orientation and particle velocity are important considerations for whether the plasmasphere is expected to be compressed, saturated, or experiencing high variability. By adding these to a model that includes time delayed inputs, their effects can be accounted for and aid in categorizing

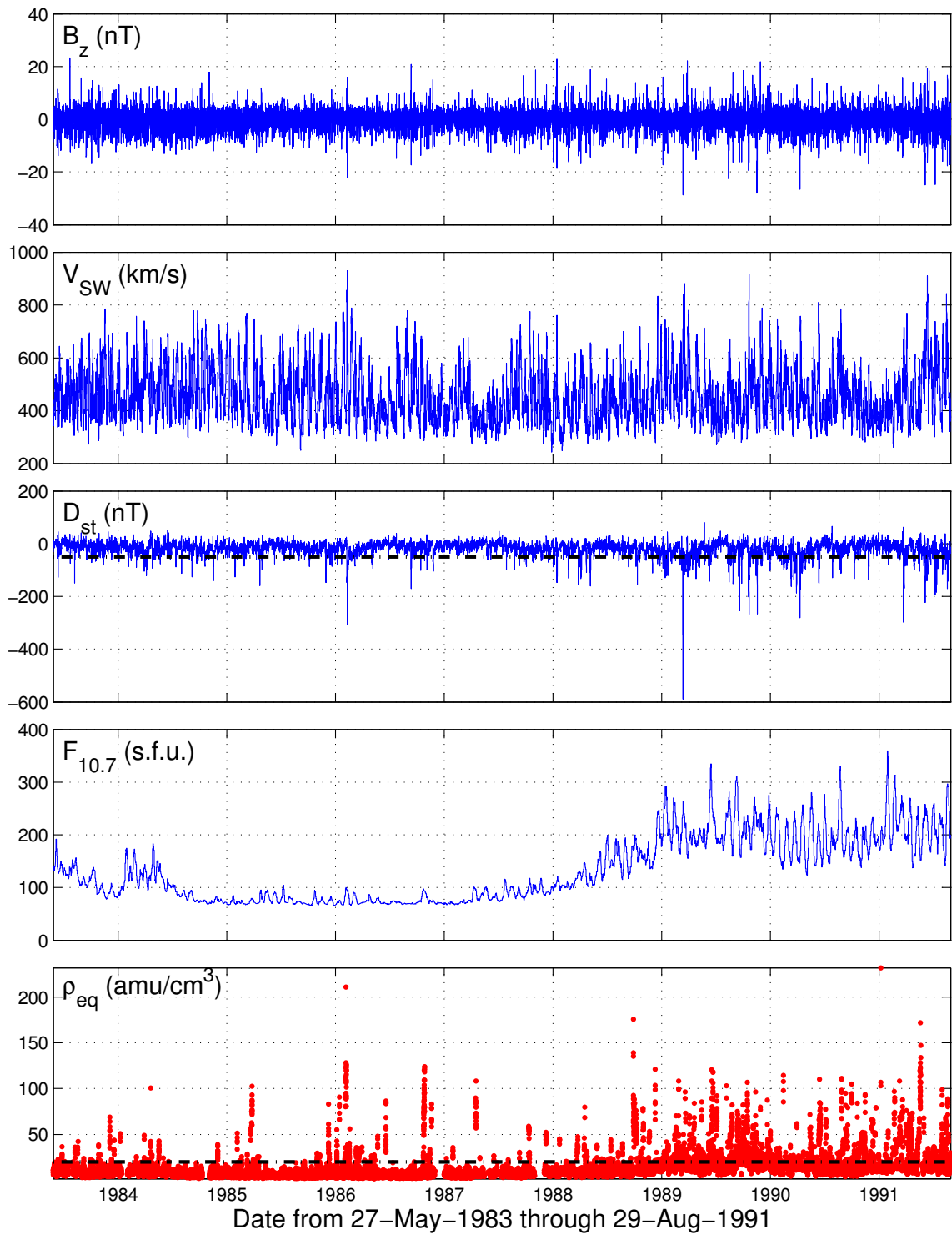


Figure 3.1: Data from GOES 6 with dashed lines indicating default event thresholds discussed in Chapter 4.

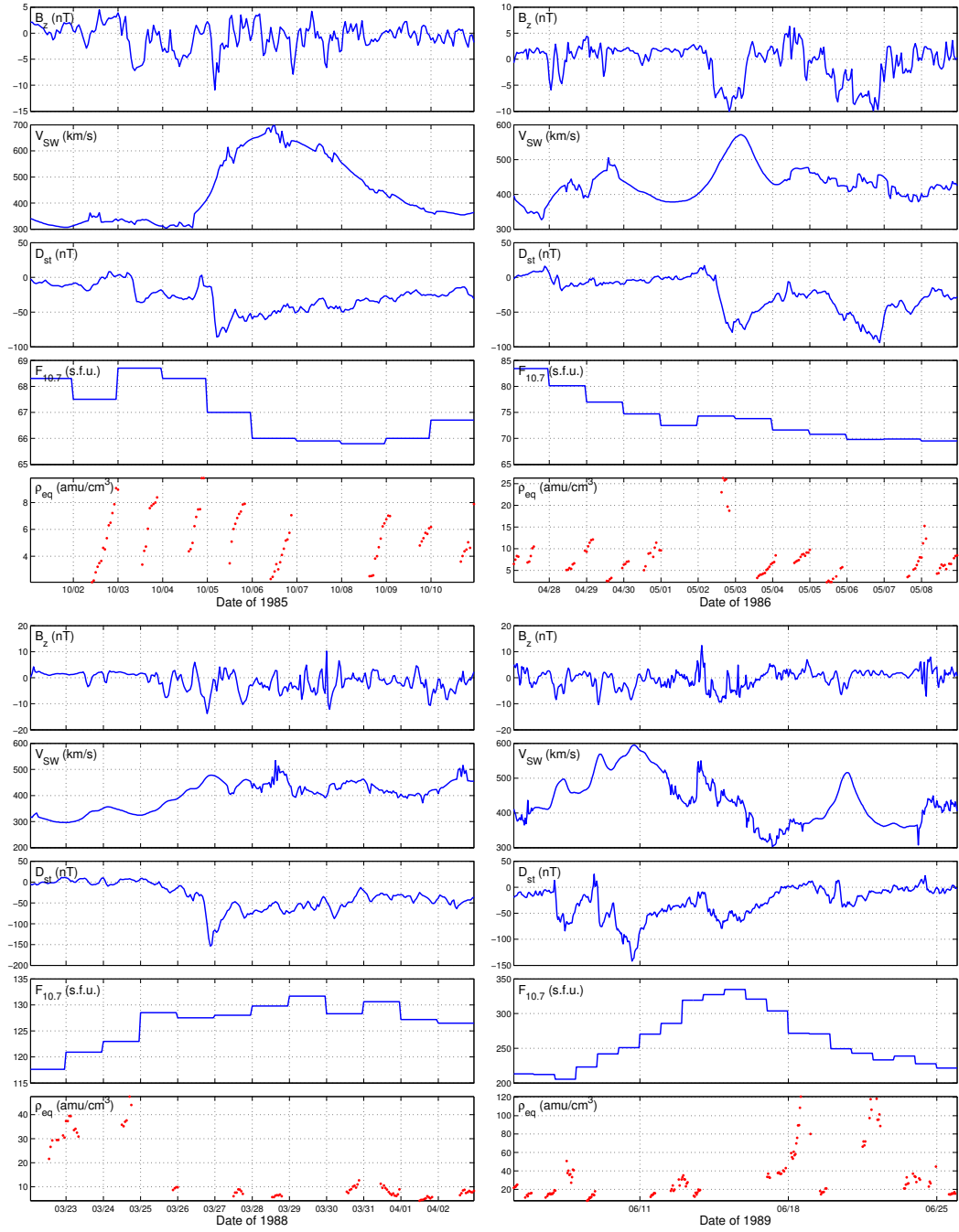


Figure 3.2: Four examples of specific events from GOES 6.

the state of the plasmatrough.

3.1.1 Source

Solar wind data for this dissertation is provided by the OMNIWeb service [King and Papi-tashvili, 2005], which contains data from multiple satellites and is uniform in time, supplying a near-Earth set of solar wind measurements. The one-hour resolution dataset was used since the study is concerned with effects on timescales of longer than an hour, and to more easily compare to the other data sources used.

Since the OMNIWeb data has gaps for some of the variables, the dataset developed for Kondrashov et al. [2014] was used as they reliably reconstruct gaps to make a continuous, uniform data set. They used Singular Spectrum Analysis to create a set of principle components and empirical orthogonal functions to find that the data contained significant oscillatory modes. This allowed the reconstruction of gaps in solar wind driving variables by using continuously observed responses such as geomagnetic indices.

3.1.2 Coverage

Low resolution (1-hour cadence) OMNI data is available from 1963 to present, but only the years of 1983-1992 were considered as they overlapped with the other data sets of interest. The data covers, but is not limited to: magnetic field magnitude in all three dimensions; solar wind proton density and temperature; and the K_p , AE , $F_{10.7}$, and D_{st} indices.

3.1.3 Data preparation

The only data cleaning required on the OMNI dataset was to convert fill values of 999.9 and 9999 to NaN, to be appropriate for use in data analysis so they would not be included in calculations. Of the variables included (see Coverage), B , B_z (GSE and GSM), and Solar wind proton number density and plasma speed all were missing about 35% of their data. The AE index was missing about 7% of its data, and all other variables had no time gaps.

3.2 Geomagnetic

Geomagnetic data cover everything inside the magnetopause, extending out to a distance of roughly $10R_E$ on the sunward side of Earth.

3.2.1 Source

The data come from Takahashi et al. [2010], which takes data from the Geostationary Operational Environmental Satellites (GOES) and uses a set of magnetic field models to relate Alfvén waves to equatorial mass density (ρ_{eq}). By taking magnetic field vectors and applying spectral analysis, they find a set of fundamental harmonic frequencies of toroidal waves. Through testing, they find a strong linear dependence of the 27-day average third toroidal frequency (f_{T3_27d}) on the similarly averaged $F_{10.7}$ index, of the form: $f_{T3_27d}(mHz) = 37.5 - 0.0972F_{10.7_27d}(sfu)$. From there, they also find a linear relationship to the averaged ρ_{eq} in the form $\log_{10}(\rho_{eq_27d}) = 0.421 + 0.00390F_{10.7_27d}$, effectively linking the derived toroidal frequency to ρ_{eq} .

3.2.2 Coverage

The GOES satellites used in this study cover the years from 1980 to the end of 1991, often with overlapping years between satellites. The satellites themselves held a geostationary orbit at around $6.62 R_E$ and collected data on a roughly 3-second cadence [GOE], which was then transformed onto a 10-minute cadence. Their radial position means they are almost always measuring properties of the plasmatrough, the region devoid of dense plasma located just outside the plasmasphere. Figure 3.3 shows the location of the GOES satellites relative to the magnetopause in the top panel, while also showing that the plasmapause location tends to vary from 2-6 R_E depending on magnetic activity.

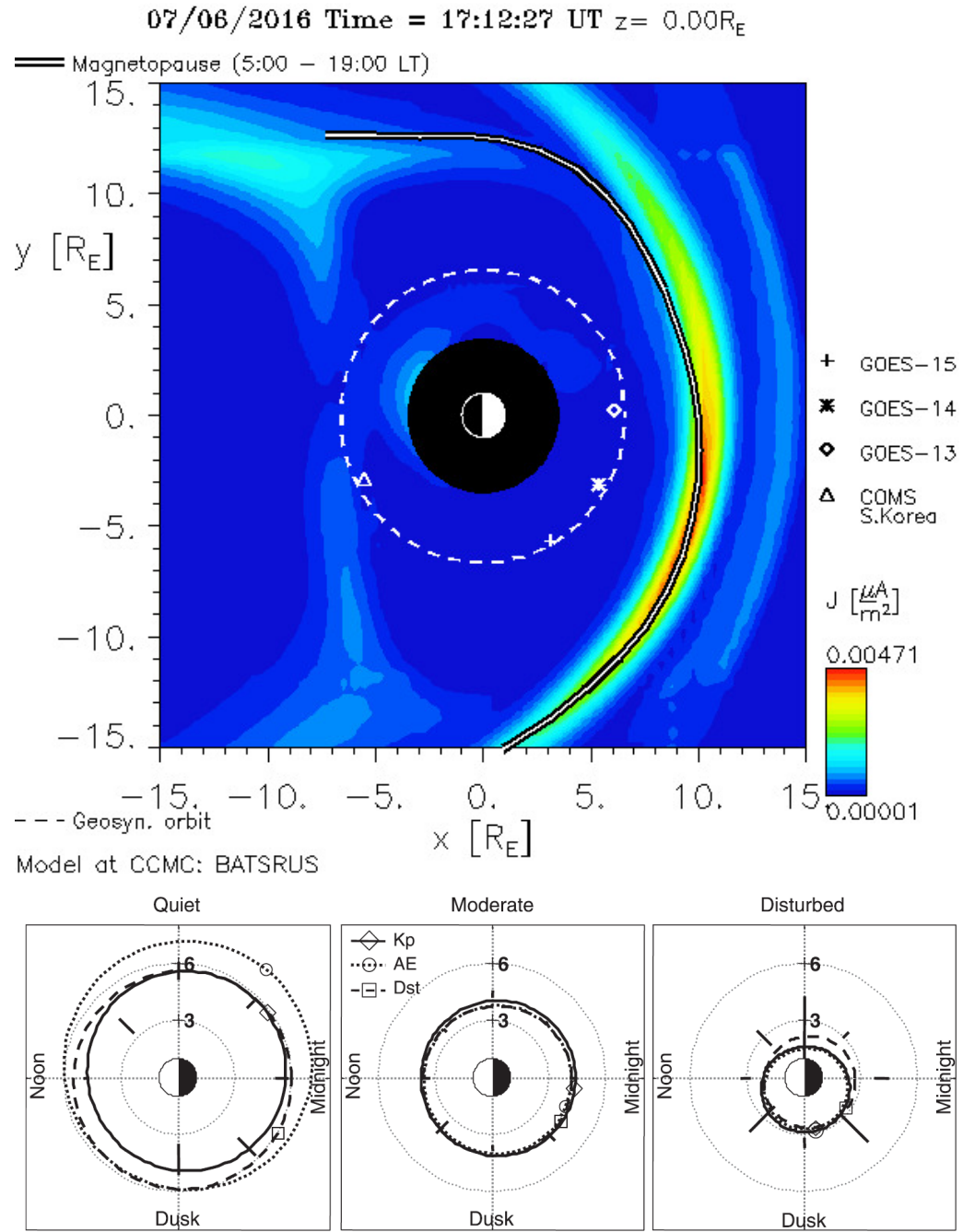


Figure 3.3: Top: Model of magnetopause location showing location of GOES satellites in geosynchronous orbit. From [CCMC], taken during a period of $K_p=4$. Bottom: Model of plasmapause location as it varies with geomagnetic activity where the symbols indicate the local time of maximum plasmapause location. From [O'Brien and Moldwin, 2003]

3.2.3 Data preparation

The data were prepared by replacing fill values of 9999 with NaN and then narrowing results to only one satellite at a time to ideally remove any effects of satellite position or calibration from the results. These data still had many temporal gaps (roughly 22% of the 10-minute intervals between the first and last point of GOES 6 had any data, since the detection rate of the relevant frequency in the toroidal waves (f_{T3_30m}) varied with local time, magnetic latitude, and the strength of the compressional source waves [Takahashi et al., 2010]), so they were placed onto a uniform 10-minute grid leaving missing points as NaN, allowing for easier data analysis and comparison to other data sets. The detection rate as a function of magnetic latitude and magnetic local time is shown in Figure 3.4.

In order to align the GOES data with the OMNI 1-hour cadence, the median of all existing 10-minute values within an hour was treated as the value for that hour (i.e. the median of all values from 7:00-7:59 was the value for 7:00). This was done to match the OMNI standard, and showed no significant difference on our timescales as using a centered median. For hours with no existing values, a NaN was inserted to keep the cadence uniform.

3.3 Plasmasphere and Plasmatrough

Plasmasphere data covers the inner regions of the magnetosphere, bounded by the plasma-pause on the outer edge and the ionosphere on the inner edge. This puts it at a typical distance of $L = 3 - 5R_E$ [Carpenter and Anderson, 1992].

3.3.1 Source

Data for the plasmasphere also comes from the GOES and OMNI datasets previously discussed, but are often calculated as extensions of directly measured data either onboard the satellites or from ground stations, depending on the current extent of the plasmasphere and location of the satellite.

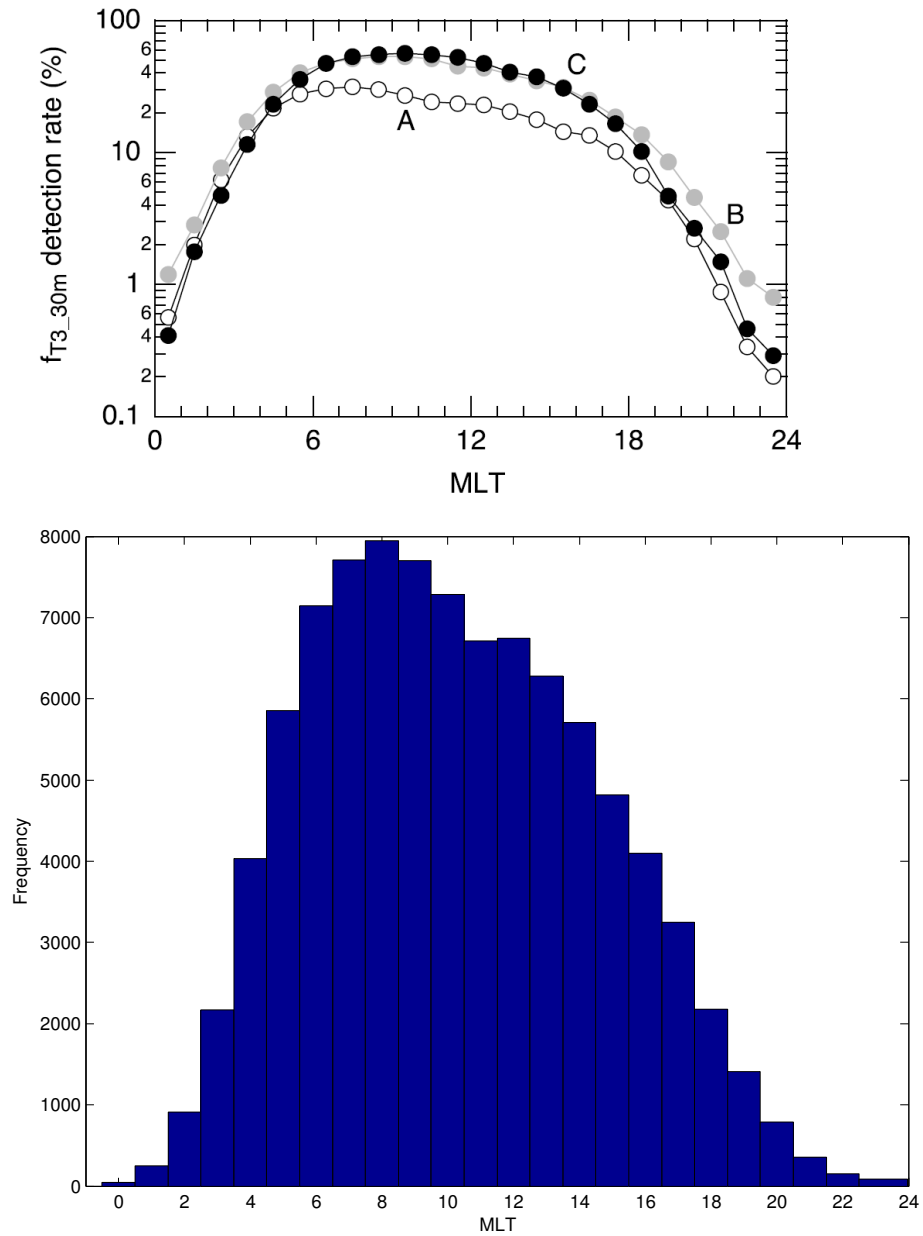


Figure 3.4: Top: Detection rate of $f_{T3\text{-}30m}$ for magnetic latitudes of 5, 9, and 11 degrees (curves A, B, and C respectively). From [Takahashi et al., 2010]. Bottom: MLT of all available data

3.3.2 Coverage

Since the data come from the same sources as that of the magnetosphere, the coverage is largely the same with specifics covered in Takahashi et al. [2010], as the satellites used most often reside in the plasmatrough. Figure 3.5 shows the typical locations of the plasmapause, and how this puts the GOES satellites firmly in the plasmatrough at $6.6R_E$.

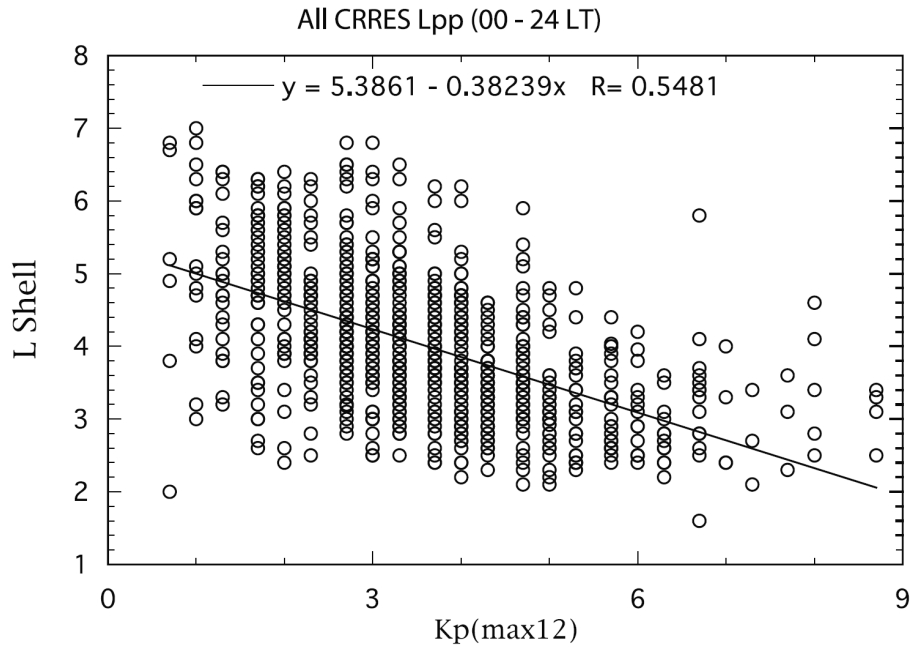


Figure 3.5: Location of detected plasmapause on CRRES against the maximum K_p value for the previous 12 hours. From [Moldwin et al., 2002]

3.3.3 Data preparation

The same preparation done for the magnetosphere applied to the plasmasphere data. Some specific analysis done in Takahashi et al. [2010] discusses how the spacecraft's geomagnetic location affected their ability to detect the necessary toroidal frequency, and thus estimate ρ_{eq} , so for some of the long-timescale averages, only certain MLTs were included. They also show that ρ_{eq} inversely correlates with geomagnetic activity (and, by extension, plasmapause

location), so during long periods of no activity the plasmasphere extends beyond geosynchronous orbit, leading to measurements of ρ_{eq} reflecting density in the plasmasphere and not the plasmatrough.

Chapter 4: Analysis

4.1 Overview

While Figure 3.1 shows an overview of the most pertinent variables used in this study, some further analysis was done to determine any potential biases introduced by specifics of the satellite motion or derivations used. For example, where Figure 3.4 shows that not only did data availability vary significantly with magnetic local time (MLT), Figure 4.1 shows that the values themselves also vary significantly with MLT. This leads to different models being better at particular times, such as AE models being better in the dawn sector and D_{st} models being better at dusk [O'Brien and Moldwin, 2003]. The concept of MLT having a strong effect on plasmospheric behavior has been well established all the way back to the initial whistler profiles of the plasmapause [Carpenter, 1966].

4.2 Linear Correlations

This dependence was further investigated, and extended, by creating a simple linear model for each major variable in the database as well as combinations of some to investigate independent contributions to the total correlation (by testing how much correlation improved in a combined model over either of the constituent models.) The inputs were the median values of each variable for four hours before a D_{st} event onset, and they were trained to predict a median of the value at onset with the four hours following it. The models were trained on half of the dataset and tested on the other half for each satellite, and this was repeated with new random samples 100 times and then the median correlation values were taken. The results are shown in Table 4.1.

It can be seen that $F_{10.7}$ almost always correlates the best with ρ_{eq} , but that there is

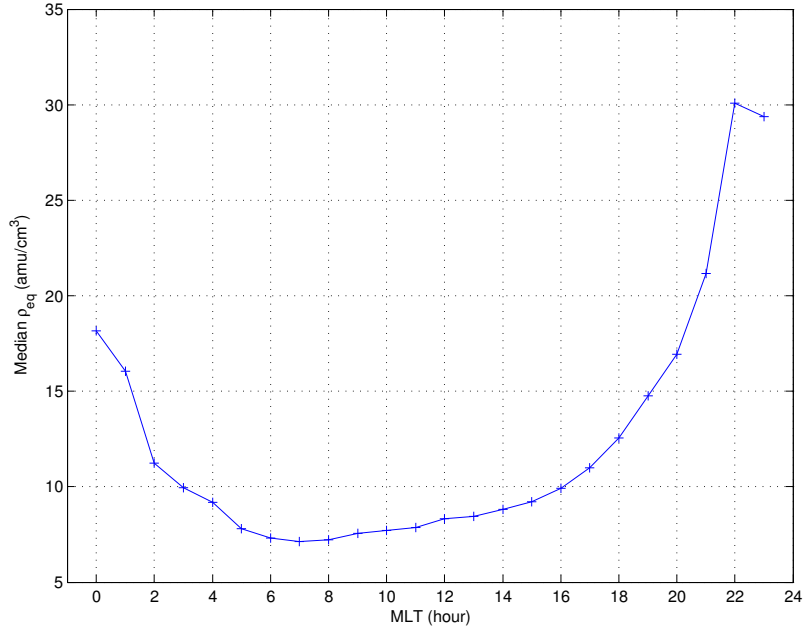


Figure 4.1: Median ρ_{eq} binned by magnetic local time

	GOES 2	GOES 5	GOES 6	GOES 7
DoY	-0.08 ± 0.08	$+0.14 \pm 0.13$	-0.06 ± 0.06	$+0.09 \pm 0.10$
MLT	-0.10 ± 0.21	-0.07 ± 0.12	$+0.01 \pm 0.23$	-0.06 ± 0.05
B_z	$+0.16 \pm 0.21$	-0.13 ± 0.15	$+0.08 \pm 0.14$	-0.07 ± 0.06
V_{sw}	-0.04 ± 0.10	$+0.27 \pm 0.09$	$+0.06 \pm 0.11$	-0.06 ± 0.06
D_{st}	$+0.26 \pm 0.17$	$+0.66 \pm 0.08$	$+0.06 \pm 0.13$	$+0.23 \pm 0.14$
ρ_{sw}	$+0.35 \pm 0.24$	$+0.63 \pm 0.31$	$+0.12 \pm 0.19$	$+0.36 \pm 0.17$
$F_{10.7}$	$+0.43 \pm 0.08$	$+0.12 \pm 0.12$	$+0.51 \pm 0.06$	$+0.40 \pm 0.06$
$B_z + V_{sw}$	$+0.11 \pm 0.17$	$+0.20 \pm 0.17$	$+0.12 \pm 0.10$	-0.12 ± 0.06
$D_{st} + F_{10.7}$	$+0.44 \pm 0.09$	$+0.71 \pm 0.08$	$+0.54 \pm 0.07$	$+0.47 \pm 0.06$
<i>All</i>	-0.03 ± 0.19	$+0.34 \pm 0.27$	$+0.61 \pm 0.11$	$+0.40 \pm 0.12$

Table 4.1: Table of linear model correlations showing the median of 100 random samples. Each sample trained on half of the data (via randomly selected rows of the least squares matrix) and tested on the other half.

significant variance between data from different satellites. D_{st} also tends to correlate well, but when making a linear model that combines both $F_{10.7}$ and D_{st} , not much improvement is gained suggesting a high degree of collinearity between the two.

Table 4.2 shows the difference between the correlation values for the training set and

$Tr - T$	GOES 2	GOES 5	GOES 6	GOES 7
DoY	$+0.16 \pm 0.11$	$+0.02 \pm 0.16$	$+0.12 \pm 0.08$	-0.01 ± 0.12
MLT	$+0.26 \pm 0.25$	$+0.16 \pm 0.14$	$+0.16 \pm 0.26$	$+0.11 \pm 0.07$
B_z	$+0.06 \pm 0.24$	$+0.27 \pm 0.18$	$+0.05 \pm 0.17$	$+0.14 \pm 0.08$
V_{sw}	$+0.11 \pm 0.13$	$+0.02 \pm 0.13$	$+0.03 \pm 0.13$	$+0.12 \pm 0.08$
D_{st}	$+0.02 \pm 0.21$	$+0.01 \pm 0.12$	$+0.06 \pm 0.16$	$+0.00 \pm 0.17$
ρ_{sw}	$+0.01 \pm 0.29$	$+0.01 \pm 0.37$	$+0.04 \pm 0.22$	-0.03 ± 0.21
$F_{10.7}$	-0.01 ± 0.11	$+0.04 \pm 0.16$	$+0.00 \pm 0.08$	$+0.03 \pm 0.08$
$B_z + V_{sw}$	$+0.15 \pm 0.20$	$+0.17 \pm 0.20$	$+0.08 \pm 0.12$	$+0.24 \pm 0.08$
$D_{st} + F_{10.7}$	$+0.05 \pm 0.12$	-0.02 ± 0.11	$+0.01 \pm 0.10$	$+0.03 \pm 0.08$
All	$+0.64 \pm 0.22$	$+0.54 \pm 0.28$	$+0.16 \pm 0.14$	$+0.25 \pm 0.13$

Table 4.2: Table of differences in linear training-testing models, where each correlation is the median correlation of 100 random samples. Each sample trained on half of the data (via randomly selected rows of the least squares matrix) and tested on the other half.

the test set. This is intended to show which variables are more susceptible to overfitting, since they would tend to correlate well with the training set but not the test set and end up having a large difference. The variables that had good test correlation ($F_{10.7}$ and D_{st}) also had small differences, indicating they were actually good predictors. The models that benefited from an abundance of data to fit (such as using all variables), or those that had a simple linear structure easy to fit to anything (DoY and MLT), had large differences due to being highly overfit to the training set.

4.3 Nonlinear Correlations

Similarly for a neural net model with the same input and target structure as the linear model, but training on a randomly selected 70% of the data, testing on another 15%, and validating on the remaining 15%, Table 4.3 shows the resulting correlation values for the validation data set.

It should be noted that nonlinear modeling is generally more susceptible to overfitting than linear modeling due to the higher order of fitting done on training and validation data, the use of more fit parameters for similarly structured models, as well as the lack of a straight-forward optimal error-minimization method such as least squares regression. This is why some models, such as that including every possible variable, correlate worse

	GOES 2	GOES 5	GOES 6	GOES 7
DoY	$+0.05 \pm 0.31$	$+0.31 \pm 0.30$	$+0.32 \pm 0.22$	$+0.12 \pm 0.17$
MLT	$+0.29 \pm 0.41$	$+0.15 \pm 0.34$	$+0.40 \pm 0.32$	$+0.17 \pm 0.21$
B_z	$+0.24 \pm 0.23$	$+0.21 \pm 0.28$	$+0.17 \pm 0.19$	-0.00 ± 0.20
V_{sw}	$+0.20 \pm 0.25$	$+0.36 \pm 0.19$	$+0.19 \pm 0.24$	$+0.06 \pm 0.18$
D_{st}	$+0.08 \pm 0.27$	$+0.18 \pm 0.25$	$+0.02 \pm 0.17$	$+0.18 \pm 0.24$
ρ_{sw}	$+0.02 \pm 0.29$	$+0.25 \pm 0.42$	$+0.20 \pm 0.22$	$+0.12 \pm 0.29$
$F_{10.7}$	$+0.26 \pm 0.27$	$+0.32 \pm 0.29$	$+0.48 \pm 0.25$	$+0.36 \pm 0.15$
$B_z + V_{sw}$	$+0.11 \pm 0.25$	$+0.20 \pm 0.38$	$+0.15 \pm 0.21$	$+0.02 \pm 0.17$
$D_{st} + F_{10.7}$	$+0.17 \pm 0.25$	$+0.21 \pm 0.32$	$+0.47 \pm 0.15$	$+0.35 \pm 0.17$
<i>All</i>	$+0.21 \pm 0.41$	$+0.67 \pm 0.40$	$+0.60 \pm 0.35$	$+0.17 \pm 0.33$

Table 4.3: Table of nonlinear model test correlations showing the median of 100 random samples. Each sample trained on half of the data (via randomly selected rows of the least squares matrix) and tested on the other half.

$Tr - T$	GOES 2	GOES 5	GOES 6	GOES 7
DoY	$+0.48 \pm 0.36$	$+0.17 \pm 0.33$	$+0.18 \pm 0.24$	$+0.27 \pm 0.23$
MLT	$+0.31 \pm 0.40$	$+0.28 \pm 0.42$	$+0.31 \pm 0.36$	$+0.28 \pm 0.26$
B_z	$+0.14 \pm 0.27$	$+0.29 \pm 0.33$	$+0.20 \pm 0.27$	$+0.20 \pm 0.19$
V_{sw}	$+0.27 \pm 0.31$	$+0.22 \pm 0.31$	$+0.20 \pm 0.27$	$+0.24 \pm 0.19$
D_{st}	$+0.37 \pm 0.32$	$+0.27 \pm 0.32$	$+0.18 \pm 0.21$	$+0.21 \pm 0.24$
ρ_{sw}	$+0.31 \pm 0.30$	$+0.16 \pm 0.42$	$+0.24 \pm 0.27$	$+0.47 \pm 0.37$
$F_{10.7}$	$+0.19 \pm 0.28$	$+0.19 \pm 0.29$	$+0.15 \pm 0.25$	$+0.18 \pm 0.26$
$B_z + V_{sw}$	$+0.28 \pm 0.31$	$+0.26 \pm 0.32$	$+0.28 \pm 0.22$	$+0.23 \pm 0.19$
$D_{st} + F_{10.7}$	$+0.30 \pm 0.29$	$+0.20 \pm 0.32$	$+0.14 \pm 0.19$	$+0.20 \pm 0.16$
<i>All</i>	$+0.51 \pm 0.58$	$+0.47 \pm 0.60$	$+0.41 \pm 0.36$	$+0.46 \pm 0.43$

Table 4.4: Table of differences in nonlinear training-testing models, where each correlation is the median correlation of 100 random samples. Each sample trained on half of the data (via randomly selected rows of the least squares matrix) and tested on the other half.

than models of just a few parts. Where a linear model can minimize error by zeroing out variables without useful information, the neural net will try to incorporate the information anyway and end up overfitting. Table 4.4 shows how significant the differences are between training data and testing data by subtracting the median correlations from both data sets from each other, and doing the root mean squared (RMS) error as the combination of the two constituent errors.

4.4 ARX

In an effort to combine the usefulness of linear models with the adaptability of nonlinear models, a number of ARX models were made to find if they could predict ρ_{eq} given variables over a number of time lags as input. Two forms were made: one with a 1-hour time lag, essentially a normal linear model predicting ρ_{eq} using each variable, and one with 24 hours of lags for each included variable. Each model would generate a matrix of the form shown in Chapter 2, bootstrap sample all the rows 100 times generating a set of ARX coefficients each time, the take the mean of those coefficients for the model used to reconstruct the target timeseries. The correlation between this reconstruction and the target is then printed to a table, a subset of which is shown in Table 4.5.

	CC-1	CC-24
<i>DoY</i>	+0.02	+0.04
<i>Hour</i>	+0.07	+0.27
B_z	+0.14	+0.22
V_{sw}	+0.20	+0.21
D_{st}	+0.03	+0.05
K_p	+0.10	+0.10
ρ_{sw}	+0.07	+0.08
$F_{10.7}$	+0.43	+0.45
$B_z + V_{sw}$	+0.24	+0.29
$B_z + Hour$	+0.16	+0.32
$B_z + F_{10.7}$	+0.45	+0.49
$Hour + F_{10.7}$	+0.44	+0.48
$D_{st} + F_{10.7}$	+0.44	+0.46
<i>All</i>	+0.56	+0.61

Table 4.5: Table of ARX model correlations created from the mean of 100 bootstrap models. CC-1 models have one hour of time lag, and CC-24 have 24 hours of time lags.

It is interesting to note which variables correlate just as well on an hourly timescale as on a daily timescale (e.g. $F_{10.7}$) compared to those which show significant improvement as more time is added to the model (e.g. Hour). The collinearity of some models is also interesting, such as how adding an hourly component doesn't aid the $F_{10.7}$ model much, but does significantly help the B_z model. Also, adding one hour of persistence to the model

increases the correlation to $0.88 - 0.91$ for all of the models.

4.5 Epoch Analyses

In an effort to determine the typical behavior of an event, analyses were done for a number of different conditions where all variables were averaged over a window surrounding the event onset. This should reduce the noise of individual events and show the overall trends inherent in the system during different types of events. For example, Figure 4.2 shows the data for D_{st} events where D_{st} dropped below -50 nT. This finds 668 such events over the span of time covered by GOES 6. Taking the median of each variable across all events for each time step (an hour, in this figure), the general trend is plotted for B_z , V_{SW} , D_{st} , $F_{10.7}$, and ρ_{eq} . The red dashed lines indicate one standard error of the mean from all of the valid points used to compute the median, and the number of valid points (relevant only for ρ_{eq}) is plotted as green bars.

Figure 4.2 shows that a D_{st} decrease is, on average and with little variation, preceded by a large drop in B_z . The other variables may have some trend, but appear to change on the time scale of days rather than hours. For this reason, the same analysis was done after binning all data to a daily time scale, and the results are shown in Figure 4.3.

This shows the same decrease of B_z accompanying a decrease in D_{st} , but also more clearly shows that the solar wind velocity and ρ_{eq} both also differ significantly from the day before onset to onset (in the case of velocity) and the day of onset to the day after (in the case of density).

In an effort to replicate the results of Takahashi et al. [2010], shown in Figure 4.4, the same epoch analysis was done on a daily timescale for just the years looked at in the paper (1989-1991), and a similar plot was created. This is shown in Figure 4.5, and finds results that are fairly similar, with slight differences possibly attributable to difference in data pruning. Takahashi et al. [2010] only looks at events happening between 0600 and 1200 MLT since their f_{T3} detection rate was highest then, whereas this looks at all times. They

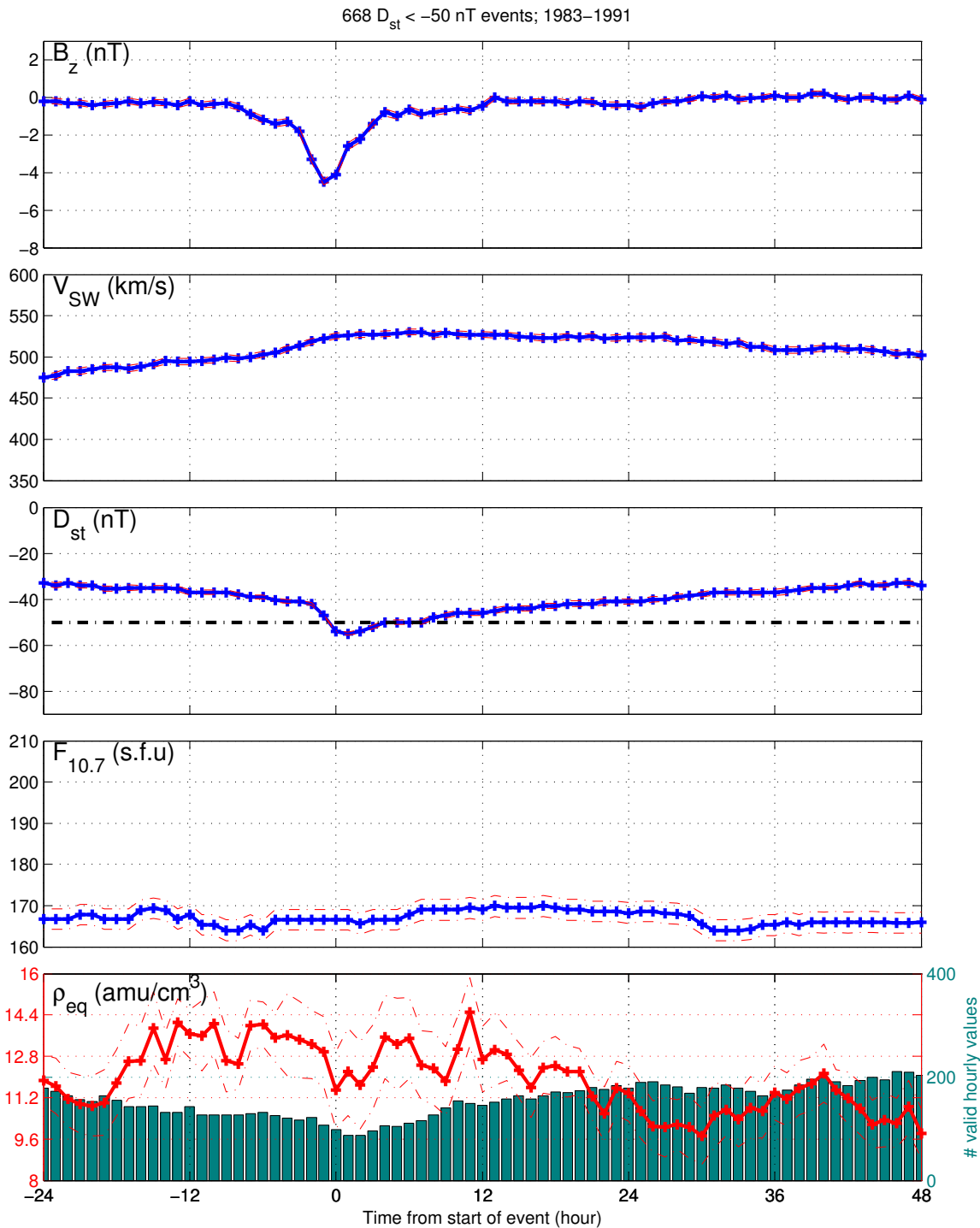


Figure 4.2: Epoch analysis for D_{st} events on an hourly timescale.

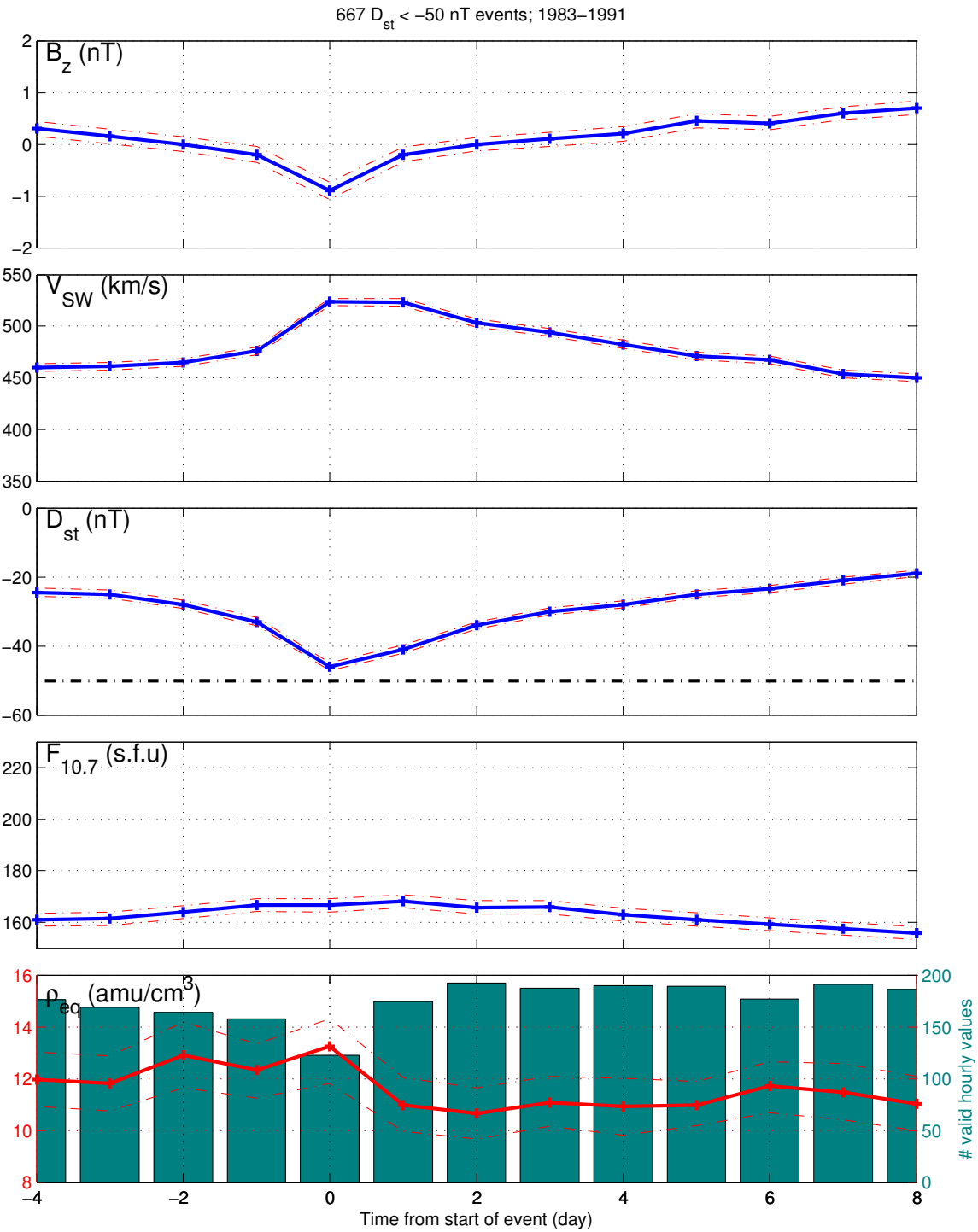


Figure 4.3: Epoch analysis for D_{st} events on a daily timescale.

also define "onset" as time corresponding to the minimum value in an event where D_{st} crossed the -50 nT threshold, whereas this considers the moment of crossing the threshold to be the onset.

To verify that there was in fact a significant difference between the day of onset and the day to either side, a bootstrap significance test was performed where a number of samples equal to the number of events was selected at random with replacement, and the median values were calculated. This was done 1000 times, and a histogram was created showing the distribution of differences between median values, shown in Figure 4.6

The idea here is that if the days have equal medians, a large number of random samples for each day should be equal on average. If the medians of two days are equal, the difference between those medians should be zero, so if a significant portion of differences have a skewed non-zero value, this suggests the days are not equal. Figure 4.6 therefore shows that only when looking at the difference in median ρ_{eq} between the day of onset and the day following can you get a distribution where less than 5% of the random samples lie beyond the hypothesized difference of 0, while the other two tests fail to reject the hypothesis of equal median daily values.

A few other forms of epoch analysis were done for exploratory purposes. Figure 4.7 shows D_{st} events where D_{st} remained below the -50 nT threshold for at least 12 hours. The same preceding drop in B_z can be seen, but now also appears to sustain the more negative value for longer. Also of note is the large spike in ρ_{eq} , but it comes at a point with few available data points, and the uncertainty on each point is large, making it difficult to say anything conclusive about the behavior of density during sustained periods of highly negative D_{st} .

Looking at events defined as a period where ρ_{eq} crosses a threshold of 20 amu/cm³ shows, in Figure 4.8, that there are no apparent trends in the solar wind or solar variables coinciding with the increase in density.

And finally, to test the amount of natural variance and for the sake of verification, a stack plot was made with random times selected as event onsets for both hourly and daily

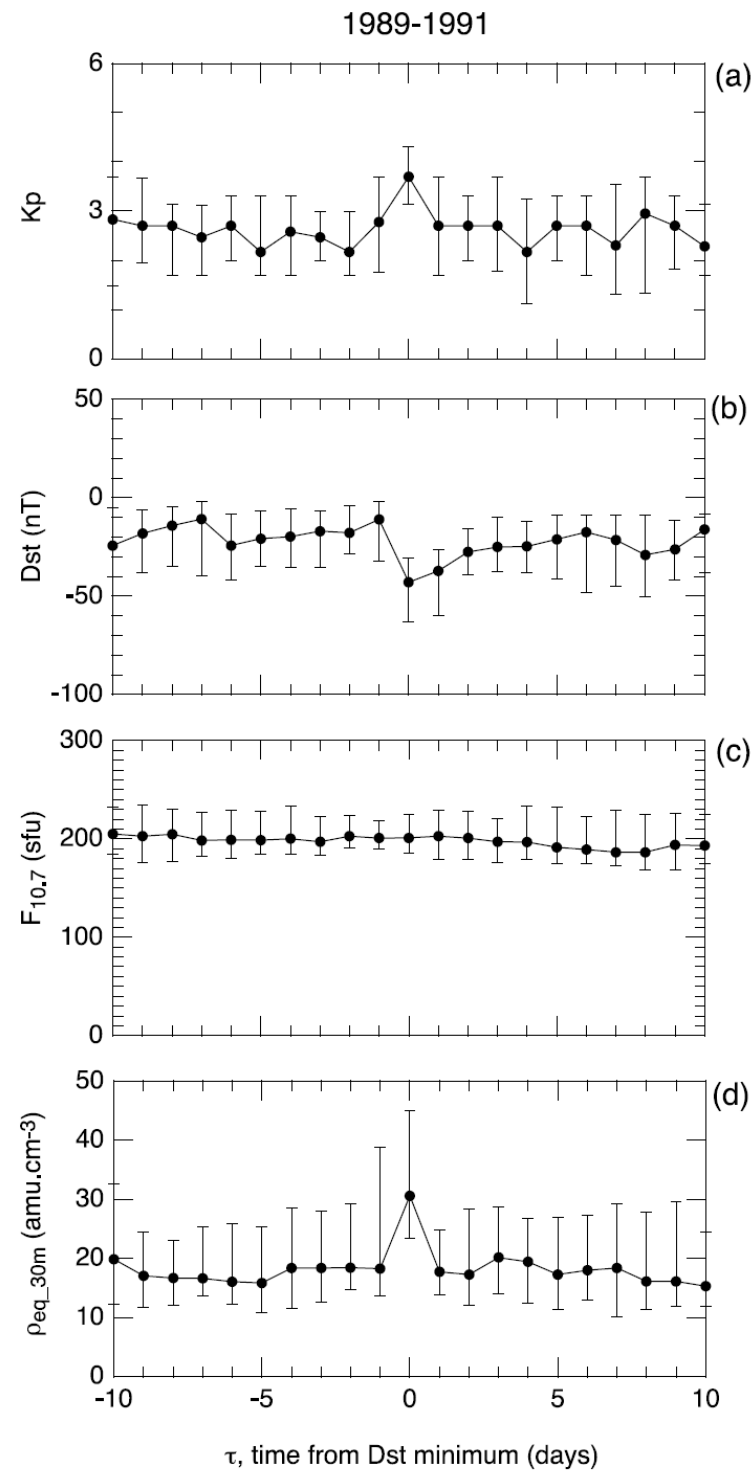


Figure 4.4: Epoch analysis for D_{st} events on an daily timescale using only the years of 1989-1991 from [Takahashi et al., 2010].

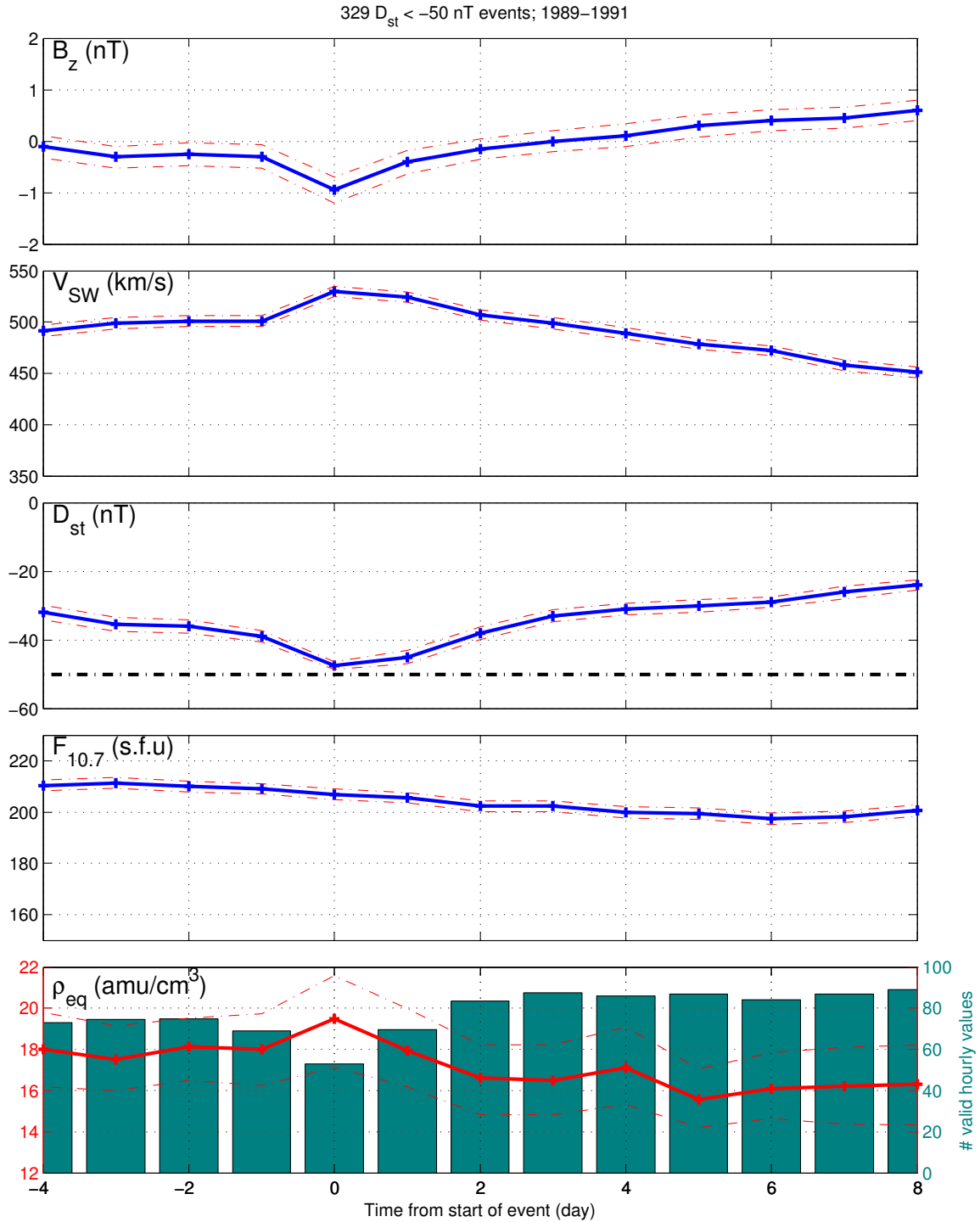


Figure 4.5: Epoch analysis for D_{st} events on an daily timescale using only the years of 1989-1991.

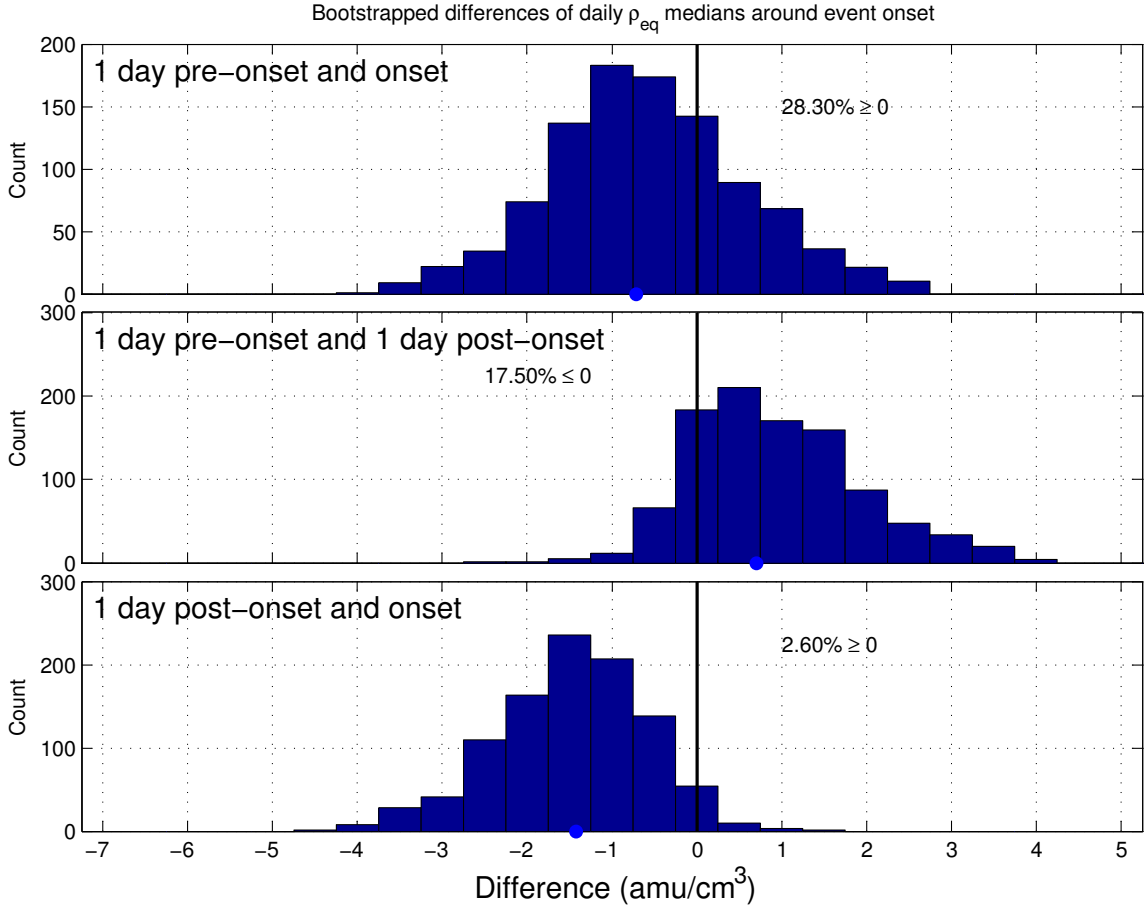


Figure 4.6: Bootstrap differences between median daily value of events using only the years of 1989-1991.

data. Figures 4.9 and 4.10 show both examples, and that neither have any significant trends.

4.6 $F_{10.7}$ Dependence

Takahashi et al. [2010] showed a strong correlation between the 27-day averaged $F_{10.7}$ index of solar activity and the averaged equatorial mass density (ρ_{eq}). This was chosen as a starting place for verifying the data analysis routines developed for this dataset, so as to show that data input, averaging, and interpolation were all done in a reasonable and reproducible manner. Figure 4.11.a shows the strong correlation seen previously, and reasonably reproduces Figure 13.b from Takahashi et al. [2010] for the years covered by GOES

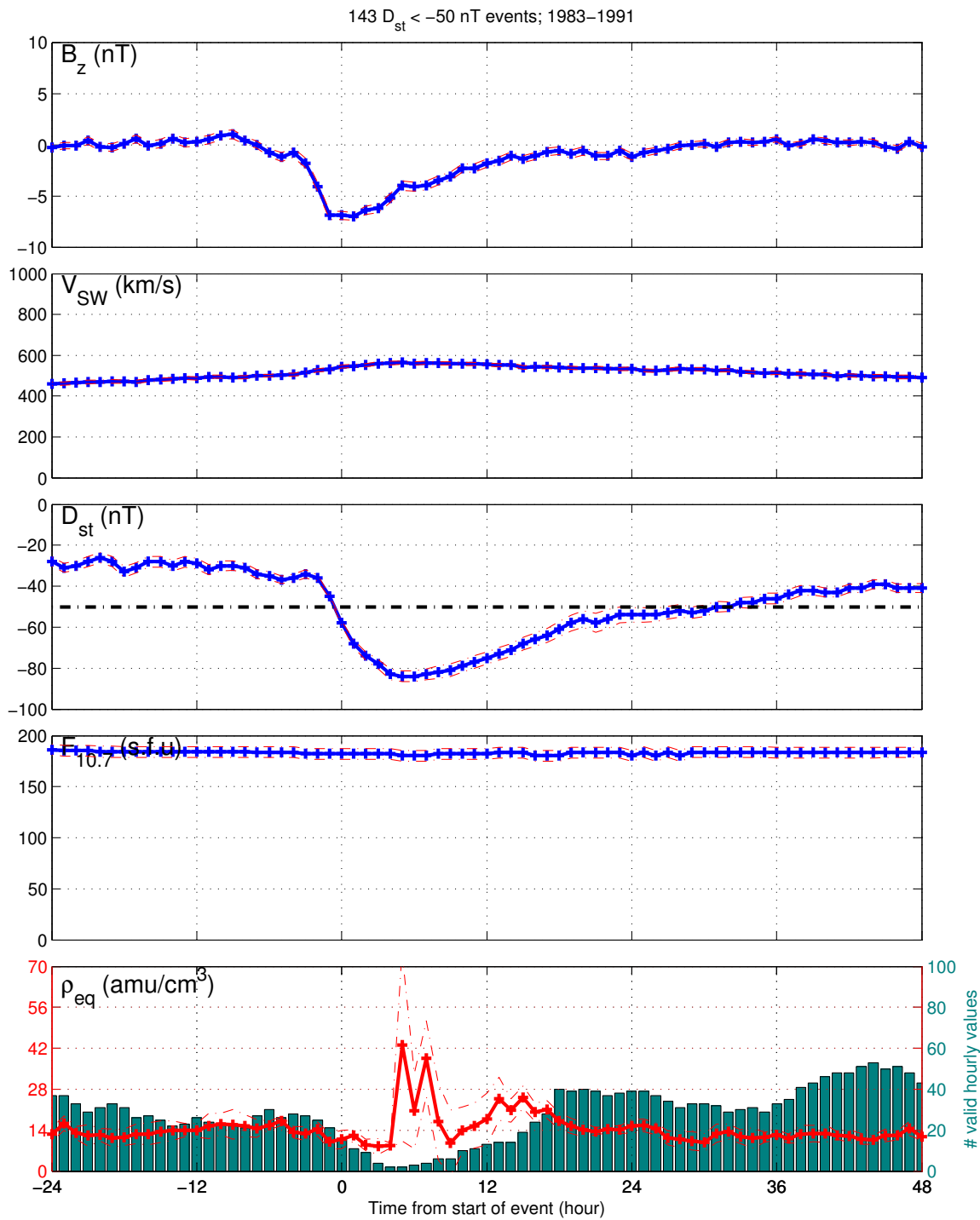


Figure 4.7: Epoch analysis for D_{st} events lasting longer than 12 hours.

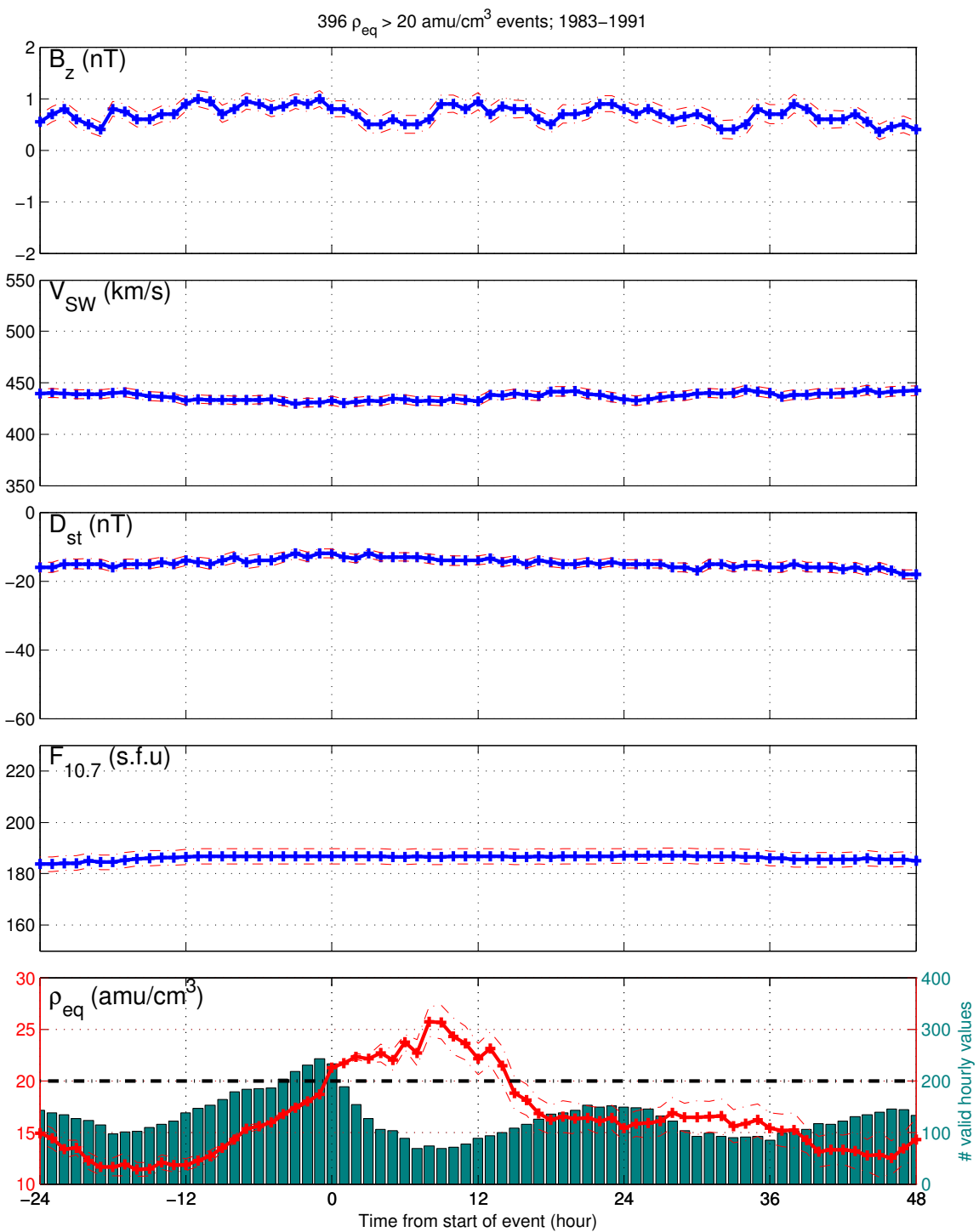


Figure 4.8: Epoch analysis for ρ_{eq} events on an daily timescale.

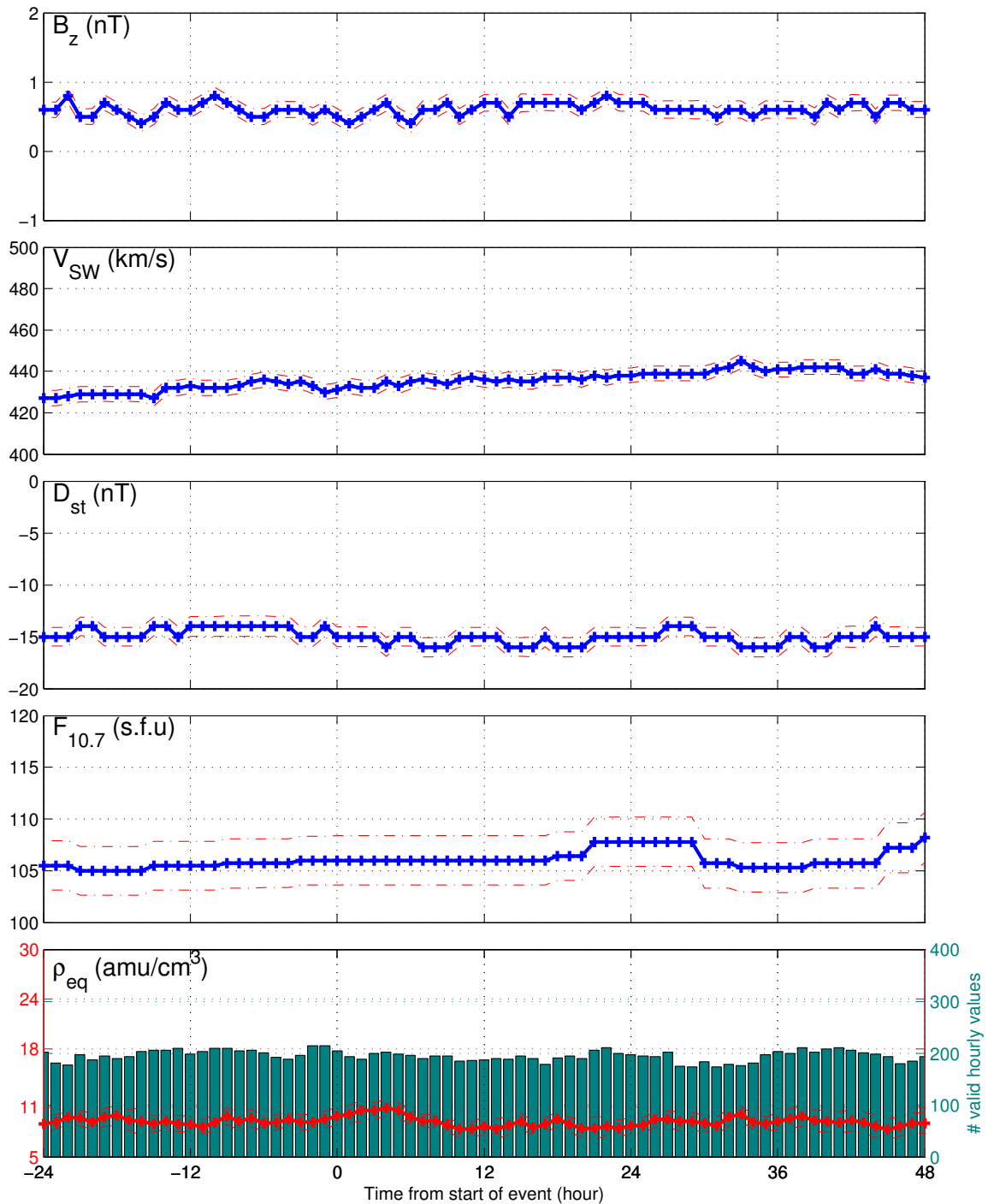


Figure 4.9: Epoch analysis for randomly selected events on an hourly timescale.

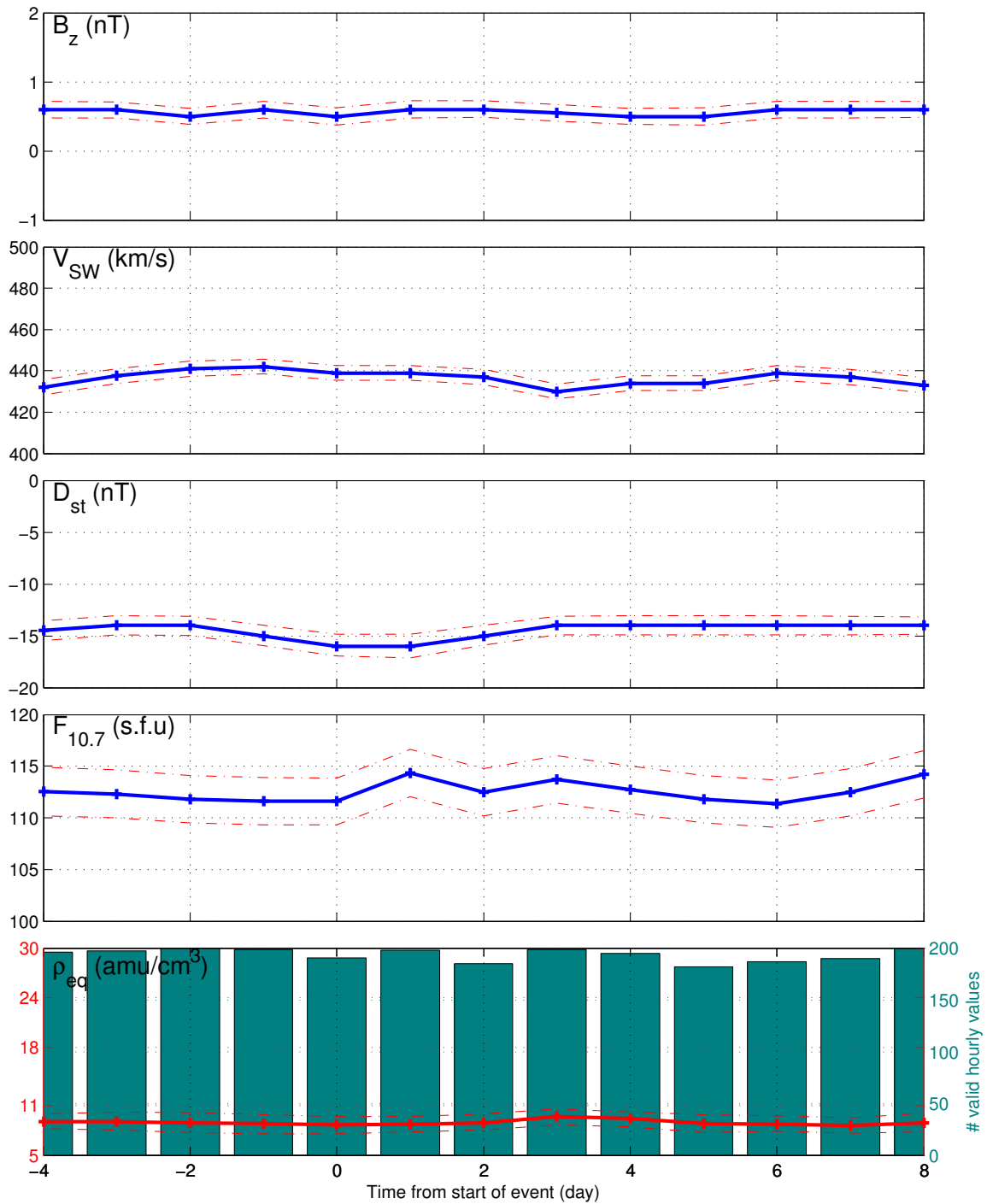


Figure 4.10: Epoch analysis for randomly selected events on a daily timescale.

6. Figure 4.12 shows the effects of long-time-scale averaging on the overall correlation of the two variables, suggesting that the connection is more influential long-term.

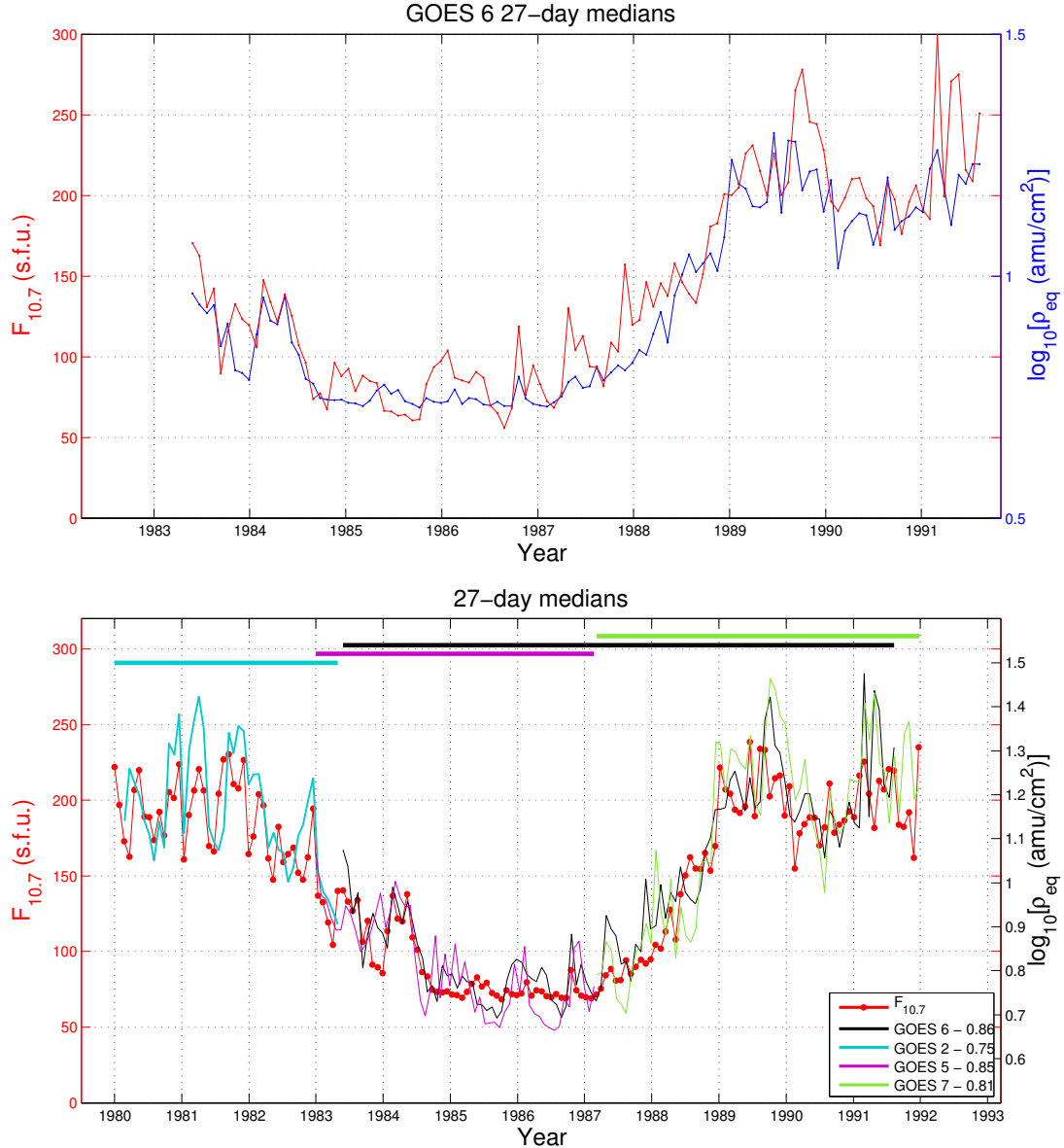


Figure 4.11: Top: Comparing $F_{10.7,27d}$ and $\log(\rho_{eq,27d})$ using GOES 6 data. Bottom: Same as top, but all available satellites.

The dependence was then analyzed in a more nonlinear manner by investigating the

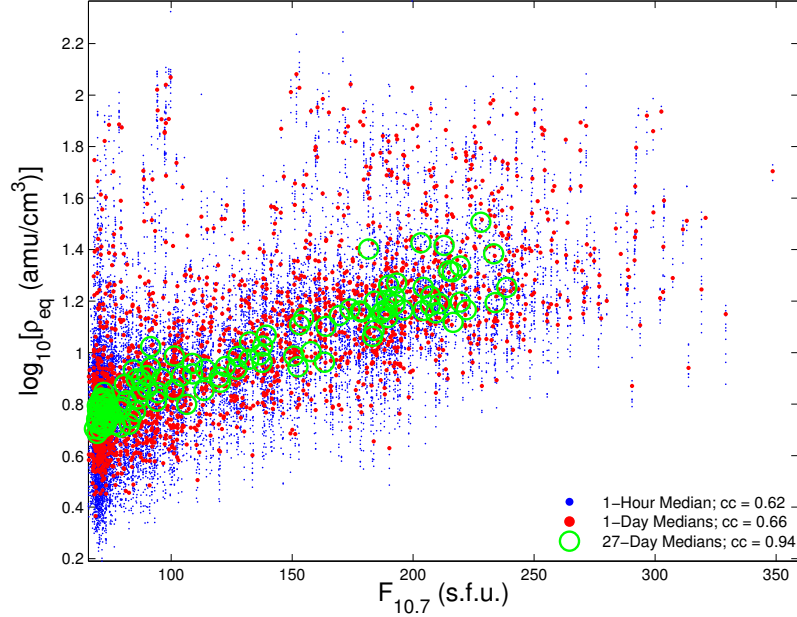


Figure 4.12: $F_{10.7}$ and $\log(\rho_{eq})$ correlation at varying time scales.

behavior of storms under different $F_{10.7}$ conditions. The hypothesis being that solar activity would drive both geomagnetic storms and, consequently, ρ_{eq} . By separating storms into bins based on the median value of $F_{10.7}$, then breaking those two bins into another two bins each separated by their respective medians, a profile of all storm behavior based on $F_{10.7}$ is obtained. Figure 4.13 shows the results of this across the events where D_{st} crossed below the -50 nT threshold.

The top panel of Figure 4.13 shows that ρ_{eq} reacts to decreases in D_{st} , but seemingly only during periods of higher solar activity. Since higher $F_{10.7}$ also correlates with a higher baseline ρ_{eq} , this effect could be due to saturation of the plasmasphere from the increased solar activity. It should also be noted that this trend isn't seen as strongly for all satellites. GOES 2 and 6 show a significant spike and baseline shift, while GOES 7 and 5 lack the significant spike and shift respectively.

The bottom panel of Figure 4.13 shows that though all events are selected based on a D_{st} threshold, the behavior before and after the storm is affected by $F_{10.7}$. For low solar activity events, the D_{st} changes are more sudden and severe, coming from and going back

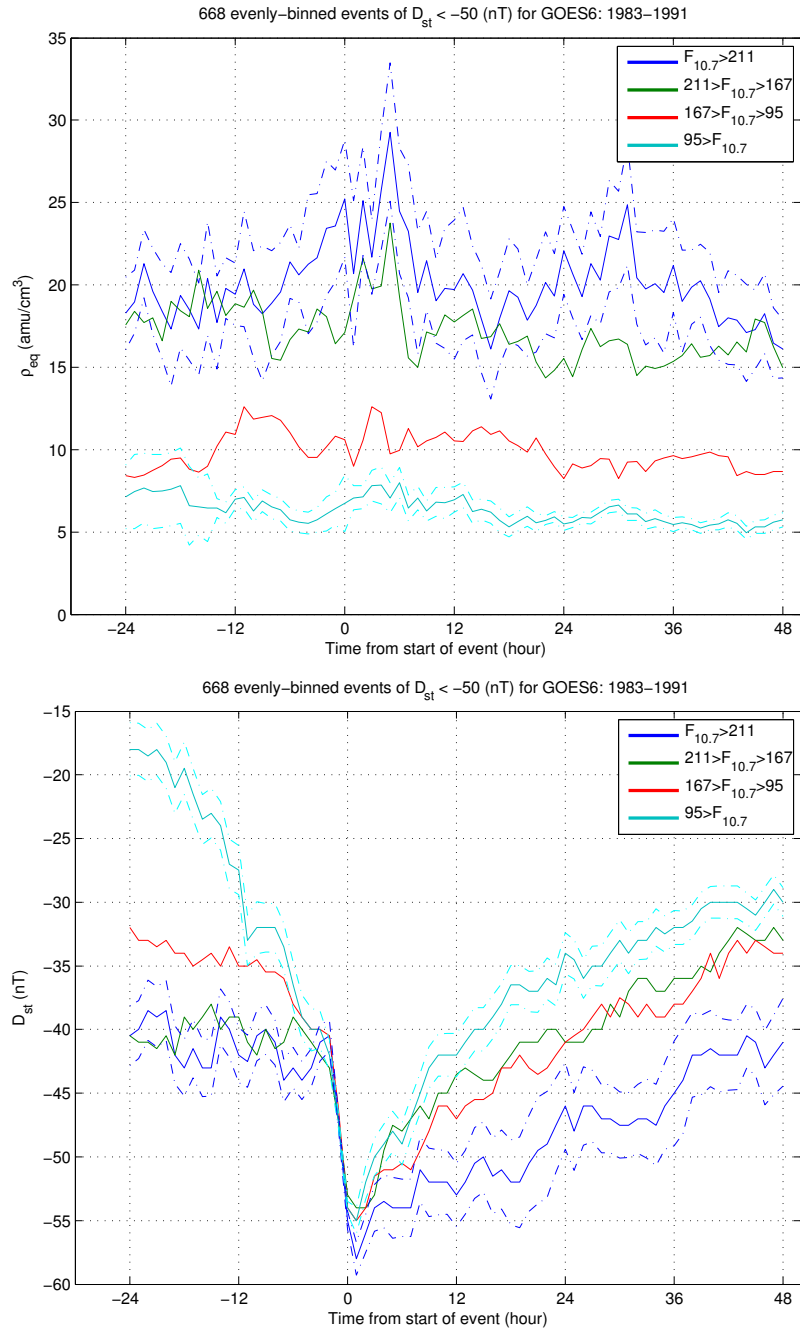


Figure 4.13: ρ_{eq} (top panel) and D_{st} (bottom panel) of D_{st} events binned by median $F_{10.7}$ values.

to a more positive baseline. High solar activity events have a longer recovery period.

One other method of testing dependence was done, where events were binned by the median value of the four hour leading up to event onset, and by the four hours at and following onset. Then the general trend of these two types of events is analyzed and a Wilcoxon rank-sum test (via `ranksum` [MATLAB, 2014]) is done at each hour to determine if the distributions of the two bins could come from the same population. Figure 4.14 shows that events are significant at a majority of the hours tested, with higher values of $F_{10.7}$ leading to higher values of ρ_{eq} both before and after event onset. This is consistent with the results of Denton et al. [2016] where daily averaged values of ρ_{eq} are different for high and low values of $F_{10.7}$.

If we instead define events as when D_{st} crosses the threshold of $-50nT$, we find even more obvious distinction in ρ_{eq} binned by $F_{10.7}$ as shown in Figure 4.15. This not only supports the idea of a significant dependence in ρ_{eq} behavior on $F_{10.7}$, but also demonstrates other facets of the structure shown in Figure 4.13 such as the peak in density just after onset for high values of $F_{10.7}$.

4.7 B_z Dependence

Similar to the $F_{10.7}$ dependence, tests were done to see if event behavior varied with the z -component of the interplanetary magnetic field (IMF). It's well established that the orientation of B_z has a strong correlation with the strength of geomagnetic storms [Takahashi et al., 2010], so events were found based on a threshold of $\rho_{eq} \geq 20 \text{ amu/cm}^3$. These events were then binned by both the median B_z at and four hours after threshold crossing, and B_z at and four hours before threshold crossing. Figure 4.16 shows both cases.

For each binning method, a two sample t-test was performed for each hour to determine if the samples in each bin had significantly different medians from those of the other bin. As there are 73 hours to perform a t-test on, a 95% confidence interval could be expected

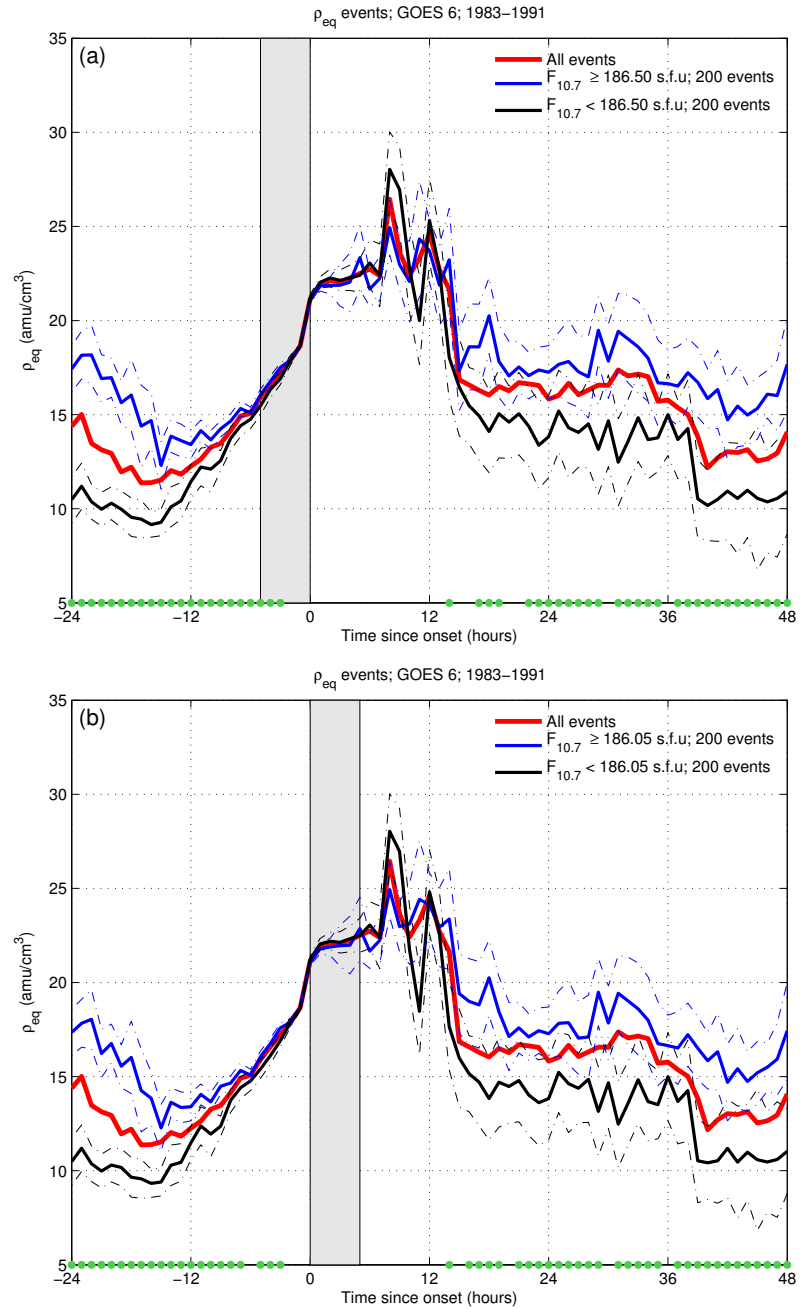


Figure 4.14: ρ_{eq} events binned by median $F_{10.7}$ before (top panel) and after (bottom panel) event onset.

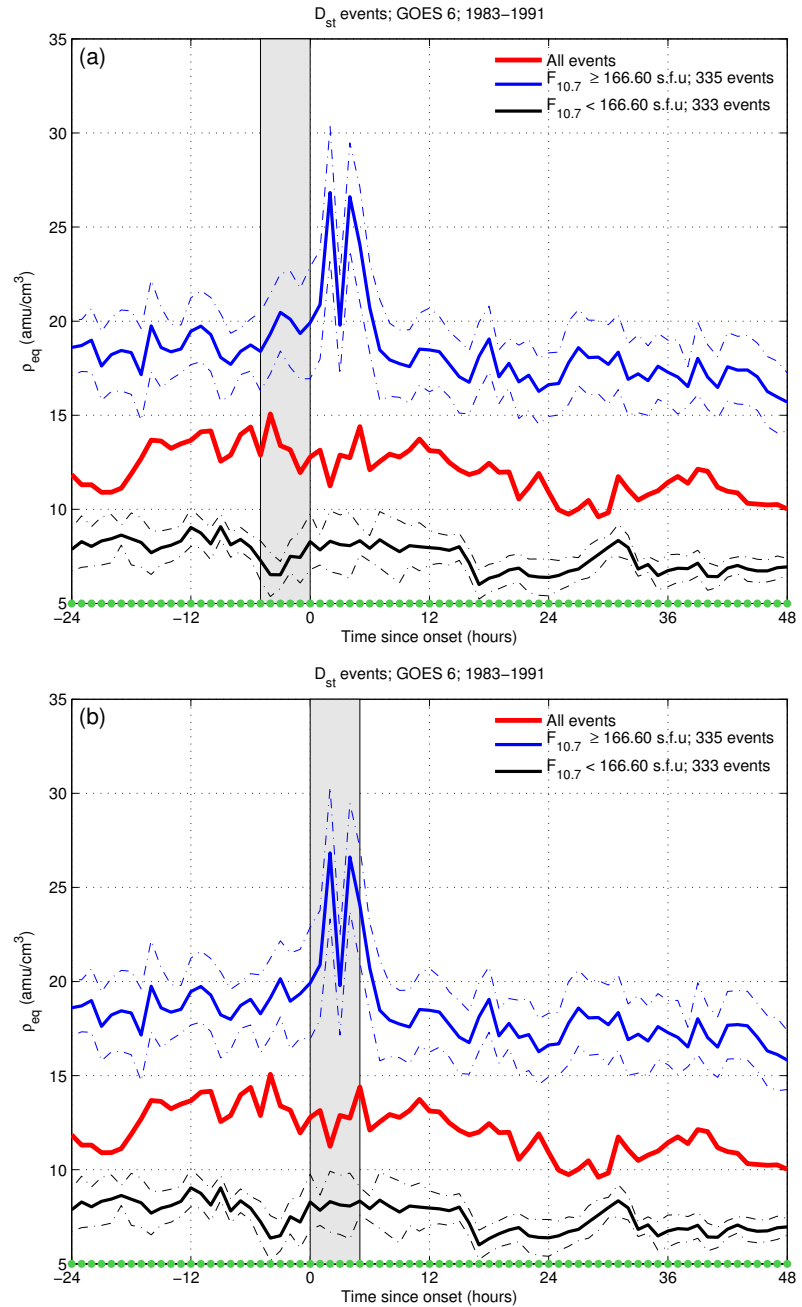


Figure 4.15: D_{st} events binned by median $F_{10.7}$ before (top panel) and after (bottom panel) event onset.

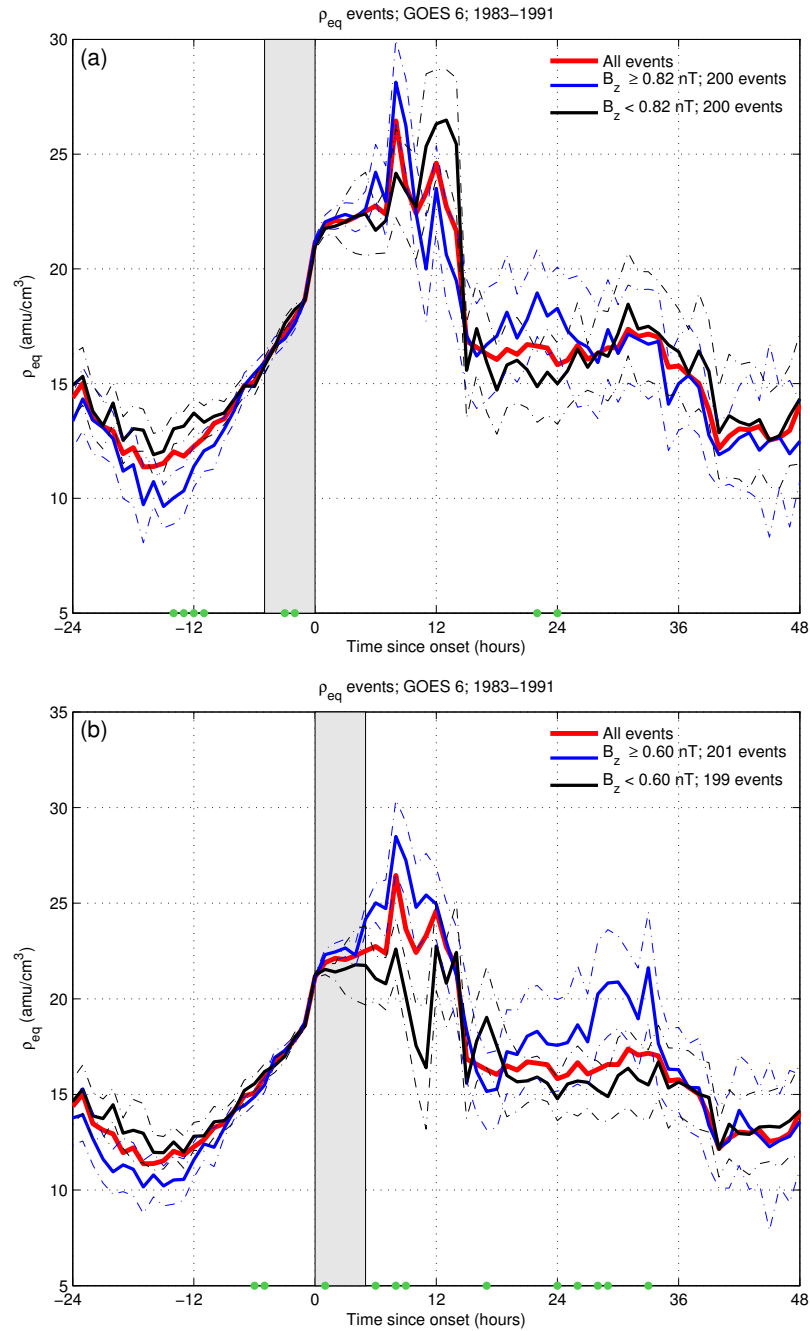


Figure 4.16: ρ_{eq} events binned by median B_z before (top panel) and after (bottom panel) event onset.

to have at least four randomly significant results. Because of this, the six significant t-test result for events binned by pre-onset B_z can only barely confirm that such a division shows significantly different behaviors, whereas the nine significant test results for post-onset B_z , six of which are consecutive hours, can be said to show a more significant division in behavior between the bins. This physically suggests that the further into a ρ_{eq} increase you get, the more B_z orientation impacts the long-term recovery to normal conditions (and indeed moving the window further in time did continue to show significance, but weakly and with no obvious trend). If instead of splitting into equal-number bins, the division is based on positive or negative B_z , either time window produces seven or more significant results, but with the added complication that one bin has twice as many samples as the other and may be biased by averaging or the lack thereof.

Temerin and Li [2002] discuss the impact of B_z on their model of D_{st} showing a seasonal variation of D_{st} . Figure 4.17 shows how D_{st} seems to vary with day of year (DoY) in our nonlinear models. These plots show a nonlinear model trained on all data, then predicted over a uniform grid of points to visualize the underlying structure of the model. The top panel predicts D_{st} using DoY as an input, showing the average model output over 40 ensemble models, along with the standard deviation at each point. The bottom panel predicts D_{st} using both DoY and B_z as inputs, also using a 40-member ensemble average, but with the actual datapoints overlaid to give an idea of what the structure may be derived from. Marker size in this panel is based on the value of D_{st} at that point. It seems to support the idea of a seasonal variation, and weakly the idea that B_z also plays a part in that relationship.

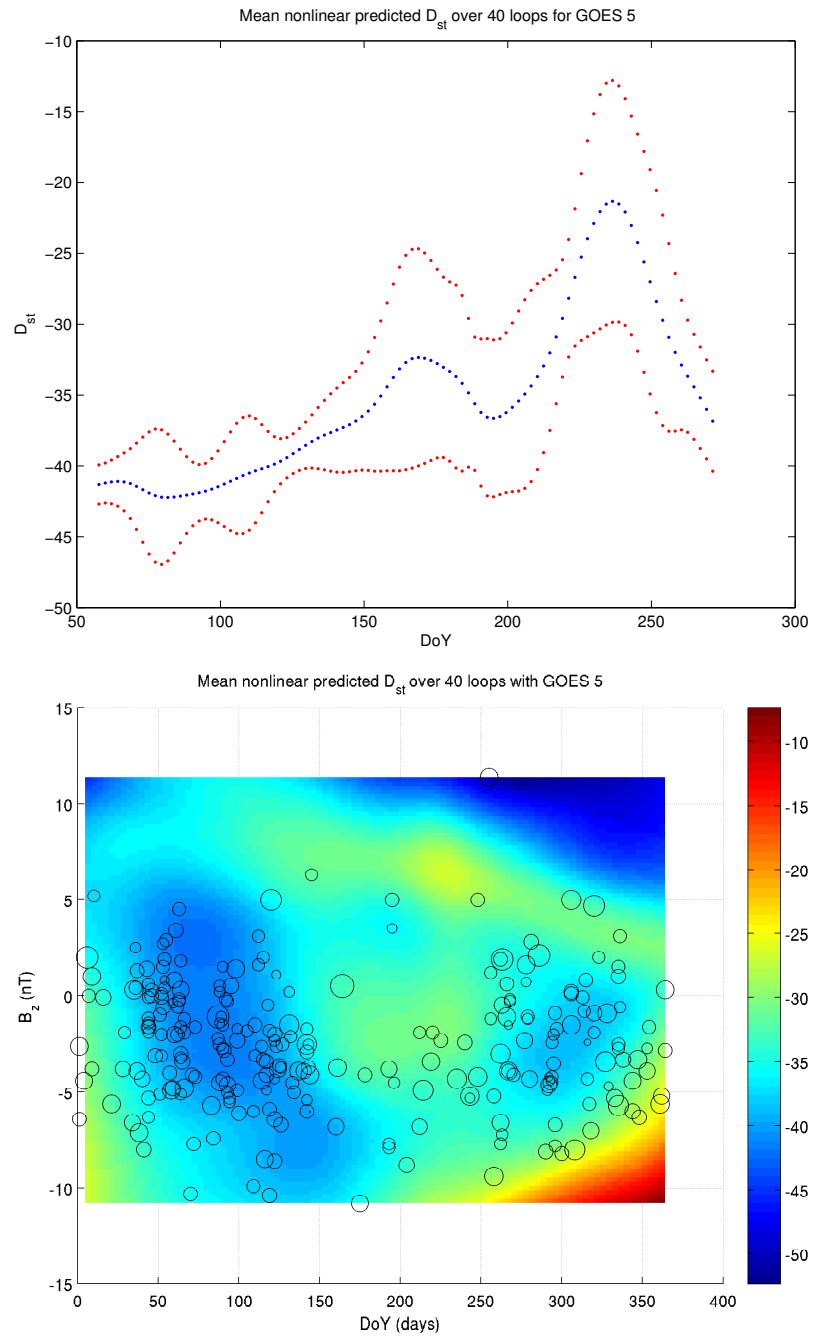


Figure 4.17: Top: D_{st} predicted by nonlinear model of day of year. Bottom: Same, but including a dimension for B_z .

Chapter 5: Onset Classification

5.1 Method

Since forecasting actual values for ρ_{eq} isn't always viable or accurate, an attempt was made to model ρ_{eq} event onsets as a classification problem whereby an onset timestep (the one in which the 20 amu/cm^3 threshold was crossed) was defined as a "1", and any other time defined as a "0". Denton et al. [2016], which also uses the inferred ρ_{eq} from GOES Alfvén waves, indicates that daily averaged Kp and $F_{10.7}$ both are involved in driving the behavior of ρ_{eq} . By then passing relevant measurements such as Kp, $F_{10.7}$, and V_{SW} into a non-linear classification model such as `patternnet` [MATLAB, 2014], a predictive classification could be made based on these conditions.

Two formats and two time scales were tested: one format consisting of passing in an entire timeseries, where each prediction was based on a sliding window of the current and previous three timesteps as one set of inputs. The other format only considered time periods at and three hours before onset, but treated each time step as its own input and classification. Both formats are diagrammed in Figure 5.1. The top diagram shows the classification method where the modeling window slides across one timestep at a time and only spans four timesteps at each onset. The bottom diagram depicts the prediction method where the window slides across all data, and each block of four timesteps attempts to predict an onset one step ahead. Both methods were used to make models for the two time scales of hourly and daily medians of values.

In order to aid the model in finding event onsets despite being numerically overwhelmed by non-onsets, the targets are weighted to more highly value a "1". Since the number of events is similar between hourly and daily timescales, but the number of data points is a factor of 24 larger for the hourly scale. As such, the weights are scaled so targets have a

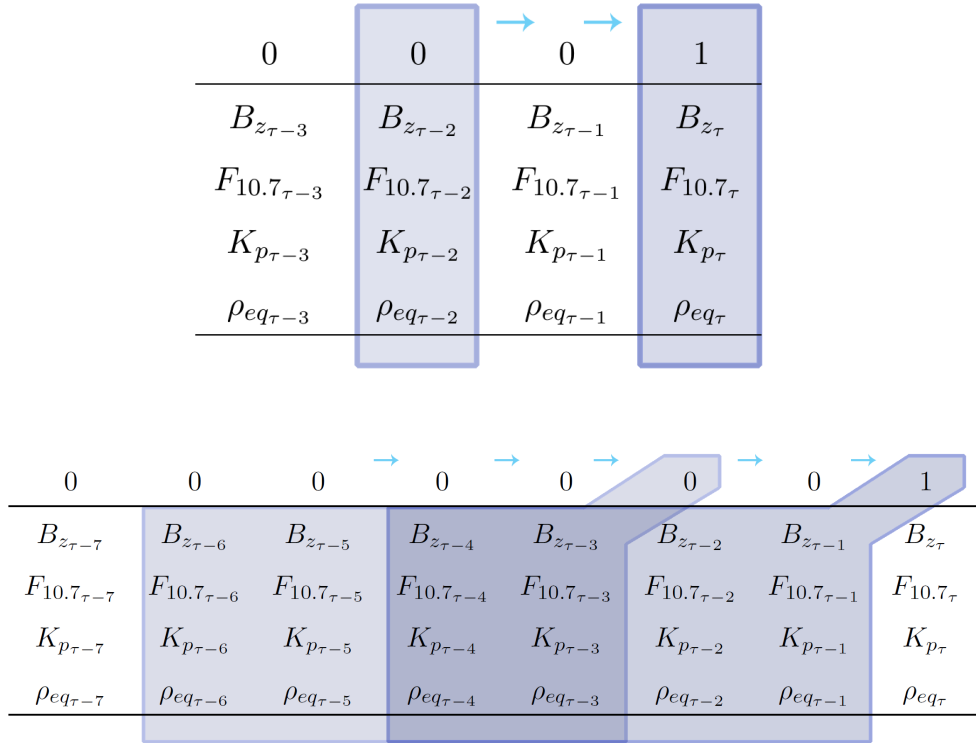


Figure 5.1: Diagram of classification (top) and prediction (bottom) methods.

value of the logarithm of the number of data points divided by the number of onsets, while all other points have a weight of 1. This gives a typical relative weight of 2-7 for onsets vs non-onsets.

5.2 Results

5.2.1 Classification

Figure 5.2 is a confusion matrix, where onsets (class "1") and non-onsets (class "0") are categorized based on their real value labeled "Target Class", and the value categorized by the model labeled "Output Class". So for example, on a daily timescale, there were 582 event onsets (sum of Target class 1), and the model correctly classified 473 of them (intersection of target class 1 and output class 1). Since this classification model is primarily concerned with

correctly classifying onsets, the percentage values given will be for the percent of correctly classified onsets out of the total number of onsets, shown as the green value in the bottom of column 2. This specific figure shows that trying to classify events on an hourly timescale using only the onset hour and three hours before leads to a model that classifies almost no onsets. Using daily values, however, results in a model where a full 80% of the onsets are correctly detected and classified, but only half of the predicted onsets were actually onsets.

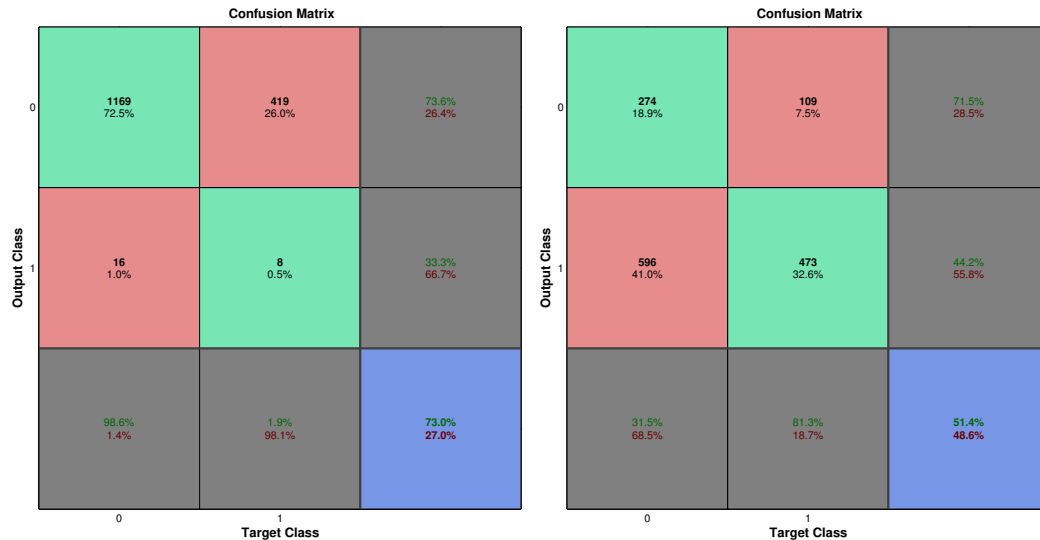


Figure 5.2: Prediction confusion matrix for hourly (left) and daily (right) ρ_{eq} onset events using classification method

In an attempt to find out what conditions best lead to a correct classification, histograms were made of the conditions associated with a correctly classified onset vs those of an undetected onset. Figure 5.3 shows this for the four variables used.

It shows that the model tended to miss onsets during periods of particularly low $F_{10.7}$, and during high speed solar winds, but was largely unaffected otherwise.

The next test was to add more obvious indicators of an event onset, such as the data being used to define an onset, and see if the model could pick that up. By adding ρ_{eq} as a factor in classifying ρ_{eq} events, the model unsurprisingly does very well, as shown in Figure 5.4.

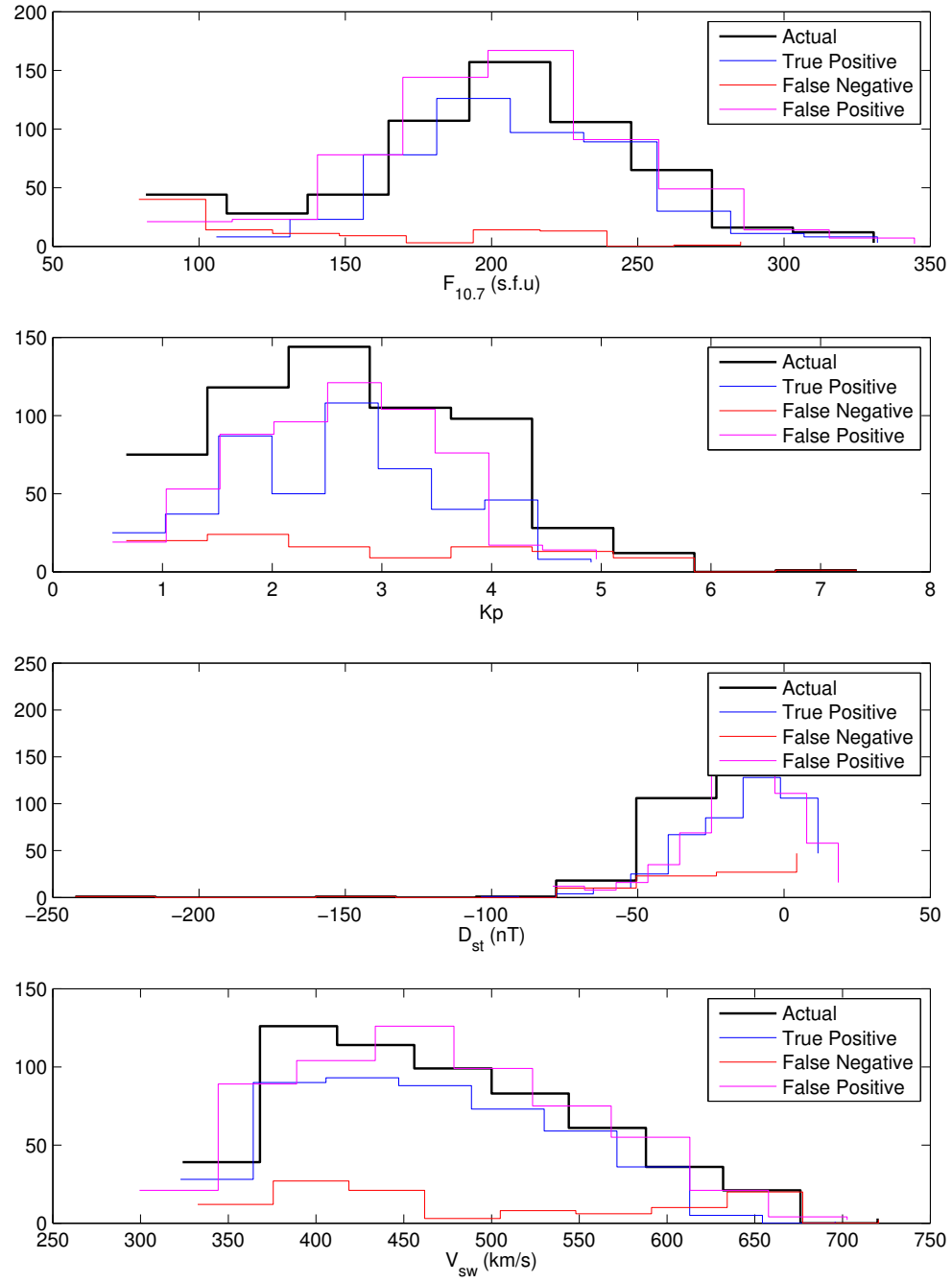


Figure 5.3: Histogram of onset conditions for daily-averaged ρ_{eq} events binned by correctness of prediction



Figure 5.4: Prediction confusion matrix for hourly (left) and daily (right) ρ_{eq} onset events, including ρ_{eq} as an input variable, and only looking at three hours before and including onset

With a successful true positive classification rate of 99% and 84% for hourly and daily 4-hour models respectively, it can be said that including ρ_{eq} information makes the models effective for classifying event onset, both validating the model as being able to determine our selection criteria as well as showing the extent to which daily averaging can obscure conditions attributed to an event. Since the ρ_{eq} events have a median duration of 14 hours above the -20 nT threshold, it's clear that they significantly impact the entire day enough to still be detectable. A histogram of these variables binned by true positive and false negative shows no particularly compelling trends, as seen in Figure 5.5.

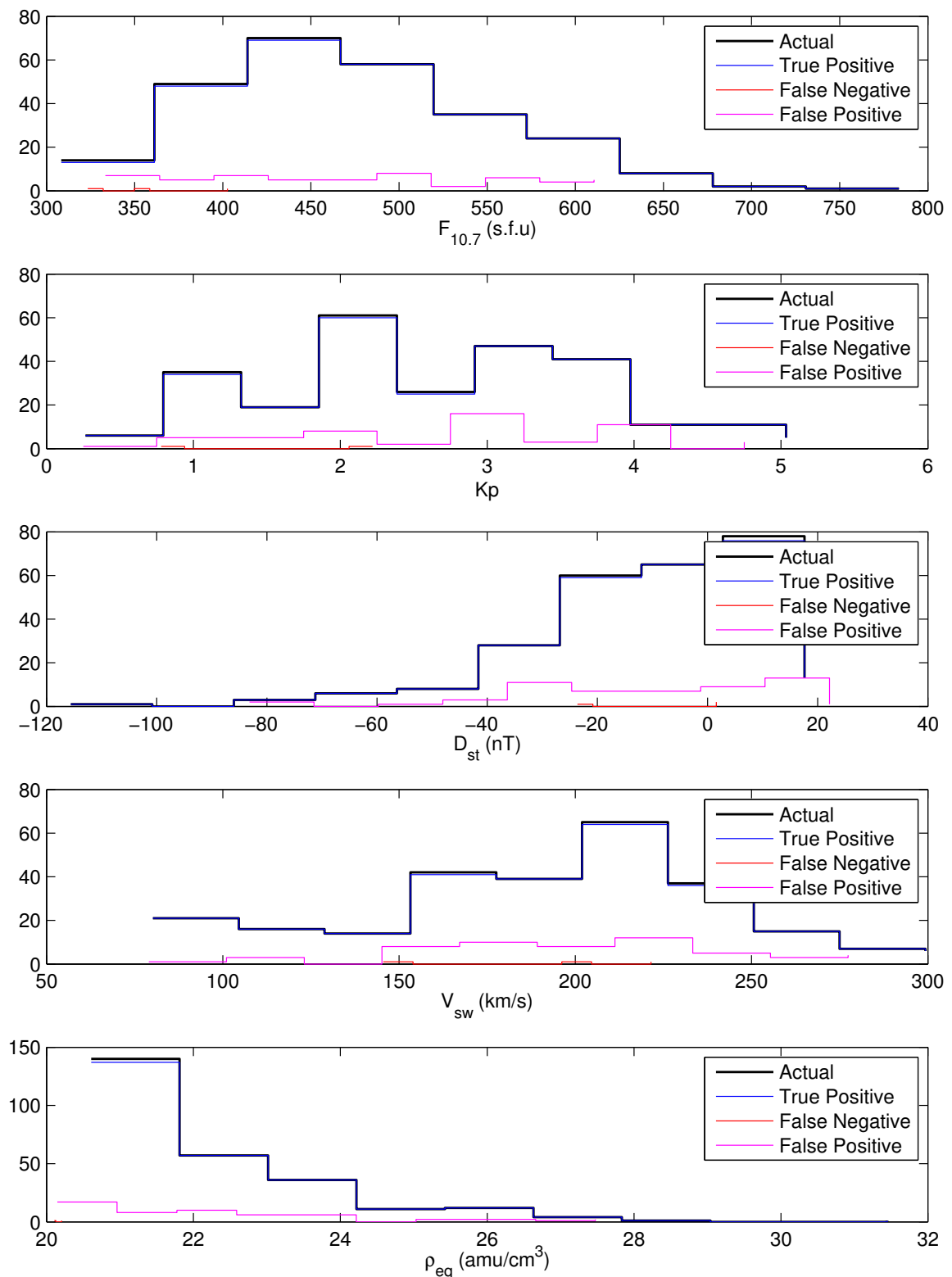


Figure 5.5: Histogram of onset conditions for hourly ρ_{eq} events including ρ_{eq} as an input, binned by correctness of prediction

5.2.2 Forecasting

Using the full data set where each prediction was based on the previous four timesteps of inputs ($F_{10.7}$, K_p , D_{st} , and V_{SW}) returned two models (daily and hourly). Both were tested with and without ρ_{eq} included as an input variable due to its more limited availability. All four confusion matrices are shown in Figure 5.6.

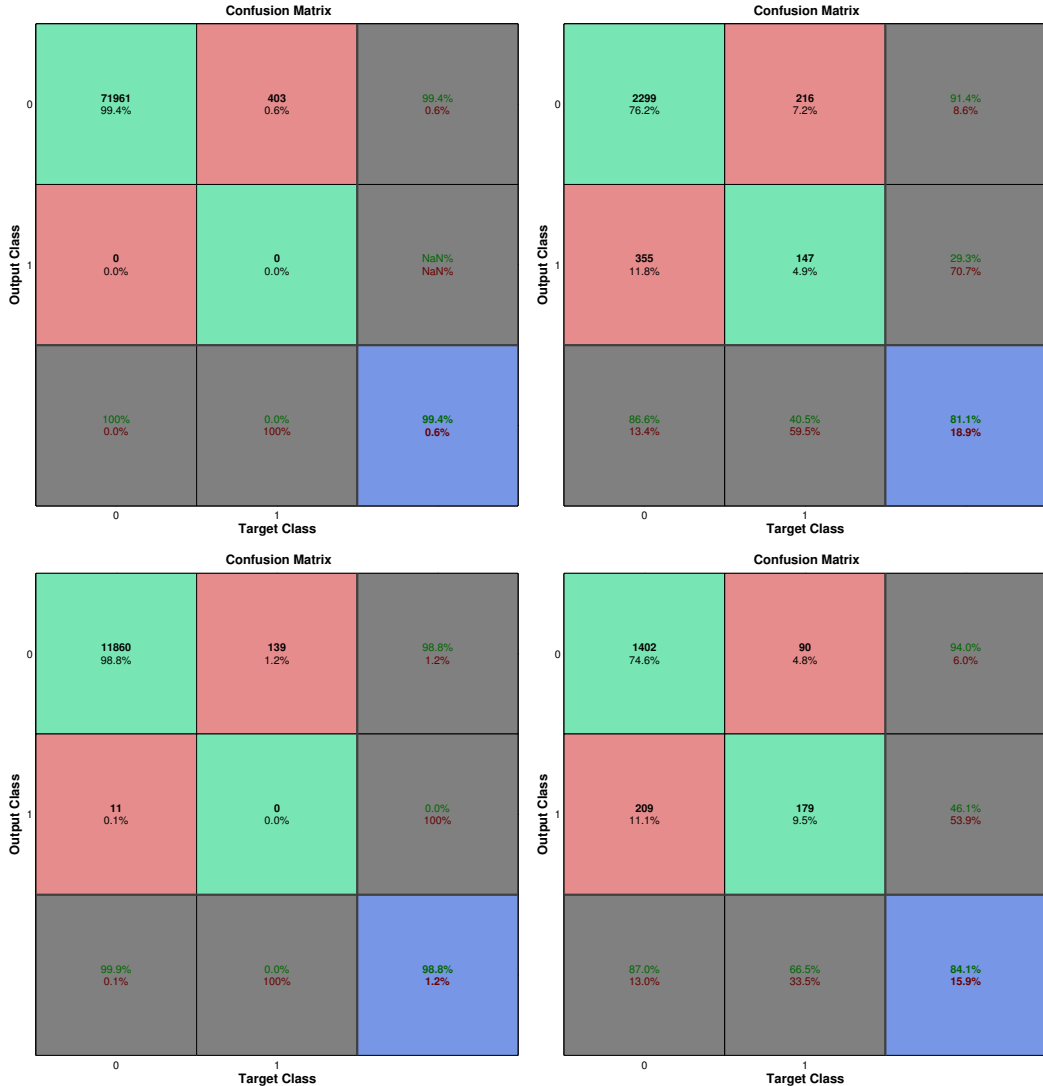


Figure 5.6: Prediction confusion matrix for hourly (left column) and daily (right column) ρ_{eq} onset events, including ρ_{eq} as an input in the bottom row, and using entire timeseries with a four hour sliding window

It's seen that the selected weighting scheme is not sufficient to pick up hourly events without further tuning, but is overly aggressive with the daily values and ends up creating more false positives than truly correct predictions. That said, being able to predict 66% of events a day in advance, at the cost of only half of the predicted onsets being accurate, is not completely useless. Again, the variables were broken down by value and correctness of prediction, this time taking the median value of each variable across the four-timestep bin. The resulting histograms are shown in Figure 5.7.

This model seems to also miss predictions during periods of low solar activity and low density. Considering at least one value had to be less than 20, and one greater than 20, this might indicate that certain events are starting lower in value and barely crossing the threshold, and end up with poor predictions for it. The model also shows that the false positives tend to follow the same distribution as the true onset values, suggesting that the model is picking up the structure but missing some other information that would determine whether ρ_{eq} actually sees a measured increase in value. As this is a first attempt at this sort of model, there is much room for refinement and improvement.

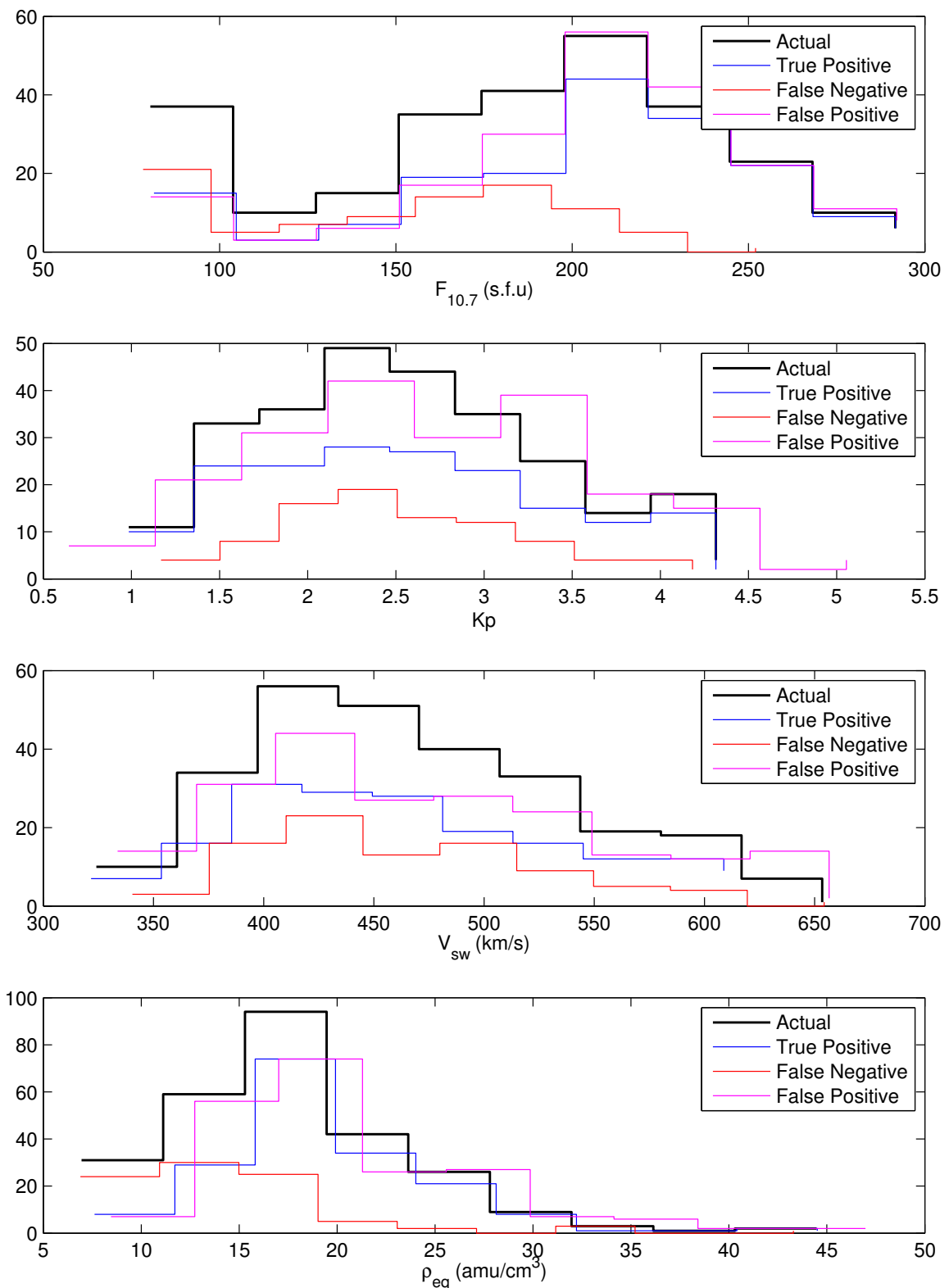


Figure 5.7: Histogram of onset conditions for daily ρ_{eq} events including ρ_{eq} as an input, binned by correctness of prediction

Appendix A: An Appendix

This is an appendix. Here is a numbered appendix equation:

$$a^2 + b^2 = c^2. \quad (\text{A.1})$$

Bibliography

- Access to GOES SEM data. URL <https://www.ngdc.noaa.gov/stp/satellite/goes/dataaccess.html>.
- J. Allen. Some Commonly Used Magnetic Activity Indices: Their Derivation, Meaning, and Use, 1982. URL <https://www.ngdc.noaa.gov/stp/solar/magindices.html>.
- J. Allen, L. Frank, H. Sauer, and P. Reiff. Effects of the March 1989 solar activity. *EOS Transactions*, 70:1479, November 1989. doi: 10.1029/89EO00409.
- R. Bala and P. Reiff. Improvements in short-term forecasting of geomagnetic activity. *Space Weather*, 10:S06001, June 2012. doi: 10.1029/2012SW000779.
- L. F. Bargatze, D. N. Baker, E. W. Hones, Jr., and R. L. McPherron. Magnetospheric impulse response for many levels of geomagnetic activity. *Journal of Geophysical Research*, 90:6387–6394, July 1985. doi: 10.1029/JA090iA07p06387.
- J. Birn, J. F. Drake, M. A. Shay, B. N. Rogers, R. E. Denton, M. Hesse, M. Kuznetsova, Z. W. Ma, A. Bhattacharjee, A. Otto, and P. L. Pritchett. Geospace environmental modeling (gem) magnetic reconnection challenge. *Journal of Geophysical Research: Space Physics*, 106(A3):3715–3719, 2001. ISSN 2156-2202. doi: 10.1029/1999JA900449. URL <http://dx.doi.org/10.1029/1999JA900449>.
- D. L. Carpenter. Whistler studies of the plasmapause in the magnetosphere: 1. Temporal variations in the position of the knee and some evidence on plasma motions near the knee. *J. Geophys. Res.*, 71:693–709, February 1966. doi: 10.1029/JZ071i003p00693.

- D. L. Carpenter and R. R. Anderson. An ISEE/Whistler model of equatorial electron density in the magnetosphere. *J. Geophys. Res.*, 97:1097–1108, February 1992. doi: 10.1029/91JA01548.
- D. L. Carpenter and J. Lemaire. Erosion and Recovery of the Plasmasphere in the Plasmapause Region. *Space Science Reviews*, 80:153–179, April 1997. doi: 10.1023/A:1004981919827.
- C. Carreau. Earth’s plasmasphere and the Van Allen belts, September 2013. URL <http://sci.esa.int/cluster/52831-earth-plasmasphere-and-the-van-allen-belts/>.
- R. C. Carrington. Description of a Singular Appearance seen in the Sun on September 1, 1859. *Monthly Notices of the Royal Astronomical Society*, 20:13–15, November 1859.
- CCMC. Community coordinated modeling center. URL <http://ccmc.gsfc.nasa.gov/>.
- S. Chapman and V. C. A. Ferraro. A new theory of magnetic storms. *Terrestrial Magnetism and Atmospheric Electricity (Journal of Geophysical Research)*, 36:77, 1931. doi: 10.1029/TE036i002p00077.
- C. R. Clauer, R. L. McPherron, C. Searls, and M. G. Kivelson. Solar wind control of auroral zone geomagnetic activity. *Geophysical Research Letters*, 8:915–918, August 1981. doi: 10.1029/GL008i008p00915.
- F. Darrouzet, V. Pierrard, S. Benck, G. Lointier, J. Cabrera, K. Borremans, N. Y. Ganushkina, and J. D. Keyser. Links between the plasmapause and the radiation belt boundaries as observed by the instruments CIS, RAPID, and WHISPER onboard Cluster. *Journal of Geophysical Research (Space Physics)*, 118:4176–4188, July 2013. doi: 10.1002/jgra.50239.
- T. N. Davis and M. Sugiura. Auroral electrojet activity index AE and its universal time variations. *J. Geophys. Res.*, 71:785–801, February 1966. doi: 10.1029/JZ071i003p00785.

M. H. Denton and J. E. Borovsky. Observations and modeling of magnetic flux tube refilling of the plasmasphere at geosynchronous orbit. *Journal of Geophysical Research: Space Physics*, 119(11):9246–9255, 2014. ISSN 2169-9402. doi: 10.1002/2014JA020491. URL <http://dx.doi.org/10.1002/2014JA020491>. 2014JA020491.

R. E. Denton, K. Takahashi, I. A. Galkin, P. A. Nsumei, X. Huang, B. W. Reinisch, R. R. Anderson, M. K. Sleeper, and W. J. Hughes. Distribution of density along magnetospheric field lines. *Journal of Geophysical Research (Space Physics)*, 111:A04213, April 2006. doi: 10.1029/2005JA011414.

R. E. Denton, K. Takahashi, J. Lee, C. K. Zeitler, N. T. Wimer, L. E. Litscher, H. J. Singer, and K. Min. Field line distribution of mass density at geostationary orbit. *Journal of Geophysical Research (Space Physics)*, 120:4409–4422, June 2015. doi: 10.1002/2014JA020810.

R. E. Denton, K. Takahashi, J. Amoh, and H. J. Singer. Mass density at geostationary orbit and apparent mass refilling. *Journal of Geophysical Research (Space Physics)*, 121: 2962–2975, April 2016. doi: 10.1002/2015JA022167.

R. C. Elphic, L. A. Weiss, M. F. Thomsen, D. J. McComas, and M. B. Moldwin. Evolution of plasmaspheric ions at geosynchronous orbit during times of high geomagnetic activity. *Geophysical Research Letters*, 23:2189–2192, 1996. doi: 10.1029/96GL02085.

S. F. Fung, X. Shao, and L. C. Tan. Long-term variations of the electron slot region and global radiation belt structure. *Geophys. Res. Lett.*, 33:L04105, February 2006. doi: 10.1029/2005GL024891.

D. L. Gallagher, P. D. Craven, R. H. Comfort, and T. E. Moore. On the azimuthal variation of core plasma in the equatorial magnetosphere. *J. Geophys. Res.*, 100:23597–23606, December 1995. doi: 10.1029/95JA02100.

D. L. Gallagher, P. D. Craven, and R. H. Comfort. Global core plasma model. *J. Geophys. Res.*, 105:18, August 2000. doi: 10.1029/1999JA000241.

- M. Ghil, P. Yiou, S. Hallegatte, B. D. Malamud, P. Naveau, A. Soloviev, P. Friederichs, V. Keilis-Borok, D. Kondrashov, V. Kossobokov, O. Mestre, C. Nicolis, H. W. Rust, P. Shebalin, M. Vrac, A. Witt, and I. Zaliapin. Extreme events: dynamics, statistics and prediction. *Nonlinear Processes in Geophysics*, 18:295–350, May 2011. doi: 10.5194/npg-18-295-2011.
- T. Gold. Origin of the Radiation Near the Earth Discovered by Means of Satellites. *Nature*, 183:355–358, February 1959. doi: 10.1038/183355a0.
- W. D. Gonzalez, J. A. Joselyn, Y. Kamide, H. W. Kroehl, G. Rostoker, B. T. Tsurutani, and V. M. Vasyliunas. What is a geomagnetic storm? *J. Geophys. Res.*, 99:5771–5792, April 1994. doi: 10.1029/93JA02867.
- J. T. Gosling, D. J. McComas, J. L. Phillips, and S. J. Bame. Geomagnetic activity associated with earth passage of interplanetary shock disturbances and coronal mass ejections. *Journal Of Geophysical Research*, 96:7831–7839, May 1991. doi: 10.1029/91JA00316.
- J. V. Hernandez, T. Tajima, and W. Horton. Neural net forecasting for geomagnetic activity. *Geophysical Research Letters*, 20:2707–2710, December 1993. doi: 10.1029/93GL02848.
- A. Keiling. Alfvén Waves and Their Roles in the Dynamics of the Earth’s Magnetotail: A Review. *Space Sci. Rev.*, 142:73–156, February 2009. doi: 10.1007/s11214-008-9463-8.
- J. H. King and N. E. Papitashvili. Solar wind spatial scales in and comparisons of hourly Wind and ACE plasma and magnetic field data. *Journal of Geophysical Research (Space Physics)*, 110:A02104, February 2005. doi: 10.1029/2004JA010649.
- A. J. Klimas, D. Vassiliadis, and D. N. Baker. Dst index prediction using data-derived analogues of the magnetospheric dynamics. *Journal of Geophysical Research*, 103:20435–20448, September 1998. doi: 10.1029/98JA01559.
- D. Kondrashov, R. Denton, Y. Y. Shprits, and H. J. Singer. Reconstruction of gaps in the

past history of solar wind parameters. *Geophys. Res. Lett.*, 41:2702–2707, April 2014. doi: 10.1002/2014GL059741.

J Lemaire. *The Earth’s Plasmasphere*. Cambridge University Press, Cambridge, U.K. New York, 1998. ISBN 9780521430913.

T. M. Loto’aniu, C. L. Waters, B. J. Fraser, and J. C. Samson. Plasma mass density in the plasmatrough: Comparison using ULF waves and CRRES. *Geophys. Res. Lett.*, 26: 3277–3280, 1999. doi: 10.1029/1999GL003641.

L. R. Lyons and R. M. Thorne. Equilibrium structure of radiation belt electrons. *J. Geophys. Res.*, 78:2142–2149, May 1973. doi: 10.1029/JA078i013p02142.

MATLAB. *version 8.3 (R2014a)*. The MathWorks Inc., Natick, Massachusetts, 2014.

S. Maus. Magnetospheric magnetic field, August 2010. URL <http://geomag.org/info/magnetosphere.html>.

R. M. Millan and R. M. Thorne. Review of radiation belt relativistic electron losses. *Journal of Atmospheric and Solar-Terrestrial Physics*, 69:362–377, March 2007. doi: 10.1016/j.jastp.2006.06.019.

K. Min, J. Bortnik, R. E. Denton, K. Takahashi, J. Lee, and H. J. Singer. Quiet time equatorial mass density distribution derived from AMPTE/CCE and GOES using the magnetoseismology technique. *Journal of Geophysical Research (Space Physics)*, 118: 6090–6105, October 2013. doi: 10.1002/jgra.50563.

M. B. Moldwin, L. Downward, H. K. Rassoul, R. Amin, and R. R. Anderson. A new model of the location of the plasmapause: CRRES results. *Journal of Geophysical Research (Space Physics)*, 107:1339, November 2002. doi: 10.1029/2001JA009211.

NASA. Earths magnetosphere. URL https://www.nasa.gov/mission_pages/sunearth/science/inner-mag-mos.html.

Homer Newell. *Beyond the Atmosphere Early Years of Space Science*. Dover Publications, City, 2011. ISBN 0486135659. URL <http://history.nasa.gov/SP-4211/contents.htm>.

T. P. O'Brien and M. B. Moldwin. Empirical plasmapause models from magnetic indices. *Geophys. Res. Lett.*, 30:1152, February 2003. doi: 10.1029/2002GL016007.

National Oceanic and Atmospheric Administration. NOAA Space Weather Scales, 2005. URL http://www.swpc.noaa.gov/NOAA_scales/.

R. S. Richardson. Sun-Spots and Magnetic Storms. *Leaflet of the Astronomical Society of the Pacific*, 2:133, 1936.

C. Russel. Schematic of Earth's Night-Side Magnetosphere, June 2007. URL http://www.esa.int/spaceinimages/Images/2007/12/Schematic_of_Earth_s_night-side_magnetosphere.

Willie Soon and Steven H. Yaskell. *The Maunder Minimum and the Variable Sun-earth Connection*. World Scientific, 2003. ISBN 9789812382757.

K. Takahashi, R. E. Denton, R. R. Anderson, and W. J. Hughes. Mass density inferred from toroidal wave frequencies and its comparison to electron density. *Journal of Geophysical Research (Space Physics)*, 111:A01201, January 2006. doi: 10.1029/2005JA011286.

K. Takahashi, R. E. Denton, and H. J. Singer. Solar cycle variation of geosynchronous plasma mass density derived from the frequency of standing Alfvén waves. *Journal of Geophysical Research (Space Physics)*, 115:A07207, July 2010. doi: 10.1029/2009JA015243.

M. Temerin and X. Li. A new model for the prediction of Dst on the basis of the solar wind. *Journal of Geophysical Research (Space Physics)*, 107:1472, December 2002. doi: 10.1029/2001JA007532.

M. F. Thomsen. Why K_p is such a good measure of magnetospheric convection. *Space Weather*, 2:S11004, November 2004. doi: 10.1002/2004SW000089.

N. A. Tsyganenko and M. I. Sitnov. Modeling the dynamics of the inner magnetosphere during strong geomagnetic storms. *Journal of Geophysical Research (Space Physics)*, 110: A03208, March 2005. doi: 10.1029/2004JA010798.

D. Vassiliadis, R. S. Weigel, D. N. Baker, S. G. Kanekal, and A. J. Klimas. Probing the solar wind-inner magnetospheric coupling: validation of relativistic electron flux models. *Journal of Atmospheric and Solar-Terrestrial Physics*, 66:1399–1409, October 2004. doi: 10.1016/j.jastp.2004.03.025.

Martin Walt. *Introduction to Geomagnetically Trapped Radiation*. Cambridge University Press, Cambridge New York, 1994. ISBN 9780521431439.

R. S. Weigel. Solar wind time history contribution to the day-of-year variation in geomagnetic activity. *Journal of Geophysical Research (Space Physics)*, 112:A10207, October 2007. doi: 10.1029/2007JA012324.

Y. I. Yermolaev and M. Y. Yermolaev. Statistic study on the geomagnetic storm effectiveness of solar and interplanetary events. *Advances in Space Research*, 37:1175–1181, 2006. doi: 10.1016/j.asr.2005.03.130.

S. L. Young, R. E. Denton, B. J. Anderson, and M. K. Hudson. Magnetic field line curvature induced pitch angle diffusion in the inner magnetosphere. *Journal of Geophysical Research (Space Physics)*, 113:A03210, March 2008. doi: 10.1029/2006JA012133.

J. Zhang, M. W. Liemohn, J. U. Kozyra, M. F. Thomsen, H. A. Elliott, and J. M. Weygand. A statistical comparison of solar wind sources of moderate and intense geomagnetic storms at solar minimum and maximum. *Journal of Geophysical Research (Space Physics)*, 111: A01104, January 2006. doi: 10.1029/2005JA011065.

J. Zhang, I. G. Richardson, D. F. Webb, N. Gopalswamy, E. Huttunen, J. C. Kasper, N. V. Nitta, W. Poomvises, B. J. Thompson, C.-C. Wu, S. Yashiro, and A. N. Zhukov. Solar

and interplanetary sources of major geomagnetic storms ($Dst \leq -100$ nT) during 1996-2005. *Journal of Geophysical Research (Space Physics)*, 112:A10102, October 2007. doi: 10.1029/2007JA012321.

Curriculum Vitae

Include your *curriculum vitae* here detailing your background, education, and professional experience.